The Role of LYVE-1 in Macrophages during Heart Regeneration and Repair

A Thesis Submitted for the Degree of Doctor of Philosophy

Benjamin G. Chapman

University of Oxford
Balliol College

Trinity 2025

ACKNOWLEDGEMENTS

I am grateful to Professor Paul Riley and Dr Joaquim Vieira for their dedicated supervision and support throughout this work. Paul's mentorship has been instrumental in my development as a researcher and a professional; his guidance has offered me the independence to shape my own work while maintaining rigour and direction. I am thankful to Joey for his sustained oversight and constructive input, even while pursuing his own work away from Oxford.

Starting this project, the steep learning curve was eased by the supportive and welcoming environment of the Riley Group, a team I quickly felt at home with. I would particularly like to acknowledge Dr Susanna Cooper, whose practical assistance and advice contributed to many experiments in this thesis. I also thank the rest of the team, Dr Emma Haberman, Dr Adam Lokman, Dr Christophe Ravaud, Dr Claudio Cortes Rodriguez, and many others for helpful discussions and day-to-day support. I am grateful to Sarah Sigal and Alexa Cosma for conducting the surgical procedures, and to Dr Michael Weinberger for bioinformatics support and constructive input on analysis strategy. Thanks also to the BMS staff, especially Mellissa Nixon for her reliable assistance and advice.

I have benefited from being part of the cardiac floor and the wider community at the Institute of Developmental and Regenerative Medicine (IDRM). I am particularly grateful to Mary Strevens for her perspective as we both navigated the writing process. There are too many colleagues to name them all individually, but the collective effort has been essential to this project. It has been a privilege to work at the Institute during its establishment.

I am indebted to those whose earlier teaching and support made this work possible, particularly Professor Clive Wilson and Professor Emeritus John Morris. I also thank Dr Catherine Swales and the OxKen team, as well as my coursemates, for making the return to clinical training as smooth as it could be.

The work presented in this thesis was made possible by the award of an OxKen MB-PhD Studentship from the Kennedy Trust for Rheumatology Research, for which I am extremely grateful. I would also like to acknowledge the International Society for Heart Research and the European Association for Cardiothoracic Surgery, as well as Balliol College, for supporting my attendance at international conferences.

I am grateful to friends outside the lab for their encouragement; their questions and suggestions were entertaining and useful in equal measure. Finally, I would like to thank my family – Jess, Jason, Jack, and Charlie – and my partner Megan for their enduring support throughout this DPhil.

TABLE OF CONTENTS

SUMMARY OF DPHIL ACTIVITY 18

I. MEETINGS ATTENDED 18
II. PRIZES 18
III. PUBLICATIONS 19
IV. TEACHING 19
V. FUNDING 20
1 ABSTRACT 21
2 INTRODUCTION 24
2.1 Myocardial Infarction and Heart Failure 24
2.2 Models of cardiac regeneration 26
2.2.1 Mammals 26
2.2.2 Other species 27
2.3 Hallmarks of cardiac regeneration 28
2.3.1 Remuscularisation 28
2.3.2 Electromechanical stability 29
2.3.3 Angiogenesis 30
2.3.4 Resolution of fibrosis and ECM remodelling 32
2.3.5 Immunological balance 33
2.4 Cardiac macrophages in regeneration and repair 35
2.4.1 In the adult mouse 35
2.4.2 In the neonatal mouse 37
2.5 Cardiac Lymphatics and Immune Cell Clearance 38
2.5.1 Mature cardiac lymphatics 38
2.5.2 Developing cardiac lymphatics 39
2.6 LYVE-1 is a lymphatic endothelium receptor and homologue of CD44 ... 42
2.6.1 LYVE-1 functions to facilitate transmigration into lymphatics 42
2.6.2 *Lyve1* knockout worsens outcomes post-MI in the adult mouse 43
2.6.3 *Lyve1* knockout unexpectedly impairs neonatal cardiac regeneration 44
2.6.4 LYVE-1 is also expressed on macrophages 44
2.6.5 Mechanistic insight from $CD44^{+}$ macrophages 45
2.7 Thesis Rationale 46
2.7.1 Hypothesis 46
2.7.2 Project Aims 46

2.7.3 Achievement of Aims 47
3 MATERIALS AND METHODS 49
3.1 Animal Work 49
3.1.1 Mouse Strains 49
3.1.2 Timed Matings 49
3.1.3 Neonatal Heart Dissection 49
3.1.4 Neonatal Myocardial Infarction Surgery 50
3.1.5 Tamoxifen Dosing and Administration 51
3.2 Molecular Techniques 51
3.2.1 DNA extraction 51
3.2.2 Polymerase chain reaction (PCR) 51
3.2.3 Agarose gel electrophoresis 52
3.2.4 RNA extraction from tissue 53
3.2.5 Complementary DNA (cDNA) synthesis 53
3.2.6 Real-time quantitative PCR 54
3.3 Immunofluorescent Staining and Histology 55
3.3.1 Whole-Mount Tissue Clearing – CUBIC 55
3.3.2 Whole-Mount Tissue Clearing – iDISCO 56
3.3.3 Paraffin Embedding 57
3.3.4 Cryosectioning 57
3.3.5 Picrosirius Red Staining 58
3.3.6 Immunofluorescent staining of tissue sections 58
3.3.7 Immunofluorescent staining of whole neonatal hearts 61
3.4 Flow cytometry 62
3.4.1 Adult cardiac cell isolation 62
3.4.2 Neonatal cardiac cell isolation 62
3.4.3 Antibody staining 63
3.4.4 Sample analysis 64
3.5 Analysis of Cardiac Function 64
3.5.1 Cardiac cine magnetic resonance imaging (MRI) 64
3.5.2 MRI data processing 64
3.6 Bioinformatics 65
3.6.1 Single cell RNA sequencing and analysis: 10x Sequencing 65
3.6.2 scRNA-seq data processing and analysis 65
3.7 Statistical analysis 67

4 RESULTS I: CLEARANCE AND RETENTION OF LYVE-1^{+} CARDIAC RESIDENT MACROPHAGES 68

4.1 Background 68
4.2 Aims 69
4.3 Results 70
4.3.1 Morphology of the postnatal cardiac lymphatics P1-P14 70
4.3.1.1 Tissue clearing for imaging of lymphatics at depth 70
4.3.1.2 Developing morphology of lymphatic junctions 73
4.3.2 Single-cell analysis of neonatal cardiac lymphatics 78
4.3.3 Macrophages are trafficked following MI at P7 but not P1 83
4.3.4 LEC and macrophage molecular pathways at P1 versus P7 90
4.3.5 Global *Lyve1* knockout impairs cardiac regeneration 93
4.3.6 LYVE-1 is also expressed on macrophages, potentially accounting for worsened outcomes in the global knockout 95
4.4 Discussion 96
4.4.1 Neonatal cardiac lymphatics are not well understood 97
4.4.2 Adult cardiac lymphatics clear macrophages to improve outcomes 97
4.4.3 Temporal determination of macrophage subtype and clearance 98
4.4.4 Tissue-resident macrophage retention following P1 MI 99
4.4.5 Early postnatal cardiac lymphatics are functionally immature 99
4.4.6 Macrophage-lymphatic endothelial cell crosstalk 101
4.4.7 Functional impairment in *Lyve1*$^{-/-}$ P1 hearts post-MI 102
4.4.8 LYVE-1 is also expressed on tissue-resident macrophages 103
4.5 Summary 103

5 RESULTS II: TISSUE-RESIDENT MACROPHAGES REQUIRE LYVE-1 TO FACILITATE REGENERATIVE HEALING POST-MI 104

5.1 Background 104
5.2 Aims 104
5.3 Results 105
5.3.1 Characterisation of *hCD68-CreERT2;Lyve1*$^{fl/fl}$ construct 105
5.3.1.1 Tamoxifen delivery with neonatal coronary artery ligation 105
5.3.1.2 Rosa26^{TdTomato} quantification 106
5.3.1.3 *Lyve1*^{flox} knockdown quantification 107
5.3.2 Cardiac cine MRI of P2MI28dpi *hCD68-CreERT2;Lyve1*$^{fl/fl}$ mice 110
5.3.3 Histological analysis of *hCD68-CreERT2;Lyve1*$^{fl/fl}$ hearts post-MI 112
5.4 Discussion 116

5.4.1 Macrophage-specific *Lyve1* knock down in the neonatal mouse.....116
5.4.2 Macrophage LYVE-1 is required for cardiac regeneration 117
5.5 Summary.....119
6 RESULTS III: LOSS OF LYVE-1 PREDISPOSES TISSUE-RESIDENT MACROPHAGES TO APOPTOSIS, FACILITATING REPLACEMENT BY INFILTRATING MACROPHAGES AND MONOCYTES.....121
6.1 Background.....121
6.2 Aims.....122
6.3 Results 122
6.3.1 scRNA-seq analysis 122
6.3.1.1 $CD45^+$ cell clustering analysis.....122
6.3.1.2 Macrophage sub-cluster analysis.....124
6.3.1.3 GO term and DEG analysis 127
6.3.1.4 Speculative Mechanism for Shift in Macrophage Subpopulations .132
6.3.1.5 Glycocalyx Visualisation in wildtype and *Lyve1*$^{-/-}$ hearts 136
6.3.2 Investigating the expression of LYVE-1 in BMDMs.....137
6.3.2.1 Unstimulated BMDMs do not express LYVE-1 137
6.3.2.2 BMDM stimulation fails to induce LYVE-1 expression.....139
6.4 Discussion.....142
6.4.1 Loss of *Lyve1* results in depletion of $CCR2^-$ resident macrophages.....142
6.4.2 The glycocalyx and macrophage survival: implications for LYVE-1 143
6.4.3 Limitations of BMDMs for studying the HA–LYVE-1 axis.....143
6.4.4 Other possible roles for macrophage LYVE-1 144
6.5 Summary.....145
7 RESULTS IV: LYVE-1 KNOCKOUT IN ADULT MYOCARDIAL INFARCTION.....147
7.1 Background.....147
7.2 Aims.....148
7.3 Results 148
7.3.1 A LYVE-1^+ macrophage subset in the adult heart following MI 148
7.3.2 Differential expression of efferocytosis-associated genes.....150
7.3.3 Neutrophil retention in *hCD68-CreERT2;Lyve1*$^{-/-}$ adult hearts post-MI 154
7.4 Discussion.....157
7.4.1 Neutrophil retention in the adult *Lyve1*$^{-/-}$ heart.....157
7.4.2 Efferocytosis analysis 158
7.5 Summary.....159

8 FINAL CONCLUSIONS AND FUTURE WORK 160

8.1 Main Findings 160

8.2 Future Work and Translational Potential 161

8.2.1 Maturation of lymphatic fluid transport 161

8.2.2 Exploration of macrophage LYVE-1^{+} function 162

8.2.3 *In vitro* LYVE-1^{+} macrophage assays 163

8.2.4 Macrophage LYVE-1 contribution to adult repair 164

8.2.5 Clinical Translation 164

8.3 Final Remarks 166

9 BIBLIOGRAPHY 167

Table of Figures

Figure 2-1. E18.5 heart stained for LYVE-1 and EMCN. 45
Figure 2-2. Summary of findings. 48
Figure 4-1. CUBIC-cleared uninjured P7 heart. 71
Figure 4-2. iDISCO-cleared hearts: P1, P7, P14. 72
Figure 4-3. Co-staining of surface lymphatics for LYVE-1 and VEGFR3. 73
Figure 4-4. Lymphatic button and zipper junctions. 75
Figure 4-5. Anti-VE-Cadherin antibody robustly targets lymphatics and capillaries. 76
Figure 4-6. Identification of lymphatic ultrastructure in P7 heart sections. 77
Figure 4-7. P1 versus P7 cardiac cell scRNA-seq data. 79
Figure 4-8. Genes differentially expressed by LECs between conditions. 81
Figure 4-9. GO pathway enrichment in LECs after MI: P1 vs P7. 82
Figure 4-10. Visualisation of *hCD68–eGFP* GFP^{+} macrophages in MLNs post-MI. 84
Figure 4-11. Macrophage drainage to mediastinal lymph nodes. 86
Figure 4-12. CX3CR1-GFP F4/80 co-staining. 88
Figure 4-13. F4/80 macrophage within mediastinal lymph node afferent lymphatics. 90
Figure 4-14. Lymphatic-macrophage crosstalk. 92
Figure 4-15 Cardiac cine MRI data from K. Klaourakis and C. Carr[101] 93
Figure 4-16. Picrosirius red staining of neonatal *Lyve1*$^{-/-}$ hearts post-MI. 94
Figure 4-17. LYVE-1^{+} macrophages are present in the P1 heart. 96
Figure 5-1. Protocol for concurrent tamoxifen administration with neonatal MI. 106
Figure 5-2. Characterisation of *hCD68-CreERT2;TdTomato* line. 107
Figure 5-3. Characterisation of *hCD68-CreERT2;Lyve1*$^{fl/fl}$ knockdown. 109
Figure 5-4. Cardiac cine MRI representative images. 111
Figure 5-5. Conditional *Lyve1* knockout MRI quantification. 111
Figure 5-6. MRI-derived cardiac function at 28 days post-MI across conditions. 112
Figure 5-7. Quantification of *hCD68-CreERT2;Lyve1*$^{fl/fl}$ infarct scar at 28dpi. 113
Figure 5-8. Infarct zone histology: scar, neovascularisation, and macrophages. 115
Figure 6-1. Wildtype versus *Lyve1*$^{-/-}$ P2MI7dpi scRNA-seq dataset. 124
Figure 6-2. Macrophage subcluster differential abundance. 126
Figure 6-3. Visualisation by UMAP of macrophage subclusters. 127
Figure 6-4. Differential expression within *Ccr2*$^{-}$ macrophage subcluster. 129
Figure 6-5. GO enrichment of DEGs in the *Ccr2*$^{-}$ *Lyve1*$^{+}$ subcluster. 130

Figure 6-6. Dot plot mapping macrophage subcluster phenotypes by gene. 131
Figure 6-7. Assessment of apoptotic markers in the scRNA-seq dataset and *in vivo*... 133
Figure 6-8. Differential expression of *Lyve1* and *Cd44* in macrophage subclusters. ... 135
Figure 6-9. Macrophage glycocalyx visualisation. 136
Figure 6-10. BMDM isolation and induction. 138
Figure 6-11. Stimulation by IL-4 fails to induce LYVE-1 expression in BMDMs. 140
Figure 6-12. BMDM flow-cytometry and IF after IL-4, dexamethasone, PGE_2. 141
Figure 7-1. Adult heart scRNA-seq shows *Lyve1* in a macrophage subset after MI. ... 149
Figure 7-2. Immune cell composition in the *Lyve1*$^{-/-}$ adult heart post-MI. 150
Figure 7-3. Efferocytosis-associated genes by macrophage subcluster after adult MI. 154
Figure 7-4. Flow cytometry panel for neutrophil and macrophage quantification. 155
Figure 7-5. Adult neutrophils and LYVE-1^{+} macrophages: conditional KO post-MI. 156

List of Tables

Table 3-1 PCR primers for genotyping.....52
Table 3-2 Primers for qRT-PCR.....55
Table 3-3 List of primary antibodies 59
Table 3-4 List of secondary antibodies.....60
Table 7-1. List of phagocytosis-associated genes.....152

List of Abbreviations

ANOVA – analysis of variance

ATP – adenosine triphosphate

BMDM – bone marrow-derived macrophage

BSA – bovine serum albumin

cDNA – complementary DNA

CO – cardiac output

CUBIC – clear, unobstructed brain/body imaging cocktails and computational analysis

DAMPs – damage-associated molecular patterns

DAPI – 4′,6-diamidino-2-phenylindole

DEG – differentially expressed gene(s)

dpi – days post-injury

E# – embryonic day number (e.g., E14.5)

ECM – extracellular matrix

EF – ejection fraction

FACS – fluorescence-activated cell sorting

GEF – guanine nucleotide exchange factor

GO – gene ontology

HA – hyaluronic acid

HABP – hyaluronan-binding protein

HBSS – Hanks' balanced salt solution

HFpEF – heart failure with preserved ejection fraction

iDISCO – immunolabelling-enabled 3-dimensional imaging of solvent-cleared organs

iPSC – induced pluripotent stem cell

LAD – left anterior descending (coronary artery)

LEC – lymphatic endothelial cell

MHC – Major histocompatibility complex

MI – myocardial infarction

MLN – mediastinal lymph node(s)

MRI – magnetic resonance imaging

OCT – optimal cutting temperature compound (cryosectioning medium)

P# – postnatal day number (e.g., P1, P7)

P#MI#dpi – Myocardial infarction induced at postnatal day #, # days post-injury

PBS – phosphate-buffered saline

PCR – polymerase chain reaction

PSR – picrosirius red (collagen stain)

PFA – paraformaldehyde

qPCR – quantitative PCR

qRT-PCR – quantitative reverse-transcription PCR

RBC – red blood cell

ROS – reactive oxygen species

scRNA-seq – single-cell RNA sequencing

SNP – single-nucleotide polymorphism

STEMI – ST-elevation myocardial infarction

SV – stroke volume

TR – tissue-resident

UMAP – Uniform Manifold Approximation and Projection

WGA – wheat germ agglutinin (lectin membrane stain)

WT – wildtype

List of Proteins and Genes

ADAM17 (*Adam17*) – A disintegrin and metalloproteinase 17.

AQP1 (*Aqp1*) – Aquaporin-1 water channel.

BMP (*Bmp*) – Bone morphogenic protein.

CCL2 (*Ccl2*) – C-C motif chemokine ligand 2 (monocyte chemoattractant).

CCL21 (*Ccl21*) – C-C motif chemokine ligand 21 (lymphoid chemokine).

CCR2 (*Ccr2*) – C-C chemokine receptor 2 (monocyte recruitment receptor).

CCR7 (*Ccr7*) – C-C chemokine receptor 7 (lymph node homing receptor).

CD11b (*Itgam*) – Integrin αM (Mac-1 subunit).

PECAM-1 / CD31 (*Pecam1*) – Platelet endothelial cell adhesion molecule-1.

CD36 (*Cd36*) – Class B scavenger receptor (lipid uptake/efferocytosis).

CD44 (*Cd44*) – Hyaluronan receptor/adhesion molecule.

CD68 (*Cd68*) – Macrophage/lysosomal glycoprotein marker.

Claudin-5 (*Cldn5*) – Tight-junction claudin family member.

Connexin-43 (*Gja1*) – Gap-junction channel protein α1.

CXCR4 (*Cxcr4*) – C-X-C motif chemokine receptor 4.

CXCL12 (*Cxcl12*) – C-X-C motif Chemokine Ligand 12.

CX3CR1 (*Cx3cr1*) – C-X3-C motif chemokine receptor 1 / fractalkine receptor.

CX3CL1 (Cx3cl1) – C-X-C motif Chemokine Ligand 1 / fractalkine.

Endomucin (*Emcn*) – Endothelial sialomucin.

FOXC2 (*Foxc2*) – Forkhead box C2 (collecting lymphatic maturation).

GATA2 (*Gata2*) – GATA-binding protein 2.

HMGB1 (*Hmgb1*)– High mobility group box 1.

IGF1 (*Igb1*) – Insulin-like growth factor 1.

ITGB1 (*Itgb1*) – Integrin β1 (matrix and cell–cell adhesion).

LYVE-1 (*Lyve1*) – Lymphatic vessel endothelial hyaluronan receptor-1.

Ly6C (*Ly6c1*) – Lymphocyte antigen 6C.

MEF2 (*Mef2a/b/c/d*) – Myocyte enhancer factor 2.

MerTK (*Mertk*) – MER tyrosine kinase receptor (efferocytosis).

Neuropilin-2 (*Nrp2*) – VEGF co-receptor.

Occludin (*Ocln*) – Tight-junction integral membrane protein.

Podoplanin (*Pdpn*) – Lymphatic/stromal glycoprotein.

PROX1 (*Prox1*) – Prospero homeobox protein 1 (LEC specification factor).

RAC1 (*Rac1*) – Rho-family small GTPase 1 (actin dynamics/phagocytosis).

RBPJ (*Rbpj*) – Recombination signal binding protein for immunoglobulin kappa J region

REELIN (*Reln*) – Extracellular-matrix glycoprotein (signalling/adhesion).

RHAMM (*Hmmr*) – Receptor for hyaluronan-mediated motility

SGLT2 (*SGLT2*) – Solute carrier family 5 member 2.

SMAD (*Smad*) - Transforming growth factor-beta signalling Protein.

SOX18 (*Sox18*) – SRY-box transcription factor 18 (lymphatic development).

TIE2 (*Tek*) – Endothelial tyrosine kinase receptor (angiopoietin receptor).

TIMD4 (*Timd4*) – T-cell immunoglobulin and mucin domain-containing 4 (macrophage receptor).

VE-cadherin (*Cdh5*) – Vascular endothelial cadherin (adherens junction).

VEGFA (*Vegfa*) – Vascular endothelial growth factor A.

VEGFB (Vegfb) – Vascular endothelial growth factor B.

VEGFC (*Vegfc*) – Vascular endothelial growth factor C.

VEGFD (*Figf*) – Vascular endothelial growth factor D.

VEGFR2 / KDR (*Kdr*) – Vascular endothelial growth factor receptor-2.

VEGFR3 (*Flt4*) – Vascular endothelial growth factor receptor-3.

ZO-1 (*Tjp1*) – Tight-junction protein 1 (zonula occludens-1).

IL-4 (*Il4*) – Interleukin-4 (Th2 cytokine; used for BMDM stimulation).

Statement of Contribution and Prior Publication

This thesis is my own work except where indicated. Contributions of collaborators are acknowledged in the text and figure legends. Chapters 3–6 include material adapted from our publication in *Nature Cardiovascular Research*:

Chapman, B.G., Klaourakis, K…[11 others]…, **Vieira, J.M, Riley, P.R.** Cardiac lymphatics retain LYVE-1-dependent macrophages during neonatal mouse heart regeneration. *Nat Cardiovasc Res* (2025). doi.org/10.1038/s44161-025-00711-4

Text inclusions have been adapted to delineate my contribution from those of my collaborators. Figure inclusions have been reformatted and, where possible, expanded for thesis presentation to aid clarity beyond journal constraints.

SUMMARY OF DPHIL ACTIVITY

I. MEETINGS ATTENDED

Oral Presentations Delivered

Society for Cardiothoracic Surgery (SCTS) Annual Meeting
Edinburgh, UK, March 2025.

International Society for Heart Research (ISHR) XXV World Congress
Nara, Japan, 2025.

Surgical Research Society (SRS) Annual Meeting, Plenary Prize Session
Cambridge, UK, 2025.

OxKen Annual Student Symposium
Oxford, UK, 2024 and 2025.

MSDTC Annual Student Symposium
Oxford, UK, 2025.

Poster Presentations Delivered

European Society for Cardiology (ESC) Annual Congress
London, UK, 2024.

British Association of Clinical Anatomists (BACA) Summer Meeting
Birmingham, UK, 2025.

II. PRIZES

Research Awards

Surgical Research Society (SRS): Young Investigator Award
Cambridge, UK, 2025.

Annual OxKen Student Symposium: Award for Best Oral Presentation of Year

Oxford, UK, 2024 and 2025. *Awarded twice, consecutive years.*

British Association of Clinical Anatomists (BACA) Summer Meeting: Award for Best Poster Presentation

Birmingham, UK, 2025.

Travel Grants

International Society for Heart Research (ISHR): Early Career Researcher Travel Grant

Nara, Japan, 2025.

European Association for Cardiothoracic Surgery (EACTS): Francis Fontan Fund Pre-Trainee Annual Meeting Grant

Copenhagen, Denmark, 2025.

Royal College of Surgeons of Edinburgh (RCSEd) and Vascutek Cardiothoracic Surgery Elective Placement Grant

Guy's and St Thomas' NHS Foundation Trust, London, UK, 2025.

III. PUBLICATIONS

Chapman, B.G., Klaourakis, K…[11 others]…, **Vieira, J.M, Riley, P.R.** Cardiac lymphatics retain LYVE-1-dependent macrophages during neonatal mouse heart regeneration. Nat Cardiovasc Res (2025). doi.org/10.1038/s44161-025-00711-4

IV. TEACHING

Anatomy Demonstrator

Department of Physiology, Anatomy, and Genetics (DPAG), University of Oxford.

Led weekly small-group gross anatomy teaching for undergraduate and graduate-entry medical students during term, using prosected human cadaveric specimens.

Associate Fellow of the Higher Education Academy (AFHEA)

Advance HE

In recognition of attainment against the Professional Standards Framework for teaching and learning support in higher education.

V. FUNDING

This work was supported by the Kennedy Trust for Rheumatology Research by the award of an OxKen MB-PhD Studentship.

Additional institutional support and core facility access were provided by the Institute of Developmental and Regenerative Medicine (IDRM), University of Oxford.

1 ABSTRACT

Myocardial infarction (MI) causes substantial cardiomyocyte death and leads to heart failure, one of the most common causes of death globally. While surgical and transcatheter techniques have evolved to facilitate reperfusion, loss of these cardiomyocytes remains irreversible in humans. This cell death is accompanied by significant infiltration of immune cells which are required to clear the necrotic debris. In adult mice, MI activates the cardiac lymphatics, which undergo sprouting angiogenesis (lymphangiogenesis) and function to drain interstitial fluid and traffic macrophages to mediastinal lymph nodes (MLNs). This prevents oedema and reduces inflammatory/fibrotic immune cell content to improve cardiac function.

Given the importance of the adult cardiac lymphatics in macrophage clearance after injury, I continued investigation into their role across the neonatal "regenerative window". At postnatal day 1 (P1) neonatal mice fully regenerate their heart following MI, in a pro-regenerative macrophage-dependent manner, whereas equivalent injury at postnatal day 7 (P7) leads to scarring driven by pro-fibrotic macrophages. I hypothesised that lymphatics respond and function differently during this "window" to clear macrophage-specific subtypes, depending upon their requirement for regeneration versus fibrotic repair. Previous work within the group has revealed limited lymphangiogenesis and preliminary evidence of reduced macrophage clearance from P1 compared to P7 infarcted hearts. The increase in macrophage clearance was coincident with maturation of lymphatic endothelial cell (LEC) junctions across the neonatal period via transition from "zipper" (impermeable) to "button" (permeable) -type junctions. In the present work I provide further evidence of this differential macrophage clearance and lymphatic maturation. I also demonstrate evidence of altered signalling between LECs and

macrophages across the regenerative window, including differential expression of the lymphangiocrine factor Reelin (RELN).

Prior work from the lab demonstrated that in mice lacking the lymphatic endothelial receptor-1 (LYVE-1) – that exhibit impaired transmigration of interstitial macrophages to lymphatic vessels – magnetic resonance imaging (MRI) revealed a surprising impaired functional outcome in P1 mice 28 days post-MI. Given our observations that pro-regenerative macrophages at P1 are not trafficked, this suggested a distinct role for LYVE-1 in tissue-resident macrophages, consistent with its expression pattern in developing and postnatal hearts. I therefore conducted macrophage-specific deletion of *Lyve1* during neonatal heart injury which revealed impaired heart regeneration, characterised by a reduced neovascular response and reduced function. Subsequent single-cell RNA sequencing (scRNA-seq) of *Lyve1* deficient $CD45^+$ cells revealed a loss of tissue-resident macrophages by apoptosis and an increase in recruited monocytes. Tissue-resident macrophage retention is known to facilitate regeneration, the loss of this population accompanied by increased monocyte infiltration is predicted to increase inflammation and fibrosis, worsening the outcome post-MI. On the basis of immunofluorescent staining, I speculate that loss of *Lyve1* promotes apoptosis in tissue-resident macrophages by disrupting the hyaluronic acid glycocalyx to expose pro-apoptotic elements on the membrane surface.

Collectively, this thesis reveals that cardiac lymphatics are developmentally compromised for clearance in early neonates, which enables retention of pro-regenerative tissue-resident macrophages, and that LYVE-1 plays an essential role in maintaining this population to promote heart regeneration and prevent inflammation and fibrotic repair.

The role of LYVE-1 in adult macrophages constitutes a promising area of follow-up investigation and I have conducted preliminary experiments to inform possible future work.

2 INTRODUCTION

2.1 Myocardial Infarction and Heart Failure

Myocardial infarction (MI) results in the ischaemic death of cardiomyocytes and abrupt loss of cardiac function; the failure of the myocardium to regenerate and the formation of fibrotic scar to replace dead tissue ultimately leads to systolic dysfunction, arrhythmias and heart failure (HF). As a result of this irreversible damage, ischaemic heart disease represents a significant contributor to cardiovascular disease, which is the single largest cause of death globally[1].

Contemporary clinical intervention aims to limit the size and impact of the initial infarct via rapid reperfusion, preferably by primary percutaneous coronary intervention (PCI) and adjunct antithrombotic therapy, or by fibrinolysis when timely PCI cannot be delivered[2]. These strategies improve survival but do not restore myocardium. As more patients survive the index event, the burden of post-MI HF is increasingly apparent. Crucially, modern HF guideline-directed therapy (ACE inhibitors, beta-blockers, mineralocorticoid receptor antagonists, SGLT2 inhibitors) is disease-modifying, but does not directly counteract the irretrievable loss of cardiomyocytes[3]. For advanced HF, heart transplantation remains the only definitive restorative therapy[4].

Within this context, the importance of new interventions that regrow the myocardium is clear. To date, attempts to remuscularise the heart with transplanted cells have not delivered consistent clinical efficacy or durable engraftment. Early programmes using iPSC-derived cardiomyocyte patches show feasibility in preclinical work and small human studies[5,6]; efficacy remains unproven because clinical experience is still limited

to small, early-phase studies primarily designed for optimising consistent engraftment, electromechanical coupling, and maturation[5-7].

Accordingly, the field is shifting to prioritise mechanism-led strategies that reactivate endogenous regeneration. Many mammals retain a brief neonatal regenerative window, suggesting that re-engaging dormant developmental pathways may, in principle, restore function after injury. To develop such therapies, it is necessary to understand and define the molecular processes that permit growth in the developing and early postnatal heart, and how these processes are constrained in maturity. Promising candidate pathways include reactivation of cardiomyocyte cell-cycle programmes and developmental signalling axes such as Hippo-YAP/TAZ, active in cardiac developmental and implicated as mechanisms to re-enter cardiomyocyte proliferation programmes in the injured adult heart[8].

Regrowth of myocardium is not the only feasible therapy in the post-MI window. Modulating resolution of inflammation is an important therapeutic target: infiltrating immune cells, while necessary in the first instance, are ultimately damaging when they persist. Therapeutic options that optimise their removal therefore represent a plausible approach to further limiting infarct damage. Increasing cardiac lymphatic drainage is an approach that has demonstrated efficacy in adult mice following MI – for example, by augmenting lymphangiogenesis by exogenous stimulation with VEGFC[9]. How the cardiac lymphatics operate in the developing and neonatal heart remains an open question and these uncertainties motivate the central aims of this thesis.

2.2 Models of cardiac regeneration

2.2.1 Mammals

A substantial proportion of patients who suffer an MI will go on to develop HF, largely because mature mammalian cardiomyocytes have exited the cell cycle and lost proliferative capacity. Postnatal maturation involves cell-cycle withdrawal with induction of binucleation/polyploidy, sarcomere and extracellular matrix (ECM) remodelling, and a metabolic switch from glycolysis to fatty acid oxidation –features associated with poor proliferative and regenerative potential[10-12]. Across vertebrate models, successful regeneration typically hinges on cardiomyocyte dedifferentiation and proliferation, rapid neovascularisation within the infarct, immune modulation that favours resolution over fibrosis, and permissive ECM remodelling[13].

By contrast, the neonatal mammalian heart retains a brief, evolutionarily conserved capacity for regeneration[14]. In mice the heart fully regenerates after MI at postnatal day 1 (P1), whereas the same injury at postnatal day 7 (P7) leads to fibrotic scarring[15,16]. Original studies employed apical resection, while subsequent work extended the principle to surgical coronary artery ligation with the reported ‘completeness’ of regeneration dependent on the injury paradigm, functional readouts, and follow-up duration.

Case reports in humans suggest analogous potential in early life: infants with ischaemic cardiac injury (for example, coronary thrombosis associated with congenital heart disease) have shown complete functional recovery over time[17-19]. These observations are not definitive, but they underscore the plausibility of a neonatal regenerative window in humans.

Notably, among adult mammals, the spiny mouse (*Acomys* cahirinus) exhibits endogenous cardiac recovery after MI. Despite comparable infarct size and mechanism to *Mus musculus*, the spiny mouse shows reduced mortality and scar size by ~50 days, accompanied by enhanced endothelial proliferation, angiogenesis, and vessel infiltration into the infarct border zone. This cardiac phenotype aligns with the spiny mouse's broader capacity to heal complex tissues with minimal scarring[20,21].

2.2.2 Other species

Outside mammals, several vertebrates exhibit robust adult cardiac regeneration. Zebrafish and axolotls regenerate myocardium after ventricular resection via proliferation of pre-existing cardiomyocytes, restoring structure and function within weeks[22,23]. These models are central to defining the cellular and molecular programmes in the setting of adult cardiac regeneration.

Intriguingly, capacity for cardiac regeneration can vary between organisms of a single species. The Mexican cavefish (*Astyanax mexicanus*) comprises two forms: a surface-dwelling fish which regenerate their hearts, and a cave-dwelling fish which heal with a permanent scar akin to adult mammals. Such divergence in otherwise closely related animals provides an opportunity for understanding how differences in the inflammatory environment can determine regenerative potential[24].

Conversely, closely related but non-regenerative teleost and amphibian models such as the medaka and some xenopus strains form persistent scars after comparable injury, allowing identification of differences that may facilitate cardiac regeneration.

2.3 Hallmarks of cardiac regeneration

Effective cardiac regeneration across vertebrate models is characterised by five interdependent components: remuscularisation, electromechanical stability, angiogenesis, resolution of fibrosis, and immunological balance[25]. These elements act within the broader post-MI environment, shaped by ECM composition, stromal-parenchymal crosstalk, coronary and lymphatic vasculature, and the integrity of the cardiac conduction system and autonomic innervation[26].

2.3.1 Remuscularisation

Restoration of cardiac function by muscular regrowth requires expansion of cardiomyocyte mass through cellular growth (hypertrophy) or cellular proliferation (hyperplasia). In regenerative settings, mass is restored largely by proliferation of pre-existing cardiomyocytes following transient dedifferentiation and cell-cycle re-entry. This has been demonstrated directly in zebrafish using lineage tracing and mitotic labelling[22,27]. More recently, neonatal mouse studies using a genetic reporter ('CycleTrack') that marks passage through the G2/M phase have captured cardiomyocyte cycling *in vivo*[28]. In mature cardiomyocytes, proliferation is constrained by cell-intrinsic programmes established postnatally. Manipulation of Hippo signalling illustrates this: activation of the downstream effector YAP promotes cardiomyocyte proliferation and improves repair after injury, whereas genetic activation of Hippo pathways components, or loss of YAP activity, restrains postnatal cardiomyocyte cell-cycle activity and growth[29,30].

Exogenous remuscularisation is feasible but remains limited by safety and maturation. Transplantation of human embryonic stem cell-derived cardiomyocytes into infarcted non-human primate hearts improves function, yet early engraftment is accompanied by ventricular arrhythmia, highlighting the need to couple new muscle formation with timely electrical and mechanical maturation.[31].

2.3.2 Electromechanical stability

Engraftment studies in large animals show that new myocardium must integrate electrically and mechanically with host tissue to be beneficial. In non-human primates and pigs, transplantation of human pluripotent stem cell-derived cardiomyocytes generates substantial grafts and improves function. Nevertheless, early engraftment is frequently complicated by ventricular arrhythmias despite evidence of graft-host coupling, indicating that the electrophysiologically immature graft constitutes a pro-arrhythmic substrate [31-34].

At the cellular level, safe integration requires appropriate ion-channel expression and calcium handling, organised gap-junction coupling, notably Connexin-43 at intercalated discs (specialised cell-cell junctional complexes that mechanically and electrically couple adjacent cardiomyocytes), and development of transverse tubules alongside aligned myofibrils. Strategies that accelerate these properties in engineered tissues can reduce the immaturity that contributes to arrhythmia risk[35], but achieving durable integration with host tissue remains a key challenge.

At the tissue scale, impulse propagation reflects myocardial fibre orientation, integrity of the His-Purkinje and ventricular conduction pathways, and continuity of excitable myocardium. Fibrosis and patches of low excitability at the graft-host interface interrupt current flow and create discontinuities. Following MI, the border zone often supports slow, zig-zag conduction that predisposes to unidirectional block and re-entry[36]. Overcoming the conduction disruption is therefore a key element of effective cardiac regeneration.

In neonatal mice post-MI, the His-Purkinje network is reconstituted and aligned with the healed myocardium, whereas non-regenerative stages show disorganisation of conduction fibres and maladaptive remodelling associated with arrhythmogenesis[37]. These observations confirm the importance of preserving, or actively restoring, conduction-system topology in the regenerative setting.

Any remuscularisation strategy should therefore aim for rapid acquisition of adult-like excitability and coupling in nascent cardiomyocytes, together with maintenance or restoration of the conduction system, to minimise pro-arrhythmic substrates.

2.3.3 Angiogenesis

Rapid revascularisation of the infarct zone is characteristic of the regenerative response to MI. In zebrafish, vascular regrowth begins within hours of injury and is instructed by epicardial and endocardial cues, forming a scaffold that precedes and supports cardiomyocyte repopulation; experimental disruption of this process impairs

regeneration[38,39]. Epicardial activation also supplies vascular progenitors and trophic signals in mammals. Thymosin β4 stimulates adult epicardial cells and promotes coronary neovascularisation after injury, offering proof of principle that epicardial programmes can be re-engaged to aid vascular regrowth[40].

Complementing these epicardial and endocardial programmes, cardiomyocyte-derived cues also shape coronary regrowth, as illustrated by VEGF-B biasing neovascularisation toward the endocardial and subendocardial compartments. Developmental *Vegfb* overexpression increases the endocardial contribution to the coronary network, and adult VEGF-B gene transfer around LAD ligation expands subendocardial endothelium and improves post-MI structure and function[41,42].

Enhancer-reporter analyses further show that angiogenic control is lineage- and age-specific: an endocardial VEGFA–MEF2 programme predominates in endocardial-derived vessels, whereas SOXF/RBPJ (Notch-associated) and BMP–SMAD programmes characterise sinus-venosus-derived arterial/venous coronaries[43]. Notably, these developmental programmes are not robustly re-engaged after adult MI, helping to explain limited spontaneous revascularisation.

Alongside capillary angiogenesis, collateral artery formation restores flow by creating artery-to-artery conduits. In neonatal mouse hearts, collaterals arise by “artery reassembly”, wherein arterial endothelial cells migrate along capillaries under CXCL12–CXCR4 guidance; loss of either component impairs collateralisation and regeneration,

while exogenous CXCL12 induces aspects of this programme in adults[44]. In parallel, LECs can establish chemokine gradients (classically CCL21) that drive CCR7-dependent dendritic cell migration towards lymphatics[45]. Any analogous chemokine gradients that govern cardiac macrophage trafficking remain unknown.

2.3.4 Resolution of fibrosis and ECM remodelling

Early matrix deposition limits wall stress and reduces risk of rupture after MI. ScRNA-seq in adult hearts has revealed an activated CTHRC1^{+} fibroblast population that emerges after MI to drive collagen deposition which, when disrupted, results in increased lethality through ventricular rupture[46].

Provisional matrix forms in both regenerative and non-regenerative settings. In the non-regenerative setting, persistence of stiff collagenous matrix, ‘fibrosis’, impairs contraction and predisposes to conduction defect arrhythmias. In regenerative contexts, the ECM is remodelled to permit growth and integration of new tissue. Manipulating matrix composition can therefore alter outcomes, for example, administration of agrin, a component of neonatal ECM, after MI in adult mice reduced scar size and improved function[47].

Hyaluronic acid (HA) is a central ECM component in cardiac injury and regeneration. Its concentration and polymer size govern tissue hydration, viscoelasticity and cell migration, while fragmented low-molecular-weight HA signals via innate immune receptors to amplify inflammation[48,49]; high-molecular-weight HA is generally anti-

inflammatory and supports tissue homeostasis[48,49]. HA participates in cardiac development and repair through receptors including CD44, notably a homologue of the HA receptor LYVE-1 (lymphatic vessel endothelial hyaluronan receptor-1), and RHAMM (Receptor for Hyaluronan-Mediated Motility) to influence cardiomyocyte and fibroblast behaviour and matrix organisation[50]. Although direct comparisons across species and ages are still limited, HA-rich matrices are associated with increased compliance and enhanced cell motility, features that align with regenerative tissue mechanics[51].

2.3.5 Immunological balance

After MI in adult mice, a brief neutrophil-dominated phase is followed by a biphasic monocyte/macrophage response: an early pro-inflammatory Ly6C^{hi} wave peaking around days 2-4 post-injury, then a shift to more reparative Ly6C^{lo} macrophages by day ~4-7. The timing and completeness of this transition largely determine scar quality and functional outcomes [52,53]. By contrast, in the neonate, the inflammatory response is more transient and dominated by tissue-resident macrophages, with little monocyte recruitment, favouring rapid resolution and regeneration[54]. Notably, regenerative neonatal hearts still exhibit an early neutrophil influx that peaks at ~1 day post-injury before rapid clearance[55]. This implies that successful regeneration is compatible with, or perhaps even triggered by, initial acute inflammation.

Adult zebrafish, capable of regeneration, also mount an early, robust, innate immune response followed by rapid clearance and revascularisation. The medaka is a small freshwater teleost fish often contrasted with the zebrafish as a closely related non-

regenerative control. The medaka displays attenuated macrophage recruitment, poor revascularisation, and persistent scarring following cardiac injury and augmenting its innate signalling promotes vascular growth and cardiomyocyte proliferation[56].

Neonatal mammals display a similar dependence on a permissive immune milieu. In neonatal mouse heart, macrophage depletion at P1 abolishes regeneration and impairs neovascularisation, identifying macrophages as necessary effectors of the regenerative programme[55]. Regulatory T cells are reported to support cardiac regeneration: adoptive transfer and loss-of-function experiments demonstrate that Tregs promote neonatal cardiomyocyte proliferation via paracrine factors[57]. B cells have also been implicated: they are required for cardiomyocyte proliferation and regeneration in the neonate, in contrast to pro-inflammatory roles reported for adult B cells after injury[58].

Although responsible for clearance of immune cells in the adult, the role of the cardiac lymphatics in neonatal regeneration remains unresolved. Preliminary work from within our group has suggested early neonatal hearts may exhibit immature lymphatics. Since regeneration in this window relies heavily on tissue-resident macrophages with relatively limited monocyte infiltration, this suggests that lymphatic functions defined in adult repair may not translate directly to the neonatal context.

In summary, the cardiac regenerative response pairs a brief innate immune reaction with rapid resolution and pro-angiogenic signalling, driven by immune subsets that promote cardiomyocyte proliferation, neovascularisation, and ECM remodelling with minimal

scar persistence. The next section examines the contribution of macrophages towards this programme, and adult cardiac repair, in greater depth.

2.4 Cardiac macrophages in regeneration and repair

2.4.1 In the adult mouse

MI is a sterile injury that releases damage-associated molecular patterns (DAMPs) from necrotic cardiomyocytes (e.g., ATP, HMGB1, mitochondrial components). These activate pattern-recognition receptors and initiate an innate immune response, with early neutrophil influx followed by recruitment of monocytes/macrophages via chemokine axes CCL2-CCR2 and CX3CL1-CX3CR1. This sequence mirrors canonical wound healing in other tissues[59].

The adult mouse heart at baseline contains heterogenous self-renewing tissue-resident macrophages alongside recruited macrophages. The tissue-resident macrophage population broadly comprises a TIMD4^{+}LYVE-1^{+}MHC-II^{lo}CCR2^{-} subset and TIMD4^{-} LYVE-1^{-}MHC-II^{hi}CCR2- subset[60,61]. A small TIMD4^{-}LYVE-1^{-}MHC-II^{hi}CCR2^{+} monocyte-derived population exists at baseline, which is fully replaced by infiltrating bone marrow-derived monocytes following cardiac injury.

Post-MI, tissue-resident CCR2- macrophages are replaced by two sequential populations of infiltrating CCR2^{+} monocyte-derived macrophages: an initial pro-inflammatory Ly6C^{hi} wave, and a subsequent pro-reparative Ly6C^{lo} wave[52,62]. The initial wave is essential to clear debris and dying cells including cardiomyocytes and neutrophils. Here,

apoptosis refers to programmed cell death with membrane integrity preserved, necrosis to membrane rupture with release of DAMPs, and efferocytosis to macrophage-mediated uptake of apoptotic cells that prevents secondary necrosis[63]. Efferocytosis is central to the transition from inflammation to repair, in part by avoiding DAMP 'unloading' and by polarising macrophages toward pro-resolving 'M2' programmes that support functional recovery[64,65]. MerTK, a macrophage receptor that mediates apoptotic cell uptake, is essential for efferocytosis. In adult mice, MerTK loss increases infarct size and delays resolution after ischaemia-reperfusion MI, whereas preventing MerTK cleavage by the metalloprotease ADAM17 preserves efferocytosis and improves outcomes[66].

High numbers and persistence of immune cells beyond their initial purpose contributes to further fibrosis and pathological remodelling and ultimately progression to heart failure[67]. Prolonged neutrophil retention is especially detrimental to cardiac repair; reactive oxygen species (ROS), protease, and inflammatory cytokine release all promote adverse remodelling, fibrosis, and electrical instability[68].

The endogenous response to MI of increased lymphatic growth attempts to reduce tissue oedema and immune cell load, targeting clearance of neutrophils, macrophages, dendritic cells and T cells, which is necessary for effective tissue repair[9,69]. Enhancement of lymphangiogenesis – the sprouting of new lymphatic vessels – following cardiac injury accelerates resolution of inflammation, increases immune clearance, and improves functional recovery[9]. This is a promising avenue for clinical translation.

2.4.2 In the neonatal mouse

In neonatal mice, the macrophages found in the intact heart at early postnatal stages are primarily tissue-resident CCR2^{-} macrophages that originate from embryonic sources and are maintained through local proliferation[54,70,71]. A substantial proportion of this tissue-resident population is defined as TIMD4^{+}LYVE-1^{+}MHC-II^{lo}, similar to the resident adult populations outlined in the previous section. Studies suggest that CCR2- subsets are non-homogeneous but encompass distinct pro-angiogenic and matrix-remodelling roles. They support endothelial and epicardial-derived cells during vascular plexus expansion, and secrete trophic factors such as VEGFA and IGF-1, contrasting with CCR2^{+} infiltrating monocytes, which are enriched for TNF-α/IL-1β/IL-6-driven inflammatory signalling that promotes chemokine and ROS release[60,72-74].

In contrast to the adult setting, circulating CCR2^{+} monocytes and monocyte-derived CCR2^{+} macrophages contribute minimally to the cardiac monocyte–macrophage population at these early stages[54,71]. In response to cardiac injury in neonates, tissue-resident CCR2- macrophages expand in number, without additional infiltration of CCR2^{+} monocytes[54,75].

General depletion of phagocytes following clodronate liposome treatment after MI at P1 inhibited cardiac regeneration resulting in fibrotic scar formation with significantly depressed cardiac function[55]. Subsequent work confirmed loss of the tissue-resident macrophage population to be responsible for this effect[54,76]. This lack of regeneration was attributed to impaired coronary angiogenesis[55], which is consistent with the growing

evidence supporting direct and indirect macrophage contributions to blood vessel growth and vascular plexus formation[77].

Between P1 and P7, as the regenerative window closes, there is a shift in the macrophage response to cardiac injury. The tissue-resident pool that proliferates locally at P1 becomes diluted as $CCR2^{+}$ monocyte recruitment increases by P7 to more closely match the adult response. In parallel, macrophage programmes shift. For example, beyond roles in matrix remodelling by phagocytosis of debris and matrix metalloproteinase (MMP) regulation, macrophages can deposit collagen directly[78]. Recent work has also shown that macrophage-derived type V collagen seeds early fibrillar assembly and alignment in the nascent scar prior to myofibroblast activation, and loss of *Col5a1* in $CD68^{+}$ macrophages disrupts this process and worsens ventricular remodelling[79]. In neonates, this pro-fibrotic programme is muted at P1 but emerges by P7, aligning with the transition to scar-forming repair by P7.

2.5 Cardiac Lymphatics and Immune Cell Clearance

2.5.1 Mature cardiac lymphatics

During adult homeostasis, the cardiac lymphatics function to modulate tissue fluid and immune surveillance, analogous to the systemic lymphatics that pervade the body. Following injury, such as myocardial infarction (MI), they undergo lymphangiogenesis by growing and sprouting into the infarcted area[9,69,80,81]. The epicardium and pro-inflammatory macrophages secrete vascular endothelial growth factor-C (VEGFC), which drives lymphangiogenesis and extensive remodelling of the cardiac lymphatic network[9,81]. The direction of lymphatic drainage in the heart is from subendocardial

lymphatics towards the subepicardial lymphatics, eventually leading to the mediastinal lymph nodes (MLNs)[82].

The inadequacy of adult lymphangiogenic response has prompted attempts to increase lymphangiogenesis and lymphatic function in the injured heart. Augmentation of the lymphangiogenic response with administration of recombinant VEGFC-C156S, which specifically interacts with VEGFR3, improves cardiac function after MI in animal models, as assessed by echocardiography and cine-MRI [9,81]. Intraperitoneal injection of recombinant VEGFC-C156S after MI in mice increased macrophage clearance via a LYVE-1-dependent mechanism[9].

The lymphatic endothelium is distinguished by specialised intercellular junctions that regulate fluid and cell entry. In initial (capillary) lymphatics, junctions are 'button-like', discontinuous, punctate contacts between oak-leaf-shaped endothelial cells, whereas in collecting lymphatics the junctions are continuous and 'zipper-like', maintaining barrier integrity[83,84]. Buttons consist of focal adherens and tight junction proteins (VE-cadherin, claudin-5, occludin, others) spaced at ~3 μm intervals, flanking narrower flap-like openings through which interstitial fluid, macromolecules, and immune cells access the lumen. These flaps act like primary valves for ingress without requiring wide disruption of cell-cell junctions[84].

2.5.2 Developing cardiac lymphatics

- The lymphatic endothelium is specified during embryogenesis by *Prox1*, which drives venous endothelial cells towards a lymphatic fate. Lineage-tracing studies in mouse embryos show that $PROX1^{+}$ lymphatic endothelial progenitors are specified

within the venous endothelium of the cardinal vein, before exiting the vein to form the jugular lymph sacs, from which lymphatic vessels subsequently sprout and migrate to form the nascent lymphatic network[85]. Beyond this programme, multiple studies also indicate possible non-venous contributions[86]. In the heart, LEC origins are mixed. While a substantial proportion arises from TIE2^{+} endothelium, ventral cardiac lymphatics receive additional input from other non-venous lineages[87,88].

Lineage-tracing and single-cell studies have revised the venous-only model by showing that paraxial mesoderm (PAX3^{+})-derived progenitors make a major contribution to LECs across multiple organs; conditional deletion of *Prox1* in this lineage impairs lymphatic development[89]. Complementary data identify an *Etv2*$^{+}$*Prox1*$^{+}$ mesenchymal progenitor pool of paraxial origin that can specify LECs directly, without a venous intermediate[90]. In the heart, venous and non-venous sources coexist: venous TIE2^{+} endothelium supplies a substantial fraction, while ventral/outflow-tract–adjacent lymphatics receive additional non-venous inputs, including cardiopharyngeal/paraxial mesoderm–derived progenitors[80,91].

LEC growth and patterning are largely driven by VEGF-C/VEGFR3 signalling; in the developing and injured heart, VEGF-C sources include the epicardium and myeloid cells[92,93]. Additionally, it has been shown that myeloid efferocytosis induces *Vegfc* expression and promotes lymphangiogenesis, suggesting a mechanistic link between debris clearance and lymphatic growth that may extend to development[94].

Although lymphatic capillaries and collecting vessels are both lined by lymphatic endothelium, their junctional architecture is functionally specialised: initial (capillary) lymphatics typically display discontinuous “button” junctions[83,84]. In button junctions, tight junction proteins (e.g., VE-cadherin, claudin, ZO-1) are arranged in short segments, anchoring overlapping endothelial flaps to create permissive entry routes for interstitial fluid and immune cells[83,84,95]. In contrast, the tight junctions in collecting lymphatics are arranged continuously in “zipper” junctions that support barrier function[83,84]. Live-cell imaging supports the view that leucocytes, notably dendritic cells, enter via preformed portals in the discontinuous perilymphatic basement membrane and traverse button junctions, rather than by protease-dependent breaching of intact junctions[95].

Developmentally, these junctional states are not fixed. Embryonic and early neonatal initial lymphatics are predominantly zippered, with a transition to button junctions taking place postnatally[96]. This is particularly well characterised in the airway and diaphragm lymphatics, where button abundance increases sharply around birth and continues to mature through early postnatal life[96]. In the intestine, lacteals similarly undergo postnatal junctional remodelling, and pathological or experimentally-induced zippering, which reduces lacteal permeability to chylomicrons, linking junctional state directly to lipid uptake and systemic metabolism[97]. Mechanistically, developmental button junction formation is under active control: VEGFR3 signalling is required during a critical postnatal window for button formation, but becomes less essential for maintenance once buttons are established[98].

Recent intravital imaging has introduced further complexity to the button-zipper paradigm. Capillary LECs exhibit a characteristic 'oak-leaf' / 'jigsaw' geometry, and longitudinal intravital imaging demonstrates that their overlapping borders and associated VE-cadherin configurations dynamically remodel in vivo during homeostasis and in response to acute interstitial fluid loading[99]. Recent perspectives therefore consider buttons and zippers as opposite ends of a dynamic continuum with multiple intermediate stages[99]. Despite this, delineation of junctions as either buttons or zippers remains a useful approximation of underlying function[83,84].

In the murine heart, the embryonic lymphatic network is largely subepicardial, whereas postnatal lymphangiogenesis expands the plexus from the subepicardium into the myocardium with a base-to-apex gradient[88,100]. Preliminary data in our group suggests functional maturity is only acquired after birth[101].

2.6 LYVE-1 is a lymphatic endothelium receptor and homologue of CD44

2.6.1 LYVE-1 functions to facilitate transmigration into lymphatics

LYVE-1 is highly expressed at the surface of initial lymphatics and interacts specifically with the ubiquitous glycosaminoglycan polymer hyaluronan that coats the surface of phagocytic immune cells, where it facilitates vessel entry[102-105]. Engagement of LYVE-1 with the long chains of hyaluronan involves an unusual sliding interaction that mediates the docking and transmigration of dendritic cells and macrophages to dermal lymphatic vessels[103,104,106,107], and has a comparable role in the adult mouse heart where it is required for clearance of macrophages following injury[9].

The hyaluronan receptor LYVE-1 has been implicated as playing a significant role in immune cell trafficking following cardiac injury[9]. LYVE-1 is a glycoprotein receptor, homologous to CD44 and expressed in LECs, tissue-resident (TR) macrophages, pulmonary endothelium, and the sinusoid endothelia of the liver and spleen[102]. LEC LYVE-1 has an established role in facilitating immune clearance, specifically involved in the docking of macrophages and dendritic cells prior to intravasation[102].

2.6.2 *Lyve1* knockout worsens outcomes post-MI in the adult mouse

In adult mice, LEC LYVE-1 is necessary for immune clearance following ischaemic injury. VEGF-C is released from cardiac macrophages post-MI, and enhancement of this response with exogenous VEGF-C stimulates lymphangiogenesis, increasing immune clearance and improving functional recovery via a LYVE-1-dependent mechanism[9]. Constitutive global deletion of *Lyve1* prevents docking and transit of leukocytes through LECs post-MI, exacerbating chronic inflammation and cardiac dysfunction[9]. Curiously, the immune cells retained post-MI within the hearts of *Lyve1*$^{-/-}$ mice included neutrophils. This is surprising given neutrophil transit into the lymphatics is via a mechanism independent of LYVE-1; neutrophils do not express a surface glycocalyx for trafficking via LYVE-1, and instead adhere to LECs via β2-integrins before passage mediated by lipoxins and MMPs[108]. Moreover, the persistence of high numbers of neutrophils amidst a higher concentration of retained, non-trafficked, macrophages in *Lyve1*$^{-/-}$ mice points to a potential failure of efferocytosis – phagocytosis of neutrophils by LYVE-1 deficient macrophages. This forms the basis for the secondary hypothesis of this thesis.

2.6.3 *Lyve1* knockout unexpectedly impairs neonatal cardiac regeneration

In contrast to the adult, previous unpublished work from the group has suggested immune clearance from the injured heart does not occur in the neonatal mouse at P1 due to the impermeability of the lymphatics at this early stage due to the predominance of impermeable "zipper-like" endothelial cell junctions, relative to permeable "button-like" junctions. Despite this, global loss of *Lyve1* still impaired cardiac regeneration post-MI at P1 at the level of reduced cardiac function as determined by MRI, implying the effect is mediated by loss of macrophage *Lyve1*, distinct from the role LYVE-1 plays in immune clearance on the adult lymphatic endothelium[101].

2.6.4 LYVE-1 is also expressed on macrophages

Thus far, LYVE-1 has been discussed in the context of lymphatic endothelium. A subset of tissue-resident macrophages also expresses LYVE-1 (Figure 2-1). In the mouse heart, resident macrophages largely comprise a LYVE-1^{+}MHC-II^{lo}CCR2^{-} population of embryonic origin that self-renew and support regeneration after neonatal MI. The function of LYVE-1 in these macrophages remains unclear and their function in the heart is entirely uninvestigated.

Across organs, LYVE-1^{+} macrophages occupy perivascular niches and display conserved, low-inflammatory, tissue-maintenance programmes. Single-cell and fate-mapping studies define two broad interstitial macrophage classes: LYVE-1^{+}MHC-II^{lo} perivascular cells and LYVE-1^{-}MHC-II^{hi} parenchymal cells, with the former enriched for vascular-stabilising and matrix-remodelling genes[109,110].

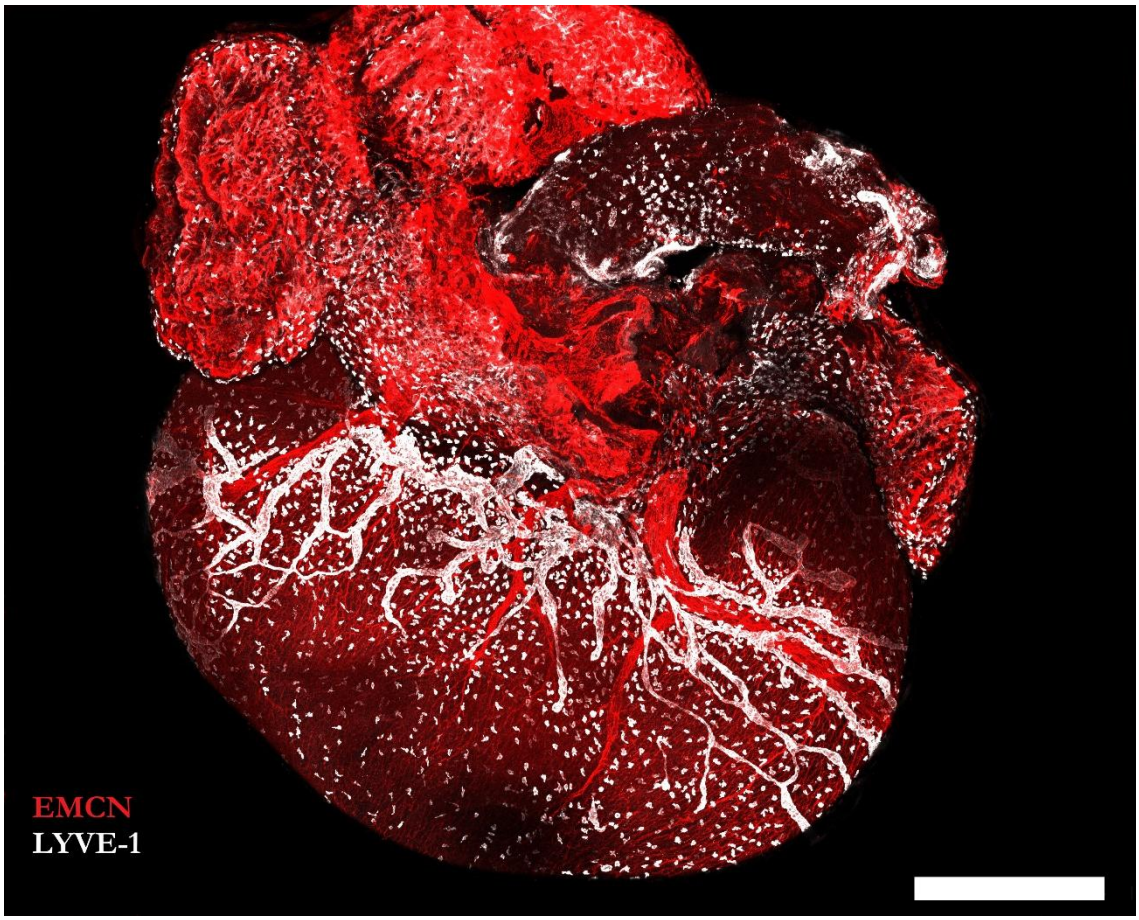

Figure 2-1. E18.5 heart stained for LYVE-1 and EMCN.

LYVE-1 (white) marks lymphatic vessels and macrophages; endomucin/EMCN (red) labels venous endothelium. Sample was optically cleared and acquired as a tile-scan confocal maximum-intensity projection. Scale bar: 0.5 mm. Image captured by Dr K. Klaourakis.

2.6.5 Mechanistic insight from CD44^{+} macrophages

Several macrophage subsets express CD44, a HA receptor and homologue of LYVE-1, sharing conserved HA-binding motifs. Insight into CD44 biology therefore offers a mechanistic template for hypothesising LYVE-1 functions in macrophages[111,112].

CD44 governs cell-matrix adhesion and migration in HA-rich tissues and supports leukocyte trafficking/retention[105]. In dendritic cells, CD44 anchors the pericellular HA glycocalyx, and loss of CD44 disrupts HA retention, impairs motility and reduces

phagocytic competence, directly linking HA binding to migratory and uptake functions[105].

In macrophages, CD44 participates in phagocytosis/efferocytosis-adjacent pathways: HA engagement and CD44 signalling enhance complement-receptor-mediated particle uptake, and CD44 can itself act as a competent phagocytic receptor[113,114].

2.7 Thesis Rationale

2.7.1 Hypothesis

The central hypothesis of this thesis is:

Immature lymphatics in the early neonatal infarcted mouse heart do not function to clear macrophages, enabling retention of pro-regenerative tissue-resident macrophages. Furthermore, these macrophages require the hyaluronic acid receptor LYVE-1 to support effective cardiac regeneration.

The secondary hypothesis of this thesis is:

Macrophage LYVE-1 plays an essential role in adult tissue repair via the regulation of phagocytosis of neutrophils by infiltrating macrophages in the injured adult heart.

2.7.2 Project Aims

The central aims of this thesis are:

Tissue-Resident Macrophage LYVE-1 in Neonatal Cardiac Regeneration

1. To finalise characterisation of cardiac lymphatic morphological and functional maturity during the first two postnatal weeks.

2. To establish whether the impaired regenerative response observed following MI in *Lyve1*$^{-/-}$ neonatal mice is attributable to loss of LYVE-1 on macrophages, rather than lymphatics.
3. To define a likely mechanism for how loss of LYVE-1 on macrophages impairs the regenerative response.

Infiltrating Macrophage LYVE-1 in Adult Cardiac Repair

4. To establish whether expression of *Lyve1* by macrophages is required for effective neutrophil clearance following MI in the adult mouse.

2.7.3 Achievement of Aims

1. Confocal imaging of cardiac lymphatics between P1-P14 allowed quantification of junction types, revealing morphological immaturity at P1. Confocal imaging of mediastinal lymph nodes in CD68-GFP/CX3CR1-GFP mice revealed reduced clearance of macrophages following MI at P1 compared to MI at P7. scRNA-seq analysis revealed shifts in LEC gene expression across the first postnatal week.

2. *Lyve1* was conditionally knocked down in macrophages following MI at P2. Histological and functional readouts recapitulated observations from global *Lyve1* at the same stage, attributing this effect to LYVE-1 on macrophages, and not lymphatics.

3. Following MI, *Lyve1*$^{-/-}$ macrophages more highly expressed apoptotic markers than equivalent wildtype populations. Confocal imaging revealed an apparent defect in the hyaluronan glycocalyx of *Lyve1*$^{-/-}$ macrophages, possibly exposing pro-apoptotic membrane elements.

4. Preliminary flow cytometry analysis following adult MI demonstrates increased macrophage apoptosis and neutrophil persistence in conditional macrophage-specific *Lyve1* knockout.

A summary of findings from this work are presented in Figure 2-2.

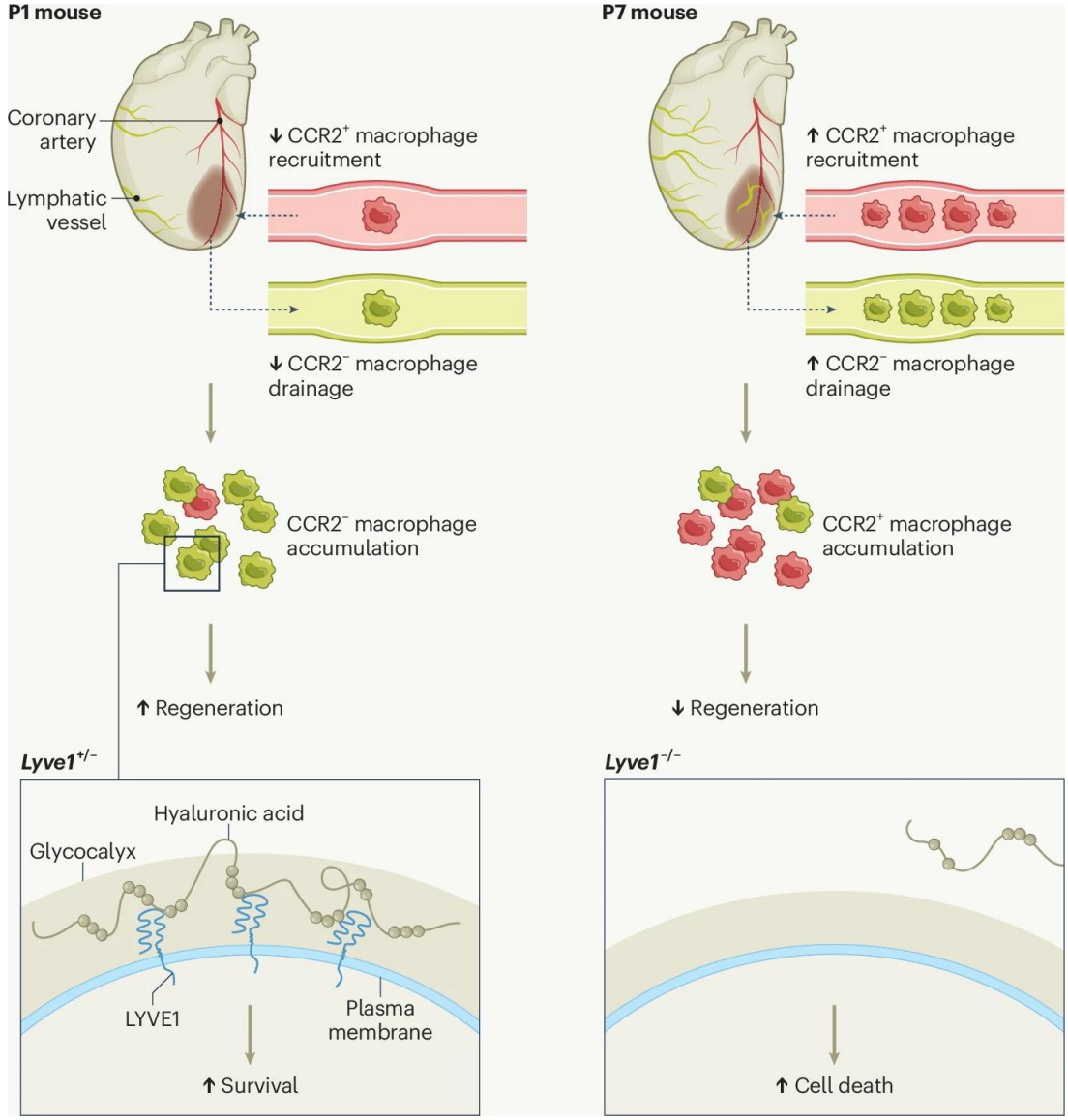

Figure 2-2. Summary of findings.

Adapted from Koopmans and van Rooij[115].

3 MATERIALS AND METHODS

3.1 Animal Work

3.1.1 Mouse Strains

The following mouse strains were used for this work: *Lyve1*$^{-/-}$[116], *hCd68-eGFP*[117], *CX3CR1-eGFP*[118,119], *hCd68-CreERT2* [120], Gt(ROSA)26Sor$^{tm9(CAG-tdTomato)Hze}$, *Lyve1*^{flox} (Jackson, DG; unpublished). Breeding was carried out using only *Cre*$^{+}$ males for all Cre strains. Mice were cared for and housed by Oxford University Biomedical Services. Mice were maintained in individually ventilated cages (IVCs) and ventilated racks at 22°C and 55% humidity. For experiments where wildtype mice were required C57BL/6 or CD1 (Charles River Laboratories) when indicated, strains were used. All animal experiments were carried out according to UK Home Office project licences PPL PC013B246, PDDE89C84 and PP3194787 and were compliant with the UK Animals (Scientific Procedures) Act 1986.

3.1.2 Timed Matings

To generate embryos, female mice were paired with male studs and were checked for vaginal plugs each morning. The day the vaginal plug was observed was designated as embryonic day 0.5 (E0.5).

3.1.3 Neonatal Heart Dissection

Neonatal mice were sacrificed by schedule 1 cervical dislocation and the heart was removed. Hearts collected for immunostaining were washed in ice cold PBS prior to fixation. Hearts for flow cytometry were washed in ice cold Hank's Balanced Salt Solution (HBSS; Life Technologies) prior to tissue digestion. Hearts for RNA extraction

were immediately placed in a cryo-tube (Nunc Thermo Scientific) and the cryo-tube was submerged in liquid nitrogen.

3.1.4 Neonatal Myocardial Infarction Surgery

Myocardial infarction surgery was performed as previously described[121]. At P1, P2, or P7 the litters were removed from the mother and placed in a warm incubator at 35°C. General anaesthesia was induced with 4% isoflurane inhalation in oxygen (1 L/min) for 15 sec. Once unconscious, cardiorespiratory arrest was induced by immersion in ice for 1-2 min. The incision site was cleaned with Hibiscrub and a sterile field constructed with drapes. The skin was cut using surgical scissors in a horizontal incision across the left mid-thorax. Sharp dissecting forceps were used for thoracotomy, close to the costochondral junction, in approximately the 3rd intercostal space. This space was widened using blunt forceps. The heart was manipulated out of the thoracic cavity by applying gentle pressure on the thorax and diaphragm. LAD artery ligation was induced by passing and tying a 7-0 Prolene suture through the anterior wall of the left ventricle. The sham control procedure involved thoracotomy surgery, heart visualisation and suture placement, but no ligature. The ribs and skin were then closed in layers with a 7-0 Prolene suture. The pup was then warmed under an infrared lamp, which led to gradual return of circulation and breathing. When respiration returned, oxygen was administered via nose cone until respiration was regular. The pup was returned to the warmed chamber (35 °C) with the other littermates. After surgery was completed on all pups, and before returning the group to the mother, the animals were covered with faeces from their cage homogenised in warmed water to mask surgical smells and reduce cannibalisation. Surgeries were carried out by research assistants Maria-Alexa Cosma and Sarah Sigal, I assisted by managing induction and anaesthesia.

3.1.5 Tamoxifen Dosing and Administration

Tamoxifen (Sigma Aldrich) was dissolved in peanut oil containing 10% ethanol by shaking overnight at 37°C at a concentration of 13.6 mg/mL. The tamoxifen solution was administered to pups at P1 via intraperitoneal injection at a dose of 0.17 mg/g, in line with the concentration used in previous neonatal work[78]. To reduce maternal stress and prolonged separation from the litter, administration was performed on one-half of the litter at a time, and pups were rolled in cage material prior to their return.

3.2 Molecular Techniques

3.2.1 DNA extraction

Ear biopsies from adult mice and tissue from embryos/neonates were collected for genotyping. The genomic DNA was extracted and amplified using the REDExtract-N-AmpTM Tissue PCR Kit Protocol (Merck). The tissue was incubated in a mix of 100 µL Extraction Solution and 25 µL Tissue Preparation Solution for 10 min at room temperature, followed by a 5 min incubation at 95°C. Immediately, 100 µL Neutralization Solution were added and the mix was vortexed.

3.2.2 Polymerase chain reaction (PCR)

Extracted DNA was used for genotyping using PCR. The sequence of the primers used is displayed in Table 3-1. The following reagents were used to set up the PCR reactions: 10 µL REDExtract-N-Amp™ PCR Reaction Mix, 0.5 µM of each primer, 4 µL tissue extract and Milli-Q water until total reaction volume of 20 µL. Thermal cycling was carried out in a Veriti^{TM} 96-well thermal cycler (Applied Biosystems). A positive control sample of known genotype was included for each genotype being tested.

Table 3-1 PCR primers for genotyping

Gene (size)	**Primer 1**	**Primer 2**	**Primer 3**
Lyve1$^{-/-}$ (381bp mutant, 310bp control)	TCACTCCTATTG AACAGTACC	TCATTCTCAGTA TTGTTTTGCC	CGTGAAAAGGT GAGGTTG
Cre	GCG GTC TGG CAG TAA AAA CTA TC	GTG AAA CAG CAT TGC TGT CAC TT	
Lyve1^{flox}	CAATGTTCATAA CCTTGGTTTGCT CCTTG	AAGGGCTTGGG AAGCGTCCAAG	
GFP	CAGCCCTCTCTT GGAAAGGAGG	TTCTCGGCTCTG TGAATGACA	

3.2.3 Agarose gel electrophoresis

Following PCR amplification, the DNA was separated on 1.5% agarose gel. 1.5 g of agarose (Sigma Aldrich, UK) was dissolved in 100 mL of TBE buffer by heating the mix in a microwave. For UV visualisation of DNA, 5 µL of GelRed (VWR) was added to the agarose gel before it was poured into moulds and allowed to set. An electric potential of 160 V was passed across the gel for 35 min to allow separation of bands to distinguish between genotypes. Gels were visualised in a UV box.

3.2.4 RNA extraction from tissue

RNA was isolated from snap frozen tissue samples using TRIzol reagent (Thermo Fisher Scientific). Tissue was homogenised in 750 µL of TRIzol solution using a manual homogenizer and a 21G sterile needle (Becton Dickinson). After being incubated for 5 min at room temperature, 200 µL of chloroform was added to the samples. Samples were then mixed by hand and incubated for 15 min at room temperature. Following incubation, samples were centrifuged at 11,000 rpm for 15 min at 4°C, which causes phase separation. The organic phase contains the lipids, the interface contains DNA, and the aqueous phase contains RNA. The top aqueous layer was transferred into a 1.5 mL tube, while the organic layer was discarded. To precipitate RNA, 500 µL isopropanol were added to the samples which were then mixed by hand and incubated at 4°C overnight. Following the incubation, the samples were centrifuged at 11,000 rpm for 10 min, which produced an RNA containing pellet. The pellet was washed with 1 mL of 75% ethanol (EtOH) before spinning at 9,000 rpm for 5 min at 4°C. The pellet was air-dried for 10 min and resuspended in diethyl pyrocarbonate (DEPC)-treated water. A Nanodrop2000 (Thermo Fisher Scientific) was used to measure RNA amount and concentration.

3.2.5 Complementary DNA (cDNA) synthesis

cDNA was synthesized from extracted RNA for use in real-time quantitative PCR (qRT-PCR). Reactions were prepared in RNase free 0.6 mL tubes (Thermo Fisher Scientific) using the following reagents: 1 µg RNA made up to a volume of 8.5 µL with DEPC-water, 0.5µL of random primers (20 µg/mL; Promega), 1 µL dNTPs (from 10 mM, GE Healthcare), 2 µL MgCl2 (25 mM, Thermo Scientific), 2 µL Dithiothreitol (DTT, 0.1 M, Life Technologies), 1 µL RNasin® plus RNase inhibitor (Promega), 4 µL 5X FS Buffer (Life Technologies) and 1 µL of SuperScript® III Reverse Transcriptase (Life

Technologies). A Veriti™ 96-well thermal cycler (Applied Biosystems) was used to run the reaction at 25°C for 10 min, 42°C for 50 min and 70°C for 15 min, before cooling to 4°C. Following cDNA synthesis samples were diluted to 4 ng/µL in DEPC treated-water and stored at 4°C prior (short-term) to use in qRT-PCR experiments.

3.2.6 Real-time quantitative PCR

Relative mRNA expression levels from genes of interest were quantified using qRT-PCR. Primer sequences are displayed in Table 3-2. MicroAmp™ Fast Optical 96-well 0.1 mL reaction plates (Thermo Fisher Scientific), were used to set up reactions which were composed of the following reagents: 8 ng cDNA, 13 µL Fast SYBRGreen Master Mix (Thermo Fisher Scientific), 6.5 µL DEPC treated-water, and 0.5 µM of each primer. All samples were run in triplicate and a no-cDNA negative control well was included for each gene analysed. Reactions were run on a ViiA™ 7 Real-Time PCR System (Thermo Fisher Scientific) with thermal cycles of 95°C for 15 seconds: 40 cycles of 95°C for 3 seconds and 60°C for 1 minute. Melt curves were included to confirm that no unspecific amplification products such as primer-dimers were produced with each primer sets used.

Cycle Threshold (Ct) values were obtained and exported to Microsoft Excel for analysis. The comparative cycle threshold method was used to calculate relative normalised gene expression (2^ΔΔCt). First, the mean Ct of the technical triplicates for each condition and gene was calculated. Then, the average Ct of all samples in the control group (Sham for LAD surgery or P0 for development) for each gene was determined. The relative difference (ΔCt) between the average Ct for the control group and the mean Ct for individual sample within each target was calculated. The relative quantities (2^ΔCt) were calculated from the ΔCt. For each biological combination, a normalisation factor was

determined from the mean of the associated housekeeping genes' 2^ΔCt. The housekeeping gene used was *Rpl13a*. The 2^ΔΔCt for each target gene was then calculated per sample by dividing the 2^ΔCt by the normalisation factor. The average 2^ΔΔCt for each biological group was then calculated using the mean. Statistical analysis and visualisation of qPCR data was done using the ΔΔCt (i.e., Log2(Fold Change)) values.

Table 3-2 Primers for qRT-PCR

Gene	**Forward**	**Reverse**
Lyve1	GGCTTTGAGACTTGCAGCTATG	GCAGGAGTTAACCCAGGTG
Reln	GGACTAAGAATGCTTATTTCC	GGAAGTAGAATTCATCCATCAG
Itgb1	CTCCAGAAGGTGGCTTTGATGC	GTGAAACCCAGCATCCGTGGAA
Rac1	ACAGATTACGCCCCCTATCCT	AATGATGCAGGACTCACAAGG
Cd36	GAGCCATCTTTGAGCCTTCA	TCAGATCCGAACACAGCGTA
Rpl13a	CATAGGAAGCTGGGAGCAAG	GCCCTCCAATCAGTCTTCTG

3.3 Immunofluorescent Staining and Histology

3.3.1 Whole-Mount Tissue Clearing – CUBIC

Whole hearts were cleared using CUBIC ('Clear, unobstructed brain and/or body imaging cocktails and computational analysis') by a protocol previously established within the group[37]. Neonatal hearts were shaken in PBS for 30 minutes before immersion in 4% PFA overnight. Hearts were then washed in PBS at room temperature before incubation with CUBIC-L, shaking at 37°C for 10 days and replacing CUBIC-L solution on alternate days. Hearts were washed with PBS three times for 3hrs before blocking (0.2% Triton X-

100, 2% BSA, 10% donkey serum in PBS). Hearts were incubated with primary antibodies for 5 days at 4°C, washed 10x in 0.1% Triton X-100 PBS, then incubated with secondary antibodies for 3 days at 4°C. Hearts were then washed 7 times in PBS and moved into CUBIC-R solution and kept shaking for 4 days at room temperature before imaging. Hearts were imaged in CUBIC-R solution directly using a Miltenyi-LaVision light-sheet fluorescence microscope (UltraMicroscope II).

3.3.2 Whole-Mount Tissue Clearing – iDISCO

Whole hearts were cleared using an iDISCO (immunolabelling-enabled three-dimensional imaging of solvent-cleared organs) protocol adapted from previous work[122]. Hearts were dehydrated by methanol/H_2O series (20%, 40%, 60%, 80%, 100%, each 1hr) and pre-treated with 66% dichloromethane 33% methanol at RT overnight. Samples were washed in methanol twice before bleaching in chilled fresh 5% H_2O_2 in methanol, shaking overnight. Hearts were then rehydrated by methanol H_2O series (80%, 60%, 40%, 20%, PBS, 1hr each). Pre-treated samples were washed in 0.2% TritonX-100 PBS before incubation in permeabilization solution (0.2% TritonX-100, 0.3M glycine, 20% DMSO, PBS) for 2 days, shaking at 37°C. Hearts were then moved to blocking solution (0.2% TritonX-100, 6% donkey serum, 10% DMSO, PBS) for 2 days, shaking at 37°C. Hearts were then incubated in primary antibody solution (1:300 in 0.2% Tween-20, 10mg/mL heparin, 3% donkey serum, 5% DMSO, PBS) for 7 days, shaking at 37°C. Samples were then washed 5x1hr in 0.2% Tween-20, 10mg/mL heparin PBS, shaking at RT. Hearts were subsequently incubated in secondary antibody (1: 300 in 0.2% Tween-20, 10mg/mL heparin, 3% donkey serum, PBS) for 7 days, shaking at 37°C, before being washed in 5x1hr 0.2% Tween-20, 10mg/mL heparin PBS. Hearts were then dehydrated in methanol/H_2O series and incubated in 66% dichloromethane 33% methanol for 3hrs.

Samples were then moved to 100% dichloromethane for 2x15 min before incubation in dibenzyl ether for 2 days to clear the tissue. Samples were refractive index-matched by moving to ethyl cinnamate overnight. Whole mount samples were imaged in ethyl cinnamate using a Miltenyi-LaVision light-sheet fluorescence microscope (UltraMicroscope II).

3.3.3 Paraffin Embedding

Hearts for histological and immunofluorescent staining were embedded in paraffin and mounted using standard methods. Briefly, fixed hearts were dehydrated through an ethanol gradient of (50% 1 hour, 70% 1 hour, 90% 1 hour, 100% overnight), and cleared with Histoclear II (National Diagnostics) for 1 hour. Samples were then embedded firstly in a 1:1 mixture of Histoclear II and Paraplast Plus (Sigma Aldrich) at 60°C overnight, then in 100% Paraplast Plus at 60°C overnight before returning to room temperature and setting. 10 μm sections were cut and mounted on to Superfrost slides. Prior to staining, sections were deparaffinised in Histoclear II and a reversed ethanol gradient (100% 3 min, 90% 3 min, 70% 3 min, 50% 3 min) before transfer to PBS.

3.3.4 Cryosectioning

Whole neonatal hearts were fixed in 4% PFA overnight at 4°C. Following fixation, samples were washed three times for 10 min in PBS and then transferred to 30% sucrose and PBS overnight at 4°C. Then, the samples were equilibrated in a 1:1 solution of OCT and 30% sucrose for 1 hour in 4°C. After equilibration the hearts were embedded in 100% OCT and frozen at -80°C. 10-15 μm slices were cut using a cryostat and transferred onto Superfrost Plus slides (VWR). Slides were dried on a slide dryer for 15 min before being rinsed with PBS.

3.3.5 Picrosirius Red Staining

Staining was carried out using Picrosirius Staining kits (Abcam) according to manufacturer's protocol. Sections were hydrated in distilled water and immersed in Picrosirius Red solution for 1 hour before being rinsed in 2 changes of 1% acetic acid followed by 2 changes of absolute ethanol. Sections were then cleared in Histoclear II and mounted with DPX (Sigma Aldrich). Images of sections were obtained using a Nikon Eclipse light microscope. Relative fibrotic area was calculated for serial sections to identify the largest cross-sectional scar area of each heart.

3.3.6 Immunofluorescent staining of tissue sections

Sections underwent permeabilization with 0.5% Triton X-100 (Sigma, UK) for 10 min, followed by two rinses in PBS for 5 min. Then, sections were blocked in blocking solution, composed of 10% serum, 4% bovine serum albumin (BSA) and 0.2% Triton X-100, for 1 hour. The blocking serum was from the same species in which the secondary antibodies were made. Blocking was followed by a 4°C overnight incubation in primary antibody, which was diluted in blocking solution. A list of primary antibodies and the dilutions used are included in Table 3-3. For each primary antibody used, one section was incubated without primary antibody as a secondary antibody alone control. Following primary antibody incubation, sections were washed several times with 0.1% Triton X-100 and incubated with Alexa Fluor-conjugated secondary antibodies for 1 hour at room temperature in the dark. All secondary antibodies were diluted in PBS; a list of the secondary antibodies used is included in Table 3-4. Following incubation in secondary antibody, the slides were washed several times in 0.1% Triton X-100, with DAPI included in the final 15 min wash. A small amount of 50:50 glycerol/PBS was then added to the slides and a 22x50 mm coverslip (Fisherbrand) was placed on top and sealed with

nail varnish. Immunofluorescent staining was imaged using a Zeiss LSM780, Zeiss LSM880, Zeiss LSM980 or Leica confocal microscope. Z-stack and tiling functions were used when required. Images were processed using ImageJ software[123].

Table 3-3 List of primary antibodies

Primary antibody	**Company/Catalogue number**	**Tissue expression/marker**	**Dilution**	**Species raised in**
VEGFR3	R&D Systems #AF743	Lymphatic endothelium	1:50	Goat
LYVE-1	Angiobio #11-034	Lymphatic endothelium, tissue-resident macrophages, and endocardium	1:400	Rabbit
PODOPLANIN	Fitzgerald #10R-P155A	Lymphatic endothelium and epicardium	1:200	Hamster
PHOSPHO-HISTONE H3 (PH3)	Abcam #AB1791	Proliferation marker	1:200	Rabbit
VE-CADHERIN	R&D Systems #AF1002	Adherens junctions	1:400	Goat
PECAM1	BD Pharmingen #553370	Endothelium	1:200	Rat

CD68	Bio-Rad #MCA1957	Macrophages	1:400	Rat
IBA1	Abcam #ab5076	Macrophages	1:200	Goat
REELIN	R&D Systems #AF3820	Lymphatics	1:200	Goat
ITGB1	Proteintech #12594-1-AP	Endothelium Macrophages	1:200	Rabbit
CC3	Invitrogen #PA5-114687	Apoptotic Cells	1:200	Rabbit
CD44	eBioscience #14-0441-82	Leukocytes Endothelium	1:200	Rat
Hyaluronic Acid Binding Protein (HABP)	Amsbio #AMS.HKD-BC41	Hyaluronic acid	1:300	Biotin conj.

Table 3-4 List of secondary antibodies

Secondary antibody	**Supplier**	**Dilution**
AlexaFluor goat α-rabbit 405	Invitrogen	1 in 500
AlexaFluor donkey α-rabbit 405	Abcam	1 in 500
AlexaFluor donkey α-rat 488	Invitrogen	1 in 500
AlexaFluor donkey α-goat 488	Invitrogen	1 in 500
AlexaFluor donkey α-goat 555	Abcam	1 in 500
AlexaFluor goat α-rat 594	Invitrogen	1 in 500

AlexaFluor donkey α-goat 647	Invitrogen	1 in 500
AlexaFluor goat α-hamster 647	Invitrogen	1 in 500
AlexaFluor donkey α-rabbit 647	Invitrogen	1 in 500
Streptavidin, Alexa Fluor 488 Conjugate	Invitrogen	1 in 200

3.3.7 Immunofluorescent staining of whole neonatal hearts

Whole neonatal hearts were permeabilised for 1 hour in 4% Triton X-100 and subsequently blocked in blocking solution (2% BSA, 10% serum, 0.2% Triton X-100 in PBS) overnight at 4°C. The blocking serum was from the same species in which the secondary antibodies were made. Samples were incubated with primary antibodies (Table 3-3) diluted in blocking solution for 48 hours at 4°C, then washed ten times for 30 min in PBS. Then, samples were incubated with secondary antibodies (Table 3-4) diluted in PBS overnight at 4°C in the dark. The hearts were washed five times for 15 min in PBS, with DAPI staining included in the last 30 min wash. Immunofluorescent staining was imaged using Zeiss LSM780, Zeiss LSM880, Zeiss LSM980 or Leica confocal microscope, or a Zeiss Z.1 light-sheet microscope. Z-stack and tiling functions were employed to obtain maximum intensity Z-projections of whole hearts. Images were processed using Imaris, Arivis Vision4D and ImageJ software.

3.4 Flow cytometry

3.4.1 Adult cardiac cell isolation

Hearts were cut transversely and rinsed with cold HBSS before transfer into gentleMACS C-Tubes containing cold HBSS on ice. 100 µL Collagenase II solution (final concentration: 200 U/mL) and 5 µL DNase I solution (final concentration: 60 U/mL) was added per tube before agitating at 37°C for 10 minutes. The heart dissociation mixture was then filtered through 40µm cell strainers and rinsed with 2ml HBSS. Tubes were left for 10 minutes to allow tissue pieces to settle, the supernatant was removed and enzymes deactivated with 0.5M EDTA. Remaining heart pieces were refreshed with HBSS, Coll II, DNAse I solution as previously before an additional 37°C agitation. Tubes were run on gentleMACS Octo Dissociator m_heart_02 programme for 1hr before addition of 80 µL 0.5M EDTA and filtration and resuspension of dissociated cardiac cell solution. After second round of centrifugation, pellets were resuspended in 5mL 1X Red Blood Cell Lysis Solution for 3 minutes at room temperature. Following further centrifugation and aspiration of supernatant, cells were separated for counting and the remainder resuspended in 5ml FACS stain buffer (2% FBS/PBS).

3.4.2 Neonatal cardiac cell isolation

Hearts were isolated and the atria were removed, and the ventricles were cut in half. Blood was removed from the ventricular chambers. The ventricles were minced using a sterile scalpel (Swann-Morton) before being processed for dissociation with Miltenyi neonatal heart dissociation kit. The pellet was resuspended in 5 mL 1X red blood cell (RBC) lysis buffer (BioLegend) and was left at room temperature for 10 min. The tubes were then centrifuged again at 350 *g* for 5 min at 4°C and the supernatant was discarded, leaving a pellet. The cell pellet was resuspended in 5 mL 2% FBS/PBS. The tubes were

centrifuged again at 350 *g* for 5 min at 4°C and the supernatant was discarded, leaving a pellet. The pellet containing the cardiac cells was resuspended in 200 µL 2% FBS/PBS.

For single cell RNA sequencing (scRNA-seq), the pellet containing the cardiac cells was resuspended in 200 µL 2% FBS/PBS and transferred to a Falcon 5 mL Round Bottom Polystyrene Test Tube, with a 35 µm nylon mesh Cell Strainer Snap Cap prior to Fluorescence activated cell sorting (FACS) of live cells using 7AAD. Heart dissociation for neonatal scRNA-seq was carried out in collaboration with Dr Susanna Cooper, Riley Group.

3.4.3 Antibody staining

150 µL of the cell suspension were taken for antibody staining, while 25 µL were kept for full negative control and 25 µL for 7AAD only staining. To each cell suspension 2% FBS/PBS were added to a final volume of 200 µL. For the antibody staining, 2.5 µL Fc receptor blocking reagent (Miltenyi Biotech) were added to the suspension and the cell suspension was left on ice for 5 min. Antibodies were then added at the dilutions shown in Table 3-3 and the tubes were incubated at room temperature in the dark for 30 min. 1 mL 2% FBS/PBS was added to each tube and the samples were centrifuged at 350 *g* for 5 min at 4°C to give a cell pellet. The pellet containing the stained cells was then resuspended in 500 µL 2% FBS/PBS and transferred to Falcon® 5 mL Round Bottom Polystyrene Test Tube, with a 35 µm nylon mesh Cell Strainer Snap Cap. Just before flow cytometry, 5 µL 7AAD (1% final concentration) viability staining solution (eBioscience) were added to allow exclusion of dead cells. Flow cytometry quantification and FACS were performed on a FACSAria III cell sorter or a LSRFortessa X20 Analyzer (BD Biosciences). An appropriate gating strategy had previously been set up in pilot studies.

Each experiment included negative and 7AAD only controls. FMO controls were used to correct for spectral overlap. FACS experiments took place at the Oxford Wellcome Centre for Human Genetics Flow Cytometry Facility and the Oxford Jenner Institute.

3.4.4 Sample analysis

Flow cytometry data obtained from the FACSAria III cell sorter and LSRFortessa X20 Analyzer were exported to FlowJo software for further analysis.

3.5 Analysis of Cardiac Function

3.5.1 Cardiac cine magnetic resonance imaging (MRI)

Neonatal cardiac cine-MRI was performed post-MI at day 28 as previously described[15] using a7 T preclinical MR system (Varian) using a 1H four-channel phased array surface receive coil (RAPID Biomedical, Rimpar, Germany). Briefly, mice were anaesthetised with 2% isoflurane in O2, and positioned prone in a custom animal handling system with homeothermic control. Prospectively gated proton cardiac images were acquired with a partial Fourier accelerated spoiled gradient echo CINE sequence (TR 5.9 ms, TE 2.2 ms, 30 kHz bandwidth, 30º FA, approximately 20-30 frames; 3-4 averages) in order to acquire two and four chamber long-axis views and a stack of contiguous 1-mm thick true short-axis images to cover the entire left ventricle (128x128 matrix; 25.6 mm^2 FOV; 0.2 mm resolution in-plane)

3.5.2 MRI data processing

MRI data were processed manually by image analysis with ImageJ. All analysis was performed blind so as wildtype/mutant groups were unknown at the time of image processing. Measurements were calculated as previously described[15] End-diastolic and

end systolic volumes were measured for each slice and summed over the whole heart. Stroke volume was calculated by subtracting the end-systolic volume from the end-diastolic volume. Ejection fraction was calculated by dividing the stroke volume by the end-diastolic volume. End diastolic mass was calculated as the left-ventricular end-diastolic volume multiplied by the myocardial specific gravity (1.05 g/cm^3), end systolic mass was also calculated in this way using the left-ventricular end-systolic volume. Cardiac output was calculated as stroke volume multiplied by heart rate. The relative infarct size was calculated from the average of the endocardial and epicardial circumferential lengths of the thinned, akinetic region of all slices, measured at diastole, and expressed as a percentage of the total myocardial surface.

3.6 Bioinformatics

3.6.1 Single cell RNA sequencing and analysis: 10x Sequencing

All the 10x scRNA library preparation and sequencing was carried out at the Oxford Genomics Centre part of the Wellcome Trust Centre for Human Genetics.

3.6.2 scRNA-seq data processing and analysis

The raw scRNA-seq data were demultiplexed by Dr Adam Braithwaite (Radcliffe Department of Medicine) and Dr Michael Weinberger (Institute of Developmental and Regenerative Medicine) using cellranger mkfastq from the Cell Ranger software suite to generate fastq files. Demultiplexed fastq files were aligned to the mouse mm10/GRCm38 reference transcriptome and gene expression matrix was counted using cellranger count programme. Downstream bioinformatics analysis was performed in R using the package Seurat (v4)[124]. A cut-off was applied to filter out low-quality cells based on the number of genes detected (<500), the number of UMI detected (<250), and the mitochondrial

gene content (>30%) per each cell. Data from all samples were combined, scaled by regressing out S and G2 cell cycle phases, and integrated using the Seurat package. Dimensional reduction of the data was performed by RunUMAP function implemented in the Seurat package. Unsupervised cluster identification was performed *via* the FindClusters function, and cell clusters were further annotated based on expression of known marker genes[125]. Identification of enriched genes in cell clusters and single cell differential expression analysis were performed using Seurat functions FindMarkers and FindAllMarkers, using gene expression detected in > 25% of cells for at least one of the populations being compared, with an absolute Log2(Fold change) > 0.25 as cut-off threshold.

To genetically de-multiplex pooled scRNA-seq samples (n=5 hearts), we re-mapped 10X scRNA-seq reads via minimap[126], called variants via freebayes and counted alleles in each cell via VarTrix, all as part of the souporcell pipeline[127]. Based on the VarTrix output, cells were assigned to donors using vireo[128]. We excluded doublet and unassigned cells from further analysis and performed differential abundance testing of cell neighbourhoods between WT and *Lyve1* KO conditions via miloR[129], building the KNN graph with k=30. This tool represents scRNA-seq data as a k-nearest neighbour graph consisting of partially overlapping cell neighbourhoods that contain an index cell and its nearest neighbour cells. Neighbourhoods are annotated to the cell type that they contain most frequently and a representative sample of neighbourhoods is tested for differential abundance across conditions.

Apoptosis markers were retrieved from MSigDB (HALLMARK APOPTOSIS) and a cumulative expression score was calculated via Seurat's AddModuleScore() function.

Markers used to analyse G1/S and G2/M cell cycle phase transitions[130] are included in the Seurat R package. The CellCycleScoring() function was used to calculate cumulative expression scores of cell cycle markers. Statistical differences in the distribution of single-cell gene expression between conditions were evaluated via the Wilcoxon rank-sum test, and p values were Bonferroni-corrected to account for multiple comparisons.

3.7 Statistical analysis

All statistical analyses were performed using GraphPad Prism 8 software. Comparisons between two groups were made using an unpaired two-tailed T test, this included an F test to confirm the two groups had equal variances. A one-way ANOVA was used to make comparisons between three or more experimental groups that had one independent variable. A two-way ANOVA was used to make comparisons between three or more groups that had been split in two independent variables. Formal a priori power calculations were not feasible for the *hCD68-CreERT2* neonatal MI model because small and variable litter sizes, unpredictable post-MI mortality, and possible genotype-dependent survival differences prevented reliable prospective specification of group sizes and endpoint variance. In all cases a *p-value* of less than or equal to 0.05 was deemed significant.

4 RESULTS I: CLEARANCE AND RETENTION OF LYVE-1$^+$ CARDIAC RESIDENT MACROPHAGES

4.1 Background

In the adult heart, myocardial infarction (MI) triggers a stereotyped, pro-inflammatory response. Neutrophils and CCR2$^+$ Ly6C^{hi} monocytes dominate early, followed by a Ly6C^{lo} reparative phase[52]. Persistence of the inflammatory wave promotes adverse remodelling and clearance of leukocytes is integral to recovery. Augmenting cardiac lymphangiogenesis with exogenous VEGF-C increases clearance of immune cells to mediastinal lymph nodes (MLNs) and subsequently improves function in adult mouse MI models[9].

By contrast, the neonatal response comprises largely locally proliferating yolk sac-derived CCR2- tissue-resident macrophages. In this setting, the role for lymphatic clearance is currently unclear. It can be assumed that prolonged presence of tissue-resident macrophages is not inherently detrimental in the way retained adult infiltrating monocyte-derived macrophages are[54,55,60].

Previous work from the group provided preliminary evidence that cardiac lymphatics are immature across the regenerative window and may not function to clear immune cells at this time[101]. Three-dimensional light-sheet imaging following MI revealed a lack of lymphangiogenesis 7 days post-injury (dpi) at postnatal day 1 (P1), compared to P7 hearts. Furthermore, transfer of splenic *hCD68-eGFP*-labeled monocytes into wildtype neonatal hearts revealed significantly reduced clearance of these cells to MLNs at P1MI7dpi compared to P7. This was supported by preliminary data in *hCD68-eGFP* mice following MI P1 and P7, where an increased number of GFP$^+$ cells were observed in

MLNs at P7 compared to P1. This impaired clearance may be explained, in part, by the maturation status of LEC junctions and the developmental transition from ‘zipper-like’ (impermeable) to ‘button-like’ (permeable) states.

To gain insight into the molecular underpinnings of lymphatic endothelium-macrophage interactions in P1 versus P7, this previous work involved generation of unbiased scRNA-seq datasets from neonatal hearts collected at different timepoints after MI and observed altered LEC-macrophage signalling.

This chapter tests the hypothesis that at P1 the immature junctional architecture of initial lymphatics limits immune-cell egress, favouring retention of tissue-resident macrophages. By P7, lymphatic maturation, coinciding with the onset of monocyte infiltration, makes immune-cell clearance necessary and permits their export.

4.2 Aims

To finalise characterisation of cardiac lymphatic morphological and functional maturity during the first two postnatal weeks.

My aim within this chapter was to complete characterisation of the early postnatal cardiac lymphatics, building on the previous work outlined above in three central areas: (1) to establish the extent of any lymphatic vessel growth from the myocardial surface, (2) to complete and quantify any change in junctional morphology between lymphatic endothelial cells in lymphatic capillary tips, and (3) to establish the capacity of the neonatal lymphatics to traffic tissue-resident macrophages following MI across the regenerative window.

4.3 Results

4.3.1 Morphology of the postnatal cardiac lymphatics P1-P14

4.3.1.1 Tissue clearing for imaging of lymphatics at depth

Clearing of whole P7 hearts was trialled with immunolabelling-enabled three-dimensional imaging of solvent-cleared organs (iDISCO) and with clear, unobstructed body imaging cocktails and computational analysis (CUBIC)[131]. Subsequent imaging was conducted using light-sheet and confocal microscopes to determine the optimal protocol for visualising lymphatics at depth within the dense myocardium. I stained for EMCN and LYVE-1, using EMCN as a positive control to determine whether signal absence at depth could be due to inadequacy of clearance. LYVE-1 staining was inconsistent in CUBIC-cleared hearts (Figure 4-1) and reportedly incompatible with iDISCO, thus I progressed with a stain for the alternative lymphatic marker VEGFR3.

VEGFR3 is a well-established marker of LECs and has been used by many high-impact studies to specifically visualise LECs[132-134]. iDISCO-optical clearing was used to assess lymphatic structure at depth in uninjured wildtype hearts at P1, P7, and P14 (Figure 4-2). This analysis confirmed lymphatics are largely absent at depth throughout the regenerative period, thus supporting previous examination within the group of lymphangiogenesis by whole mount surface staining. The group has previously used whole-mount X-gal staining of *VEGFR3*$^{+/LacZ}$ mice to quantify lymphangiogenesis[80] and I employ VEGFR3 again here as a well-characterised reporter of lymphatic growth as described previously: “The heart of a new-born VEGFR-3$^{+/-}$ mouse reveals large lymphatic vessels at the pericardial surface. In contrast, coronary blood vessels are not

stained. The stained vessels did not contain erythrocytes in sections of newborn skin, confirming their lymphatic nature"[135].

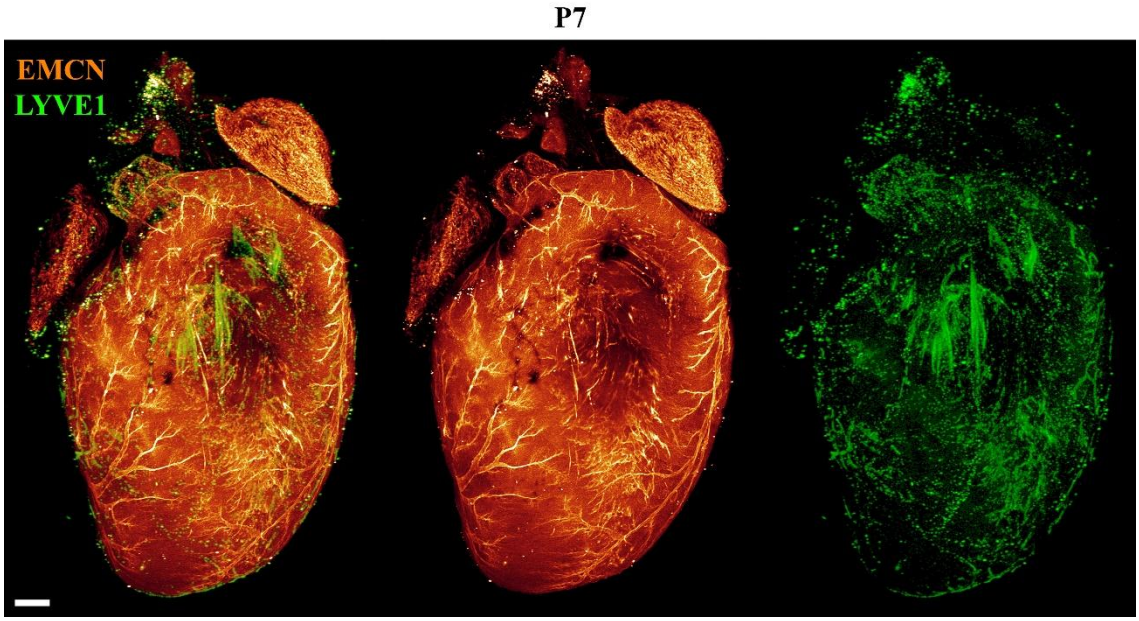

Figure 4-1. CUBIC-cleared uninjured P7 heart.

Whole-mount heart stained with immunofluorescent antibodies against Endomucin (EMCN) and LYVE-1 before imaging with light-sheet microscopy. Scale bar: 200 μm.

The VEGFR3 antibody was incompatible with CUBIC reagent. These compatibility issues motivated a switch to iDISCO as a clearing agent. I cleared P1, P7, and P14 hearts using iDISCO and, by staining for VEGFR3, was able to visualise lymphatics at depth by light-sheet microscope, and surface lymphatics at high magnification with confocal microscopy (Figure 4-2). Having established the paucity of deep lymphatics across P1–P14, I then examined whether junctional maturation at the surface could account for developmental differences in immune egress.

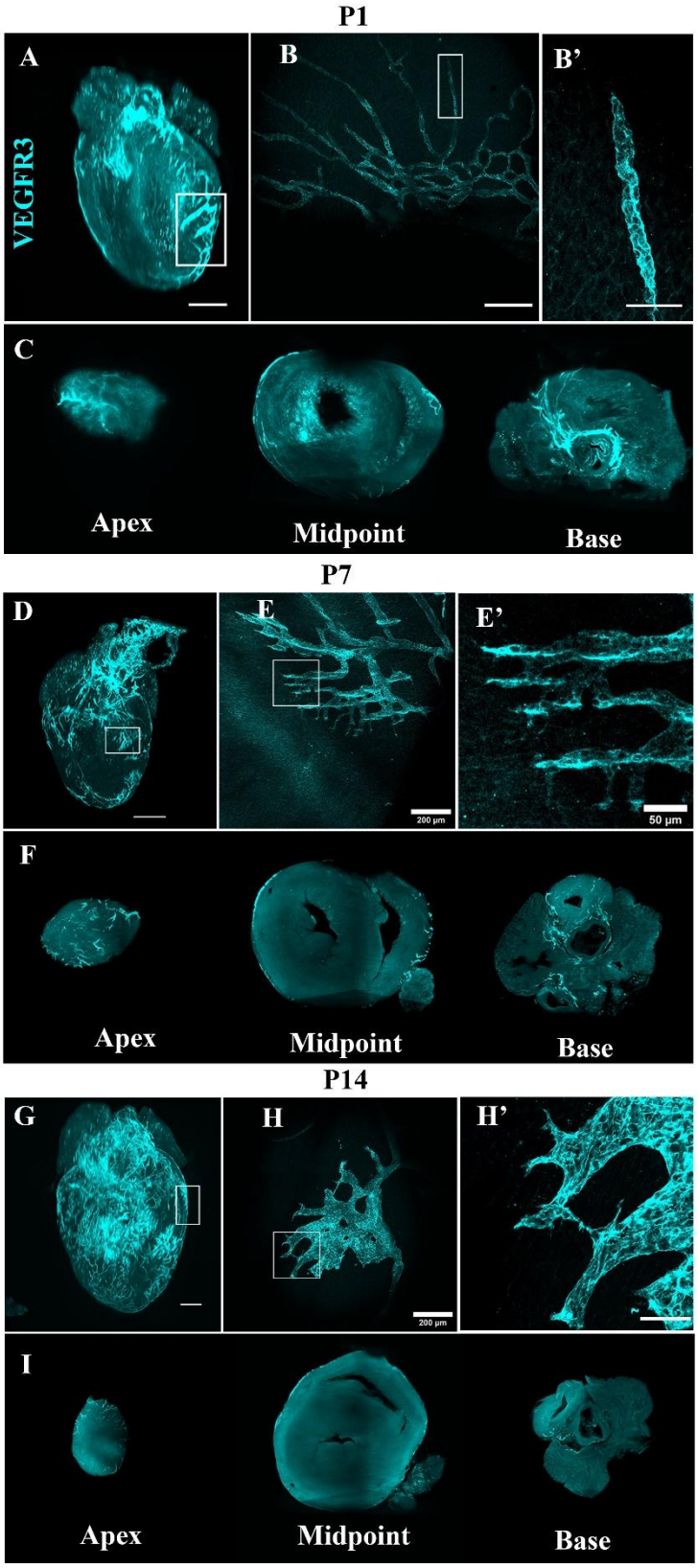

Figure 4-2. iDISCO-cleared hearts: P1, P7, P14.Whole mount hearts were cleared using iDISCO at P1, P7, and P14 and stained for VEGFR3 before imaging with light-sheet microscopy (A-I). Initial lymphatics were identified morphologically (B, B', E, E', H, H'). Representative sections (C, F, I) from the 3-dimensional images (A, D, G) illustrate lymphatics are largely absent at depth. Scale bars: 0.5 mm for A, D, G; 200 µm for B, E, H; 50 µm for magnified views.

The whole-mount iDISCO staining demonstrated co-staining for LYVE-1 and VEGFR3 in lymphatic vessels, albeit with incomplete coverage of LYVE-1 (Figure 4-3).

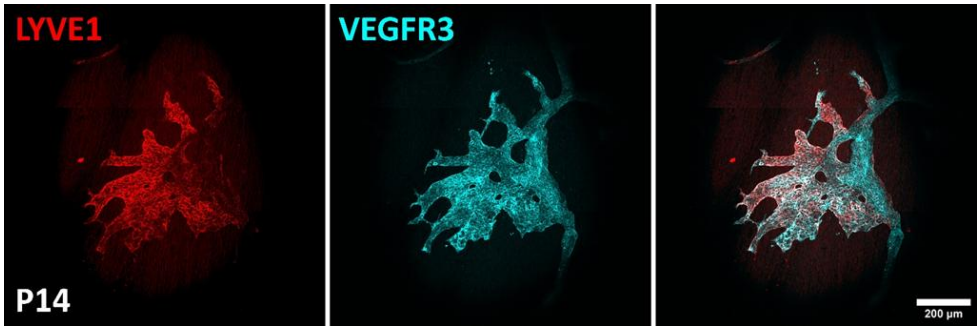

Figure 4-3. Co-staining of surface lymphatics for LYVE-1 and VEGFR3.

Confocal imaging of whole-mount heart surface lymphatics. Representative image from uninjured P14 heart. Scale bar: 200 µm.

4.3.1.2 Developing morphology of lymphatic junctions

LECs have specialised intercellular junctions with different degrees of cell permeability, termed button-like and zipper-like junctions[83]. In the lungs and trachea, the junctions of initial lymphatics undergo transformation during postnatal development, replacing tightly zipper-like with discontinuous, more cell-permeable button-like junctions, comprised from mostly the same junctional proteins[96]. To study the junctions in initial lymphatics of the neonatal heart, I performed comparative immunostaining for VE-Cadherin, whose expression is maintained in zippers, and LYVE-1 using high resolution confocal imaging (Figure 4-4). This analysis was initiated by a previous DPhil Candidate, Dr K. Klaourakis, and here I describe my imaging of additional hearts to ensure reproducibility and permit quantitative analysis, including subsequent statistical analysis.

We employed a whole-mount approach to clearly delineate initial lymphatics from surrounding lymphatic structures. At P1 the initial lymphatics contained predominantly zipper-like junctions with continuous VE-Cadherin expression and no gaps between neighbouring LECs (Figure 4-4A-C). By P7 button junctions were evident, defined as discontinuous ~3 μm gaps in VE-Cadherin expression[83,84], albeit still with a proportion of zippers (Figure 4-4D-F; Figure 4-5), however, by P14 the junctions were predominantly button-like, with discontinuous VE-Cadherin and gaps between adjacent LECs (Figure 4-4G-I). Thus, the transformation from zipper, through intermediate to button junctions occurring between P1-P7 and still ongoing by P14, with the % incidence of each junction type in Figure 4-4, quantified as previously reported[84] representing a dynamic change in junction morphology which continues during later stages of postnatal development. The majority zipper junction phenotype at P1, maintained proportionally through to P7, would effectively exclude immune cell clearance following injury at P1, whereas the appearance of button junctions by P14 corresponds to 7-days post-MI at P7 that supports clearance at this stage, consistent with previous adoptive transfer experiments within the group. I manually quantified multiple image frames across multiple hearts, based on existing literature regarding the morphology and size of these junctions[84]: "Unlike continuous (zipper) junctions, the junctions in initial lymphatics (i.e., buttons) consisted of roughly parallel linear segments of junctional proteins, about 3 μm in length and 3 μm apart along the border of oak-leaf-shaped endothelial cells." The n numbers indicate hearts analysed; 2-4 lymphatic capillary tips were analysed per heart. The definition of continuous versus button-like junctions was based on physical measurements, noting the well-established description of button-like junctions as discontinuous ~3 μm gaps in VE-Cadherin expression.

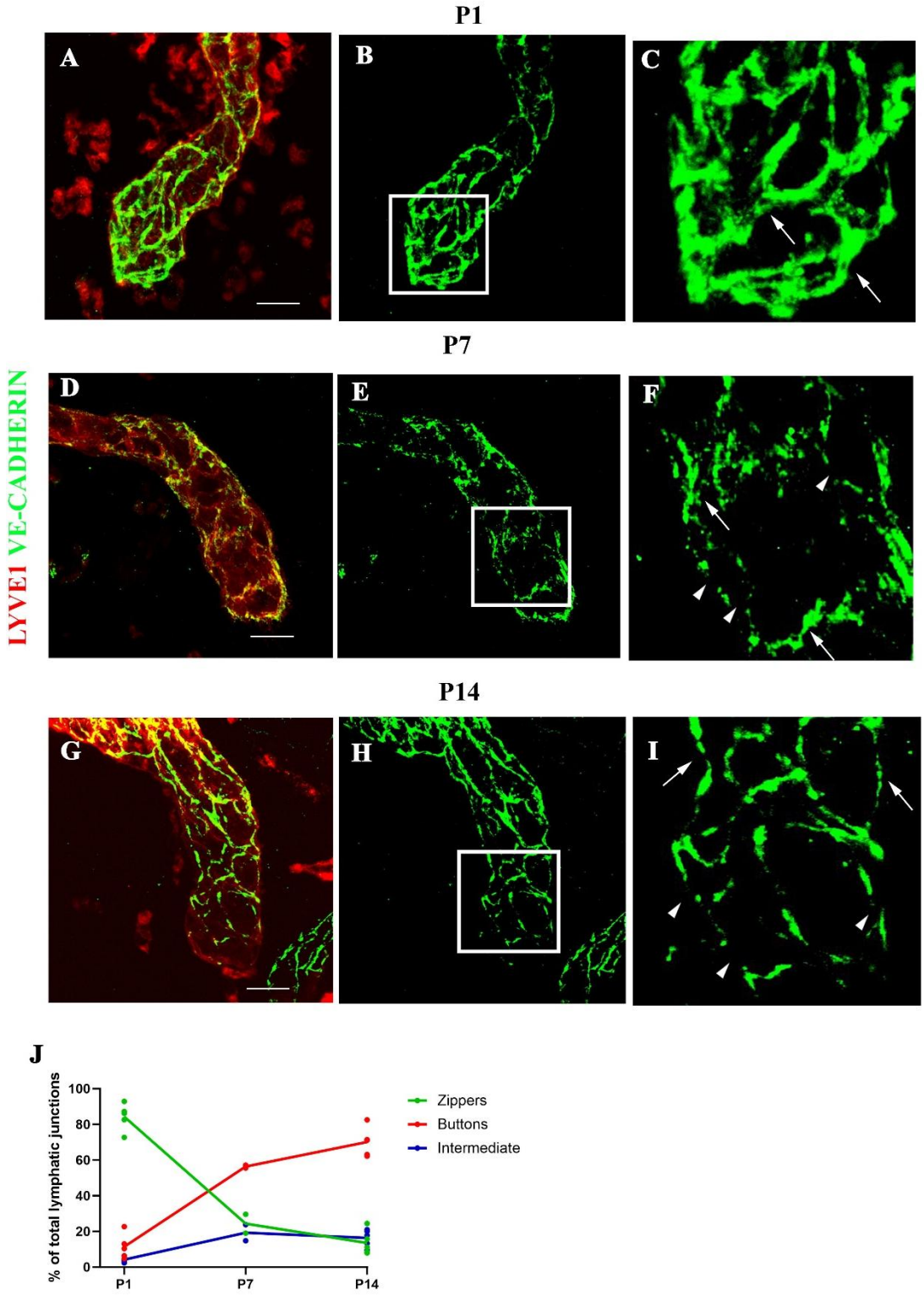

Figure 4-4. Lymphatic button and zipper junctions.

Amendments and quantification of work from K. Klaourakis[101]. High magnification confocal imaging of LECs within vessels stained for VE-Cadherin and LYVE-1 enabled visualisation of cell-cell junctions at different postnatal stages (A-I). The morphology of the junctions at P1 appeared to be continuous, resembling that of zippers (arrows in C). Zipper-like junctions were also observed at P7 (arrows in F) but there was also the emergence of discontinuous button-like

junctions (arrowheads in F) as well as those that were intermediate between zipper and button, indicative of a more cell permeable endothelium. The more complete transformation to button-like junctions was further evident by P14 (arrowheads in I), although some intermediate and zipper-like junctions were still evident at this stage (arrows in I). Quantification of the % incidence of the three junction types (zipper-like, intermediate, and button-like) across the P1-P7-P14 time course (J), reveals the trend in transition from zipper-like (impermeable) to button-like (permeable) during postnatal development. Macrophage morphology also transformed during this two-week period. n = 5 for P1 and P14, n = 2 for P7; lymphatic vessel tips within the visual field were analysed, 2-4 tips per heart. Mean percent was plotted. Scale bars: 20 μm.

The VE-cadherin antibody was validated via robust continuous capillary staining elsewhere in the heart (Figure 4-5). This verifies the 'gaps' in staining observed to reflect differences in morphology, and not technical artefacts. The continuous versus discontinuous VE-cadherin staining is as anticipated, to demarcate zipper versus button junctions respectively, as reported elsewhere in other tissues[83].

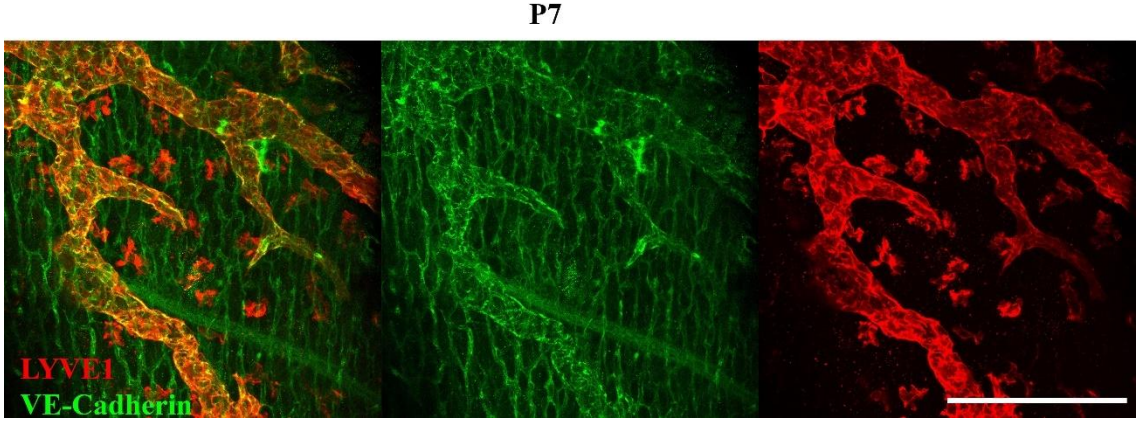

Figure 4-5. Anti-VE-Cadherin antibody robustly targets lymphatics and capillaries.Further representative examples of the button-zipper morphology of cardiac lymphatics at P7. Importantly, these panels also demonstrate robust staining of capillaries with VE-Cadherin. Scale bar: 100 μm.

A representative attempt to visualise the changing ultrastructure across the neonatal period within tissue sections is also included (Figure 4-6). These sections were obtained due to the wider compatibility with immunofluorescent staining compared to whole mount clearing approaches. Staining confirmed observations from 3D samples that VE-

Cadherin stains lymphatic vessels and capillaries, lymphatic vessels were identified by LYVE-1 staining and capillaries and veins were identified using IB4. Positive IB4 staining confirms vessels positive for VE-Cadherin but negative for LYVE-1 are capillaries and not lymphatics lacking LYVE-1 (Figure 4-6). These views are less informative regarding three-dimensional structure which prevents identification of lymphatic capillary tips specifically but nonetheless provide representational evidence of the presence of buttons and zippers throughout. There was greater intensity of VE-Cadherin staining in lymphatic vessels, where the characteristic gaps of button junctions could be observed in select regions. This also reflects what was observed in the whole mount surface images.

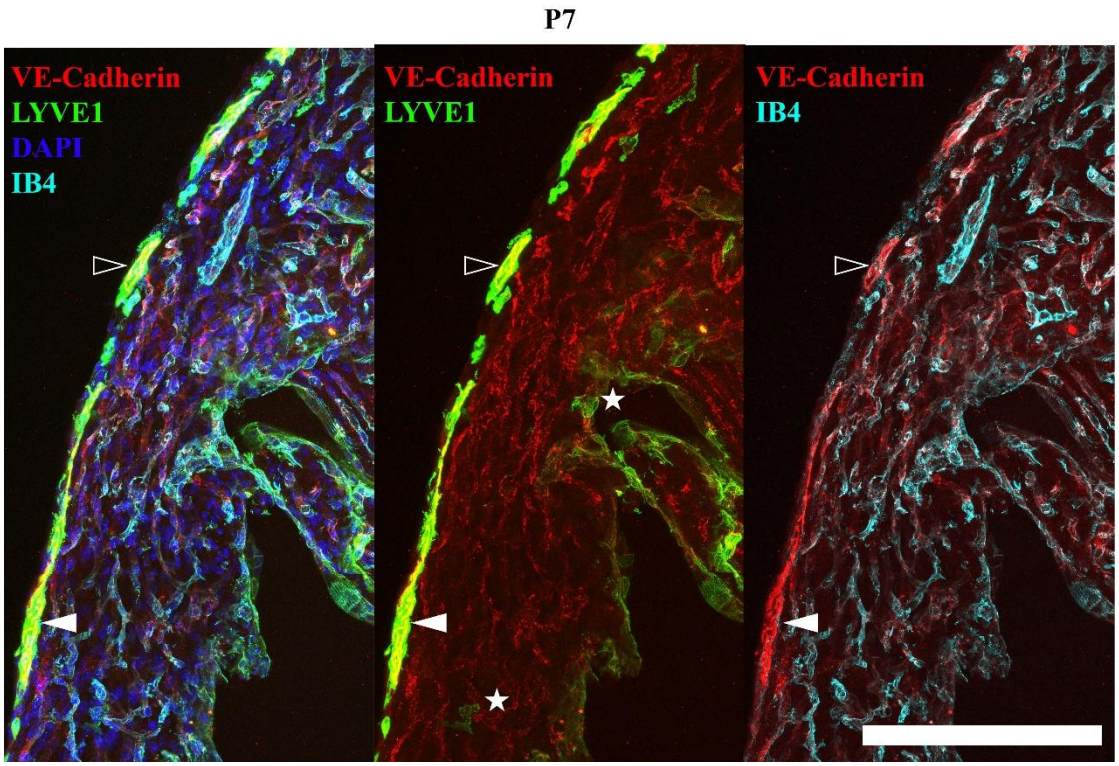

Figure 4-6. Identification of lymphatic ultrastructure in P7 heart sections.

Visualisation of button-like (white arrows) and zipper-like junctions (black arrows) in sections through the heart at P7. Characteristic gaps of button-like junctions are visible. LYVE1+ macrophages are also visible (stars). Staining for VE-Cadherin, LYVE-1, and IB4 facilitated delineation of lymphatic vessels and capillaries. VE-Cadherin stains both lymphatic vessels and

capillaries, while LYVE-1 is selective for lymphatics and IB4 is selective for capillaries and veins. Scar bar: 50 μm.

4.3.2 Single-cell analysis of neonatal cardiac lymphatics

To understand whether differences observed in the lymphangiogenic response and immune-clearance function of cardiac lymphatics after MI at P1 and P7 involves an altered LEC molecular phenotype, analysis was carried out of scRNA-seq collected previously within the group at different time points using the 10X Genomics Chromium platform (Figure 4-7). Hearts from P1 and P7 CD1 mice were harvested by Dr K. Klaourakis 1- and 7- days after MI, along with their corresponding non-infarcted controls, and the six individual cDNA libraries constructed for single cell RNA sequencing. The resulting data were analysed in R using published Seurat pipelines with automated cluster annotation and manual consolidation of published gene markers[125,136] for individual cell types by Dr Michael Weinberger. The objective in assessing lymphatic differential gene expression between P1 and P7 was to identify candidate pathways with a role in the regenerative response at P1.

To conduct pathway enrichment analysis, we re-clustered the existing scRNA-seq data to obtain pooled LEC groups for each condition (Figure 4-7).

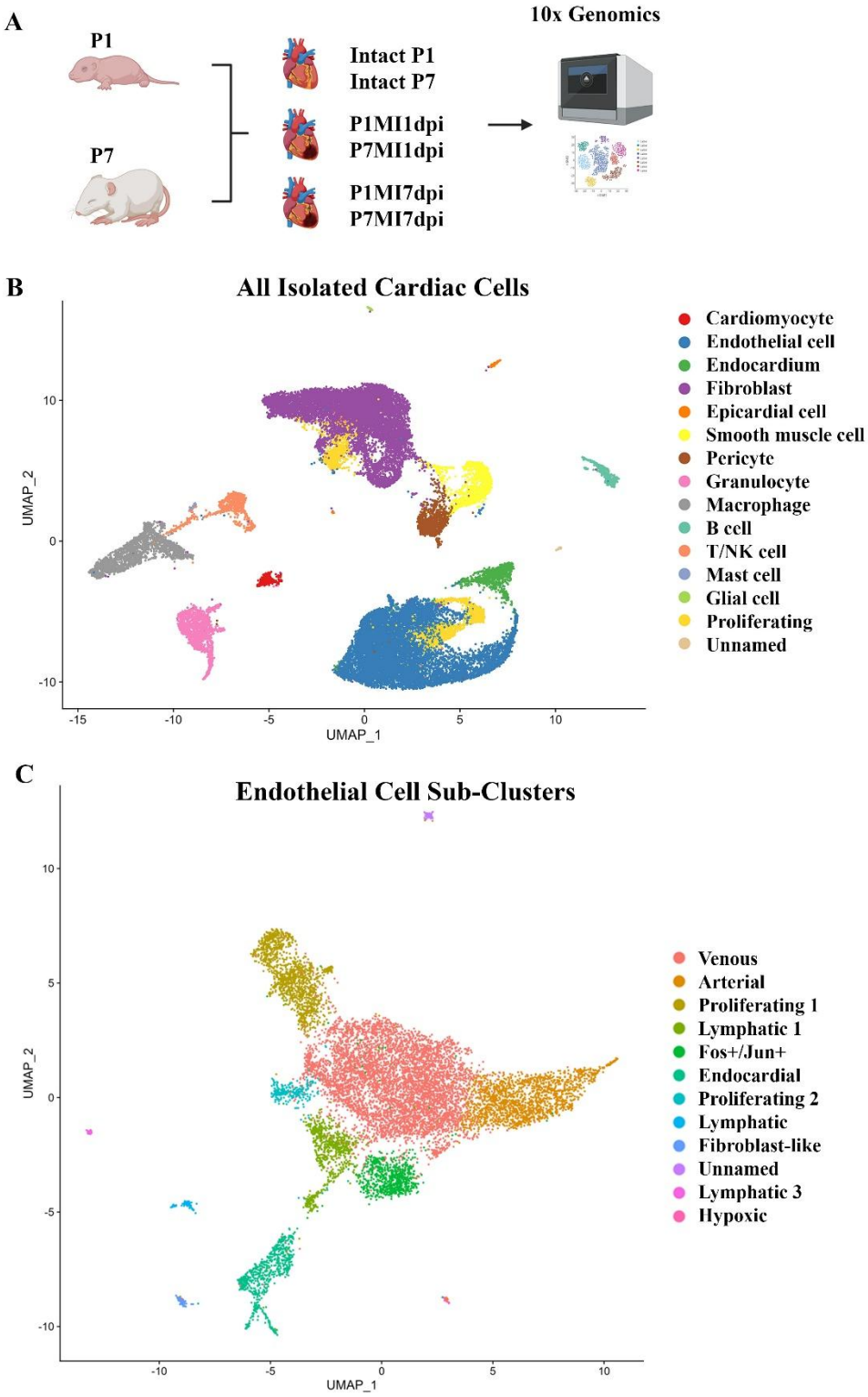

Figure 4-7. P1 versus P7 cardiac cell scRNA-seq data.

Schematic of the experimental pipeline illustrating stages sequenced. CD1 mice underwent MI at P1 or P7. Hearts were harvested at 1dpi (P1MI1dpi and P7MI1dpi) or 7dpi (P1MI7dpi and P7MI7dpi). For the intact conditions, the samples were collected at either P1 or P7 without any prior surgery. The samples were FACS-isolated using the 7AAD marker to isolate the live cells and libraries were prepared for sequencing using the 10x Genomics platform[101] (A). UMAP showing clustering of distinct cell types from whole hearts pooled across all samples and timepoints (B). Subclustering of the endothelial cell cluster revealed a breadth of cell identity and allowed identification of a lymphatic endothelial cluster (C). n = 3 hearts were pooled to a single sequencing library per condition. Panel A created with BioRender.com

Unbiased differential gene expression analysis of our LEC cluster (Figure 4-8) revealed distinct molecular signatures between LECs at P1 versus P7, with no enriched pathways in the uninjured state, but enrichment of several pathways and associated genes at P7 relative to P1 following injury (Figure 4-9). Notably, aquaporin-1 is shown to be differentially upregulated in P7, but not P1, in LECs following MI (Figure 4-9). LECs are not widely reported to express AQP1, and this may reflect the possibility that AQP1 expression is upregulated only in an injury/inflammatory context when clearance of tissue fluid becomes necessary. Immunofluorescent staining of neonatal and adult lymphatic vessels for AQP1 with and without injury presents a possible avenue for future work, albeit one beyond the scope of this work which focuses on capacity for cellular trafficking rather than fluid handling.

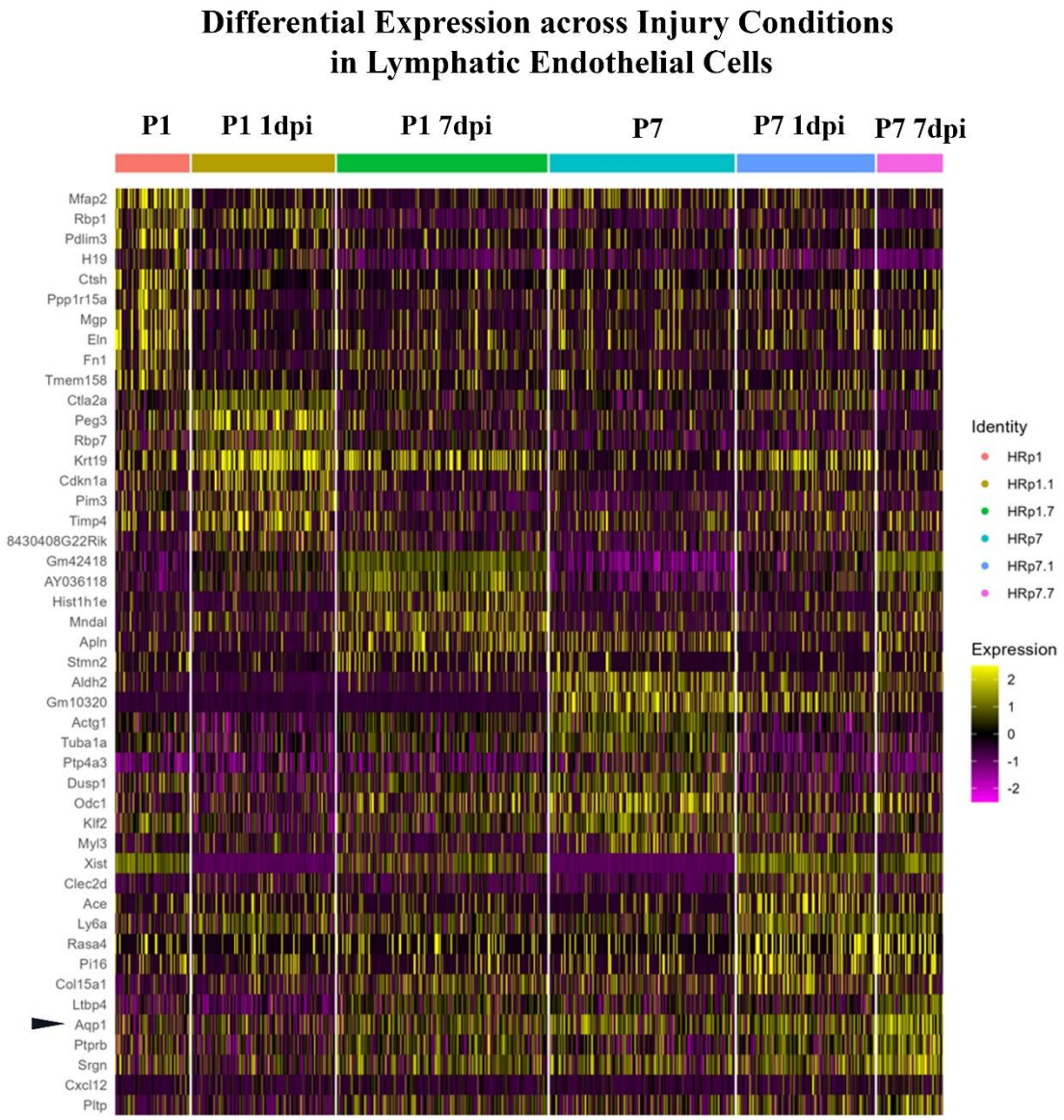

Figure 4-8. Genes differentially expressed by LECs between conditions.Heatmap of changes in lymphatic endothelial cell gene expression across conditions.

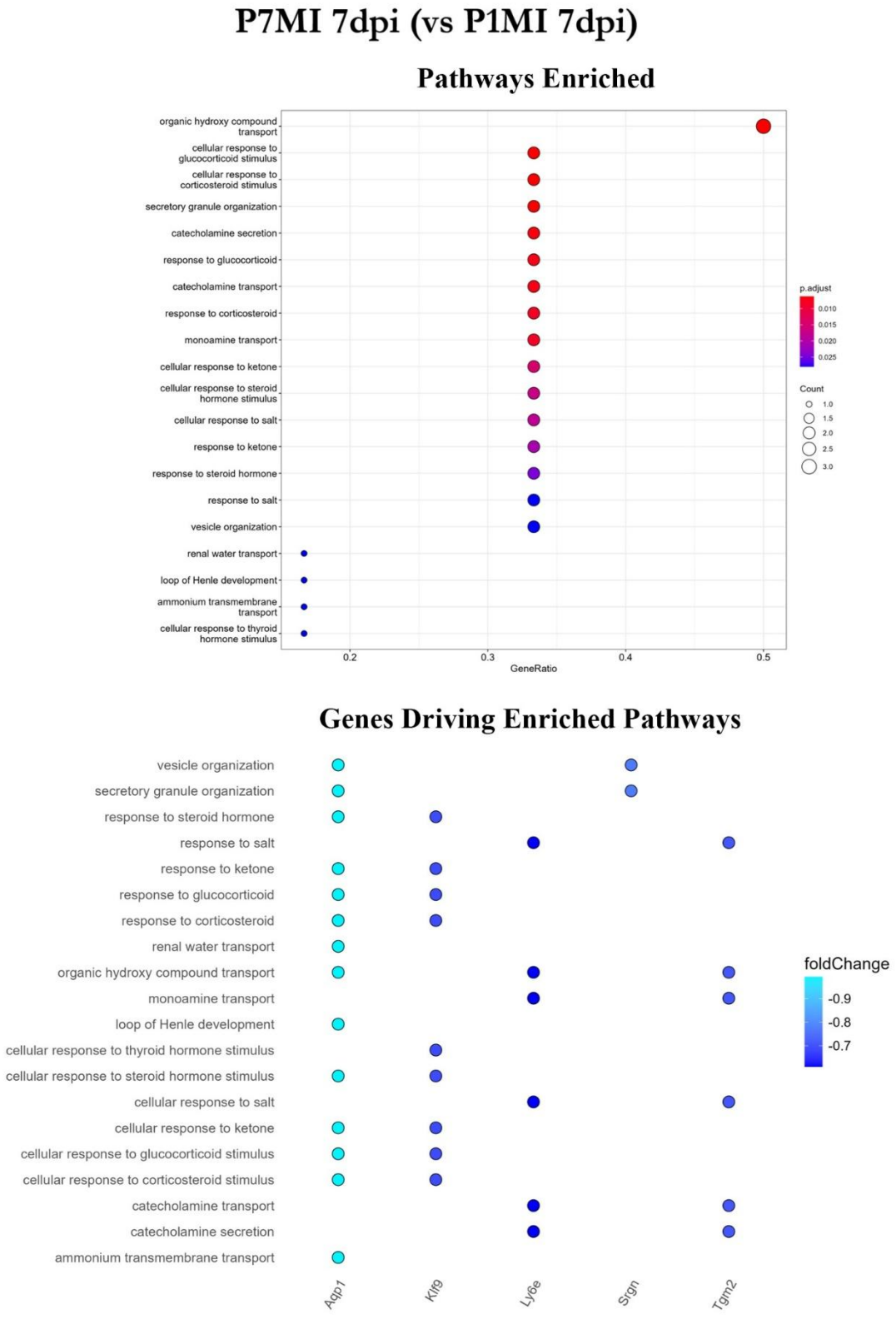

Figure 4-9. GO pathway enrichment in LECs after MI: P1 vs P7.

No enriched pathways were detected at baseline (uninjured P1 vs P7). P7MI7dpi vs P1MI7dpi showed enrichment for vesicle trafficking/secretion and hormone-response pathways in P7, with a prominent aquaporin DEG among the drivers, suggesting a water-transport/fluid-

handling response that emerges in the more mature P7 lymphatics but is not evident in the immature P1 setting.

4.3.3 Macrophages are trafficked following MI at P7 but not P1

Previous adoptive transfer data from our group has demonstrated the capacity of the cardiac lymphatics to clear macrophages from the infarct zone following MI at P7, but not P1[101]. Preliminary work examining the clearance of endogenous *hCD68-GFP* macrophages to the mediastinal lymph nodes (MLNs) was also conducted. To validate this adoptive transfer data, increase the *hCD68-GFP* sample size, and extend the analysis more specifically to tissue-resident macrophages, MLNs were isolated from *hCD68-eGFP* and *CX3CR1-eGFP* injured and control mice, identified on imaging of whole cardiopulmonary blocks by localisation within the subcardinal, subaortic, and paraaortic zones. *CX3CR1-eGFP* has previously been shown to mark tissue-resident macrophages[119]. The cardiopulmonary blocks were sectioned, and images were acquired of MLNs *in situ* for quantification of the $CD68^+$ or $CX3CR1^+$ macrophage numbers in relation to MLN size (Figure 4-10; Figure 4-11). The presence of both $CD68^+$ and $CX3CR1^+$ macrophages in MLNs 7 days after MI at P1 was not significantly different compared to intact P8 hearts (Figure 4-11), whereas $CD68^+$ and $CX3CR1^+$ macrophage numbers were significantly elevated after MI at P7 (20.1%, 10.6%) compared to P14 intact hearts (6.4%, 2.8%; $p<0.05$; Figure 4-11).

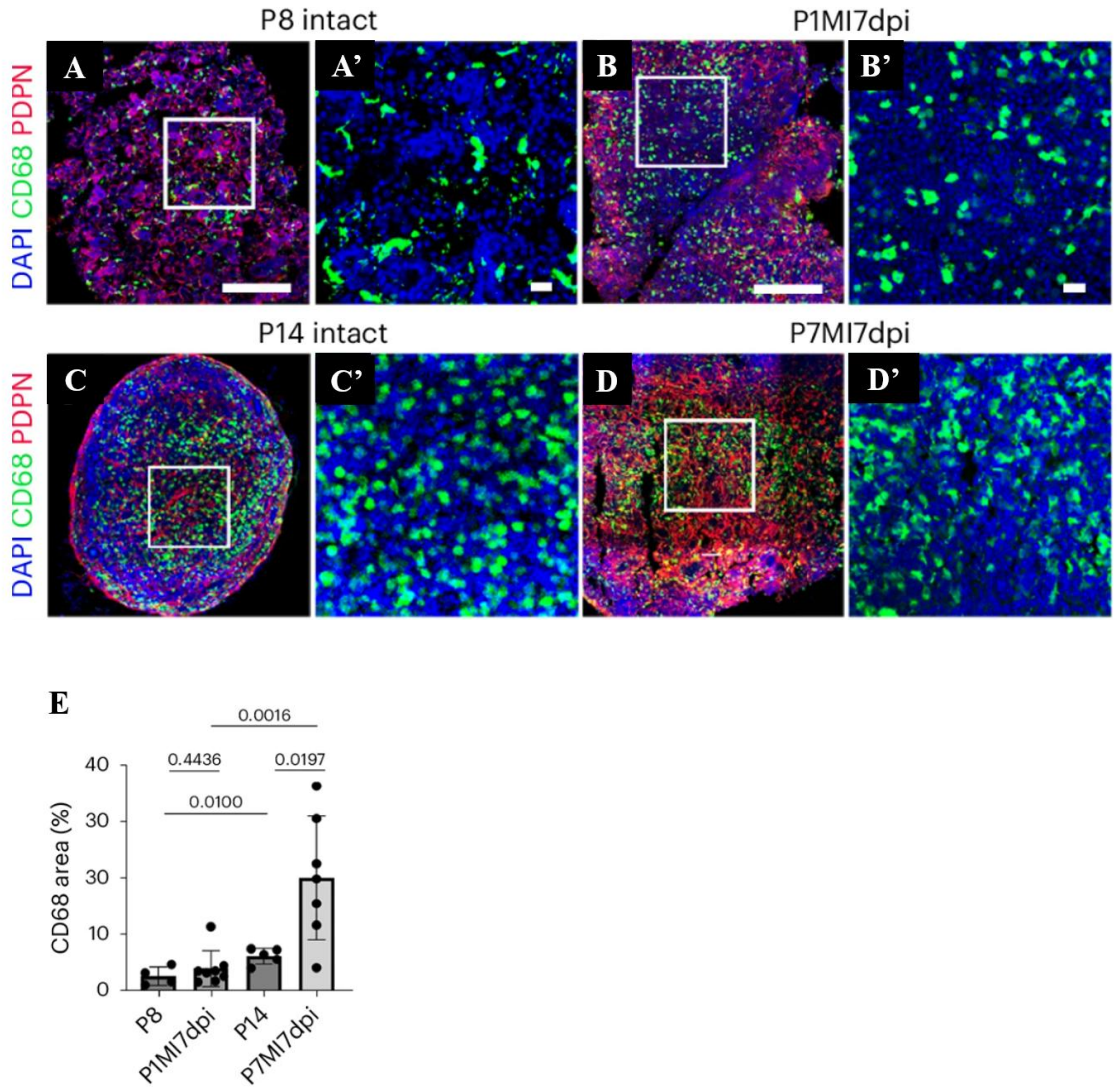

Figure 4-10. Visualisation of *hCD68–eGFP* GFP$^+$ macrophages in MLNs post-MI.

MLN visualisation confirmed minimal clearance at P1 after MI, which appeared increased at P7, compared to the respective intact controls that contained resident MLN GFP$^+$ macrophages (compare A to B and compare C to D). Quantification of macrophage numbers in the MLNs validated these observations and indicated that the difference in clearance at P1 versus P7 was significant (E). Quantification was conducted across the entire MLN area within 10 µm sections. Magnification boxes are illustrative. Data are presented as mean ± SEM. n = 4 for P8, n = 8 for P1MI7dpi, n = 5 for P14 and n = 7 for P7MI7dpi. Significant differences were calculated using one-way ANOVA followed by Tukey's multiple comparisons test. Scale bars: 0.5 mm for A-D, 20 µm for A'-D'.

To exclude the possibility that the increased CD68$^+$ and CX3CR1$^+$ macrophage numbers found in the MLNs after MI at P7 was due to a proliferative response of lymph node-resident macrophages, MLNs were stained with the proliferation marker phospho-histone

H3 (PH3; Figure 4-11). GFP^+ cells were found to proliferate in the subcapsular sinus of MLNs from both intact (P14) and P7 infarcted mice after 7-days (Figure 4-11). However, there was no significant difference between proportion of proliferative cells in any condition (Figure 4-11).

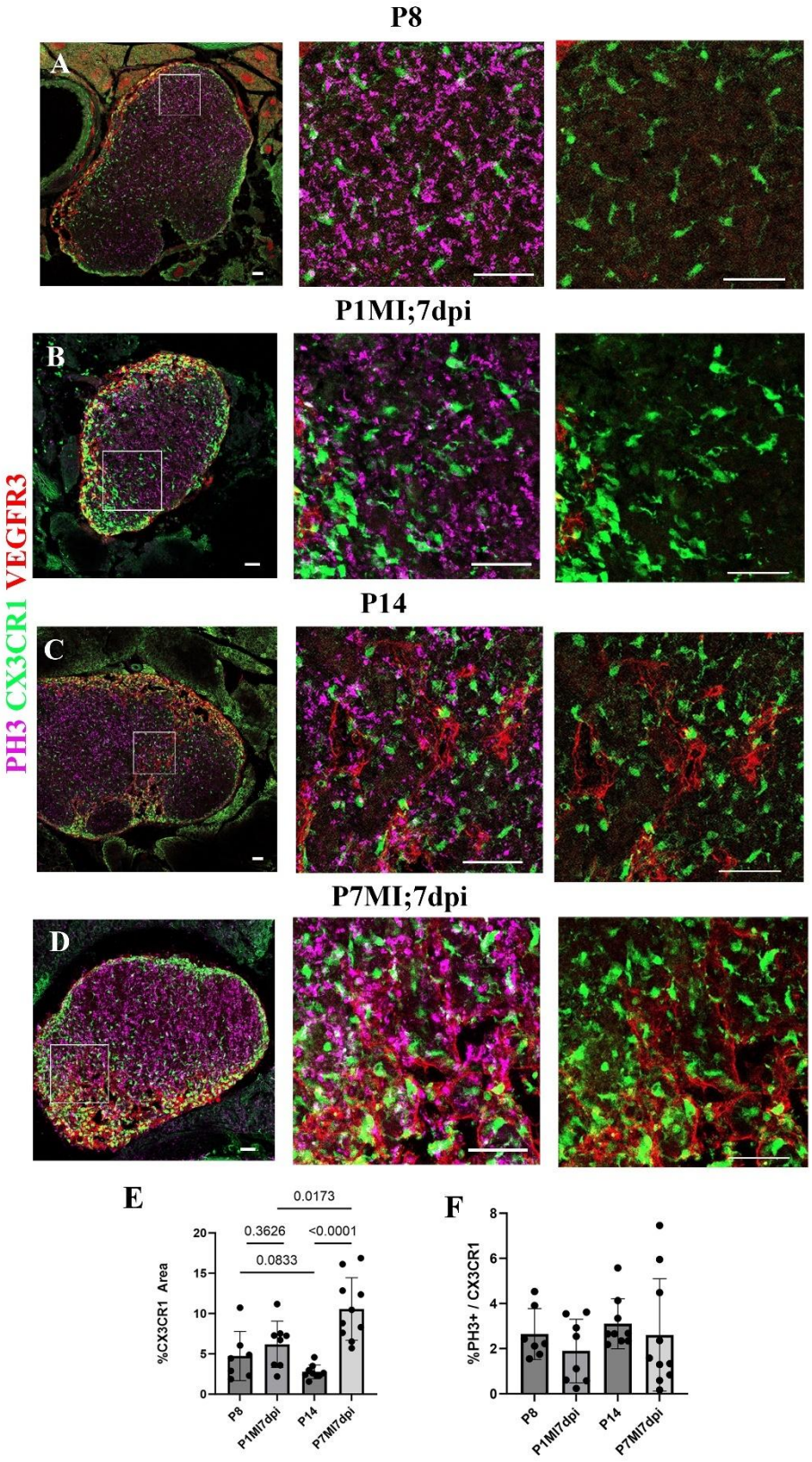

Figure 4-11. Macrophage drainage to mediastinal lymph nodes.

Visualisation of endogenous GFP$^+$ macrophages in MLNs from *Cx3cr1-eGFP* mice confirmed minimal clearance at P1 post-MI, which appeared increased at P7, compared to the respective intact controls which contained resident MLN GFP$^+$ macrophages (compare A and C, compare

B and D). Quantification of macrophage numbers in the MLNs validated these observations and indicated the difference in clearance at P1 versus P7 was significant (E). There was no significant difference in $PH3^{+}$ macrophages between conditions (F). Quantification was conducted across the entire MLN area within 10 μm sections. Magnification boxes are illustrative. Data are presented as mean ± SEM. n = 7 for P8, n = 8 for P1MI7dpi, n = 9 for P14 and n = 10 for P7MI7dpi. Significant differences were calculated using one-way ANOVA followed by Tukey's multiple comparisons test. Scale bars: 50 μm.

The boxed sections provided show magnified views of the region containing afferent lymphatics, the area where cleared macrophages are expected to enter MLNs and are unrelated to the quantitative assessment of macrophage numbers. Quantification was carried out across the entirety of each lymph node and took place in an unbiased manner, blinded to condition. A single z-stacked image was taken through each individual lymph node cryo-sectioned at 10 μm intervals. Technical conditions including the staining protocol and microscope laser power were consistent between samples. No post-imaging intensity alterations were carried out prior to analysis. Staining for F4/80 in *Cx3cr1-GFP* MLNs confirmed co-localisation of GFP with F4/80, validating the identify of these cells as macrophages (Figure 4-12).

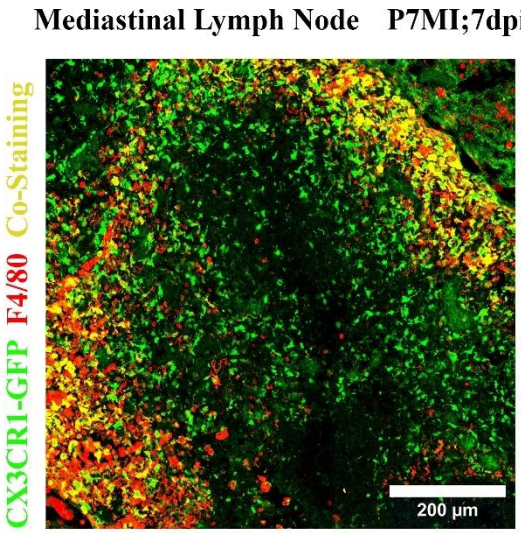

Figure 4-12. CX3CR1-GFP F4/80 co-staining.

GFP^+ cells in CX3CR1-GFP MLNs are confirmed to be macrophages by F4/80 staining. They are densely clustered around the afferent lymphatics. GFP^+F4/80- cells are likely dendritic cells within the lymph node paracortex. Scale bar: 200 µm.

Further staining for F4/80 in MLNs post-MI facilitated delineation of macrophages from dendritic cells, and confirmed the increased presence of macrophages within the afferent lymphatics, draining to the MLNs, at 7 days following MI at P7, but not at P1 (Figure 4-13).

In order to validate that the increase in macrophages within the afferent lymphatics following MI at P7 is due to trafficking from the heart, I aimed to disrupt lymphatic drainage and assess any difference in their presence within the lumen of the afferent lymphatics. It is important to note that VEGFC/VEGFR3 disruption would also affect the coronary vasculature and lymphangiogenesis resulting in additional defects and confound any interpretation related to trafficking. Instead, I have utilised *Lyve1* loss-of-function as more specific to lymphatic trafficking and carried out MLN imaging in *Lyve1* knockout mice 7-days after MI at P7, when macrophages are known to accumulate in the wildtype

setting. These images reveal disrupted lymphatic trafficking and a clear absence of macrophages within the afferent lymphatic lumen of P7 *Lyve1*$^{-/-}$ MLNs at 7-days post-MI compared to wildtype controls (Figure 4-13).

Taken together, these data reveal that cardiac lymphatics significantly clear CD68^{+}, CX3CR1^{+} and F4/80^{+} macrophages via the afferent lymphatics to the draining MLNs following MI at P7, but do not clear macrophages from infarcted P1 hearts.

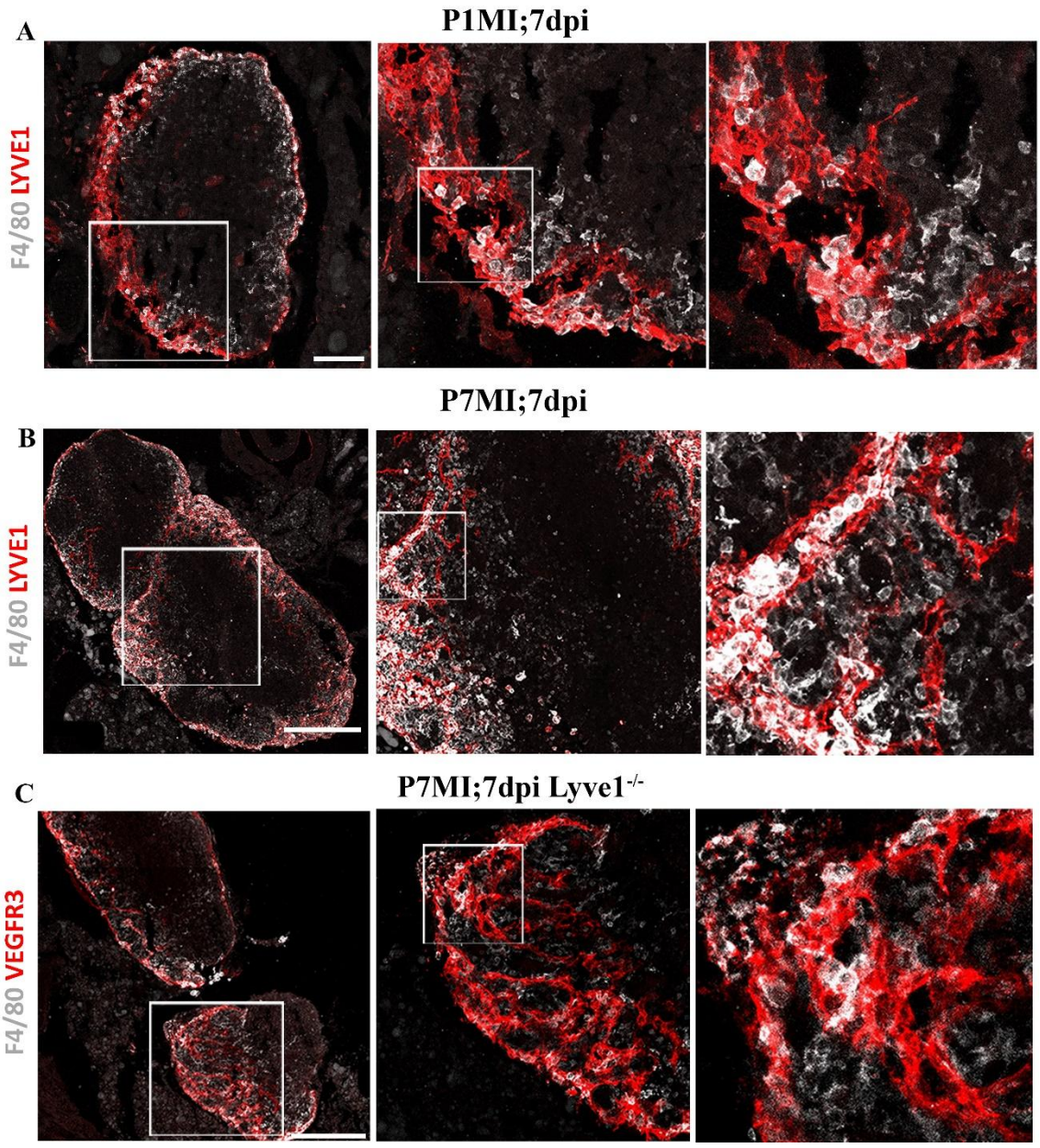

Figure 4-13. F4/80 macrophage within mediastinal lymph node afferent lymphatics.Further F4/80 staining was conducted which confirmed the presence of F4/80^{+} cells within the lumen of MLN afferent lymphatics following MI at P7, but not P1 (Compare A and B). Macrophage drainage is disrupted following P7 MI in the *Lyve1*$^{-/-}$ setting (C). Scale bar 250 μm.

4.3.4 LEC and macrophage molecular pathways at P1 versus P7

Previous analysis of the present scRNA-seq dataset within the group examined ligand-receptor interactions between macrophage and lymphatic subclusters. This original analysis was conducted using a different clustering technique and scTalk analysis,

identifying a number of putative interactions between LECs and macrophages (Figure 4-14). Intriguingly only a single interaction from LECs to macrophages was identified (Figure 4-14A), while multiple interactions were found from macrophages to LECs (Figure 4-14B). The lone ligand-receptor interaction from LECs to macrophages was between the extracellular signalling protein Reelin (Reln) produced by LECs, and Integrin Beta-1 (Itgb1 / CD29), its potential receptor which has not previously been described in these cell populations. Interestingly, published work already implicates Reelin as a pro-regenerative mediator in the context of neonatal heart regeneration[137].

Subsequent qPCR analyses suggested that *Reln* was downregulated at P7 compared to P1, while *Itgb1* expression was unchanged (Figure 4-14). I confirmed the qPCR data at the level of protein expression by immunostaining for REELIN combined with LYVE-1, ITGB1 and IBA1. Here I examined LECs at 5-days post-MI following surgery at P2, to be consistent with the stages examined in the prior study[137], compared to 5-days post-MI at P7 and uninjured controls. This revealed positive staining of ITGB1 in $IBA1^+$ macrophages (Figure 4-14H) and elevated expression of REELIN in LECs at P2 compared to P7 at 5-days post-MI (Figure 4-14), consistent with a role in the early postnatal regenerative response and validating the scRNA-seq pathway analyses (Figure 4-14A).

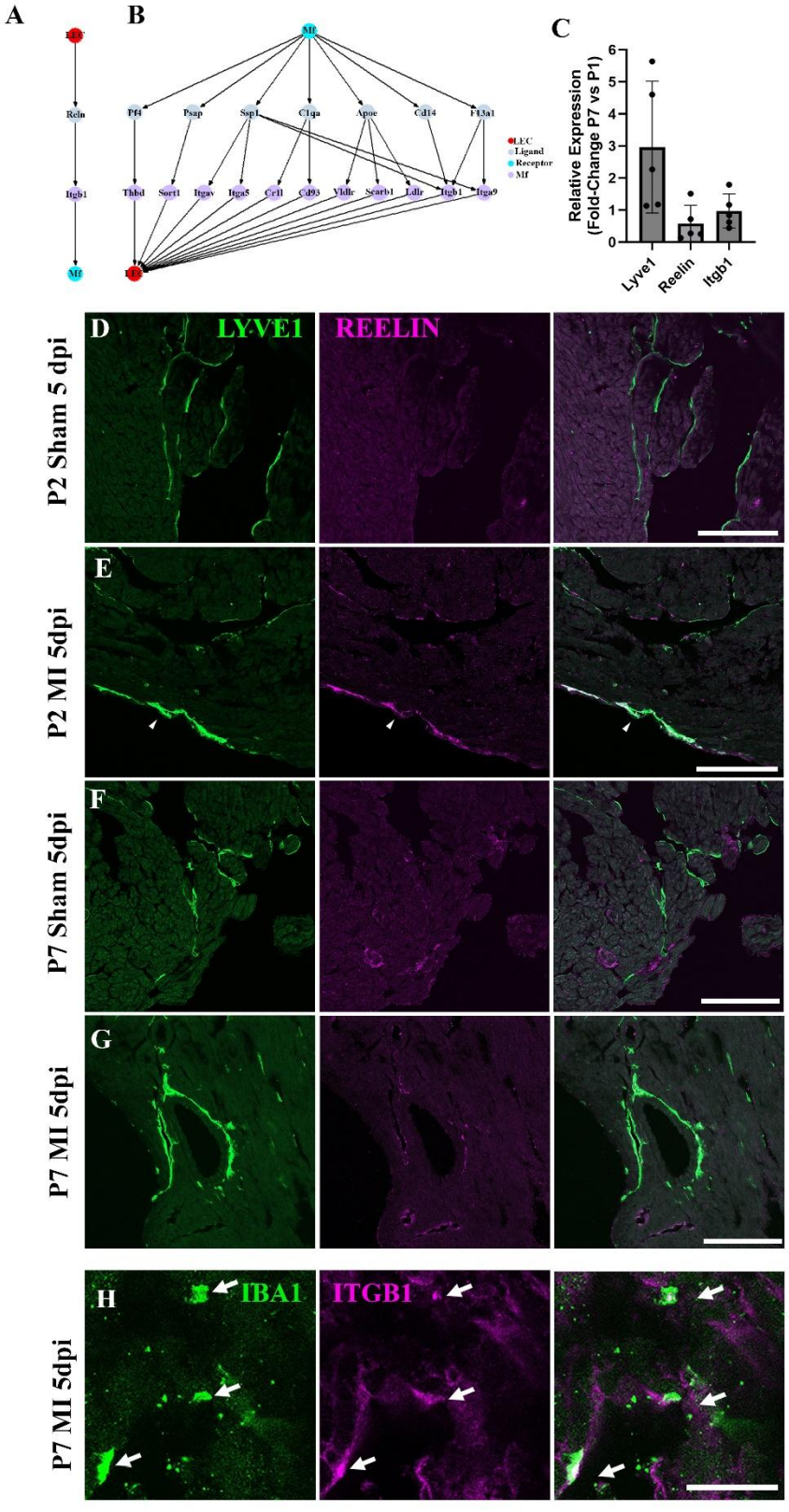

Figure 4-14. Lymphatic-macrophage crosstalk.Tree plot showing outgoing connections from the LECs to Mf (A) and from Mf to LECs (B). The single outgoing LEC signal was identified as Reelin (Reln), a previously described lymphangiocrine factor, interacting with ITGβ1 on Mf (A). Top node refers to source population, second layer to ligands, third layer to receptors and bottom node representing the target population (A, B). A, B adapted from K. Klaourakis[101]. *Reln*

expression was shown by qPCR to decrease between P1 (n = 6) and P7 (n = 5), while *Itgb1* expression was unchanged (C). Immunostaining for REELIN combined with LYVE-1 (D-G) and ITGFB1 combined with IBA1 (H) in resident macrophages and LECs, respectively, revealed elevated expression of Reelin at P2MI5dpi compared to P7MI5dpi and sham controls across equivalent timepoints (D-G). Data are presented as mean ± SD. Qualitative observations in D-H were seen across tissue sections and in 1 additional heart. Scale bar: 150 µm for D-G; 25 µm for H.

4.3.5 Global *Lyve1* knockout impairs cardiac regeneration

Previous MRI studies within the group revealed an unexpected association between *Lyve1* and functional outcome following MI at P1 (Figure 4-15), a timepoint normally associated with complete regeneration and preserved function[15]. This confounded our initial hypothesis that given pro-regenerative macrophage clearance is not occurring at P1, disruption of clearance by loss of LYVE-1 would have no effect on recovery from early postnatal MI.

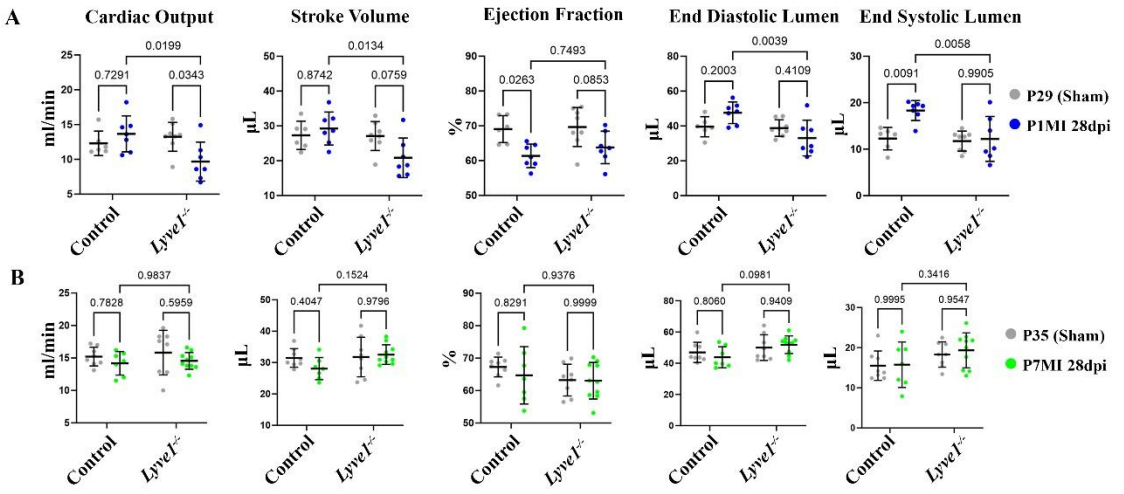

Figure 4-15. Cardiac cine MRI data from K. Klaourakis and C. Carr[101].Plots from longitudinal cine MRI performed on *Lyve1*$^{+/-}$ and *Lyve1*$^{-/-}$ mice 28 days after MI at P1 and P7, as well as in intact control littermates at comparable P29 and P35 stages (A, B). MRI revealed significantly reduced cardiac output (CO) in P1 *Lyve1*$^{-/-}$ mice at 28 days post-MI compared to P29 intact *Lyve1*$^{-/-}$ controls (A). The reduced CO was even more significant than reductions observed for *Lyve1*$^{-/-}$ mice injured at P7 at 28-days post-MI compared to P35 intact *Lyve1*$^{-/-}$ controls (B). Data are presented as mean ± SD. n = 6 for P29 control, n = 7 for P1MI28dpi control, n = 8 for P29 *Lyve1*$^{-/-}$, n = 7 for P1MI28dpi *Lyve1*$^{-/-}$, n = 8 for P35 control, n = 7 for P7MI28dpi control, n = 8 for P35

Lyve1$^{-/-}$, n = 10 for P7MI28dpi *Lyve1*$^{-/-}$. Significant differences were calculated using two-way ANOVA.

A commonly utilised indicator of cardiac regeneration is reduction in scar area. For this reason, picrosirius red (PSR) staining was used to identify the fibrotic area for quantification. Existing samples derived from *Lyve1*$^{-/-}$ P1MI 28dpi hearts were used to optimise the PSR staining protocol and verified by overlap with Masson's Trichrome (MTC; Figure 4-16). There was no significant difference in scar area between wildtype and *Lyve1*$^{-/-}$ hearts (Figure 4-16C), indicating the functional impairment is likely independent of an effect on capacity for clearing fibrosis. This supported MRI-derived estimation of infarct size (Figure 4-16D).

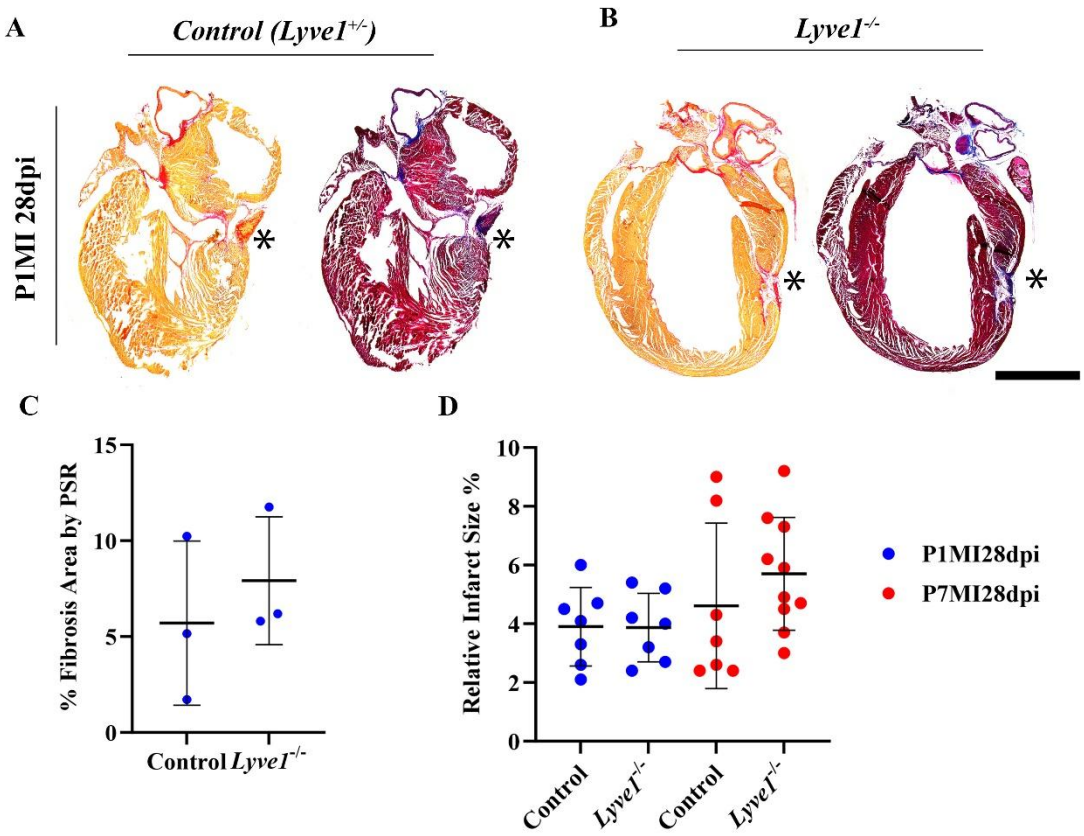

Figure 4-16. Picrosirius red staining of neonatal *Lyve1*$^{-/-}$ hearts post-MI.Sections were taken 28 days following MI at P1 from control (*Lyve1*$^{+/-}$) hearts (A) and *Lyve1*$^{-/-}$ hearts (B) and stained

with picrosirius red (purple gross appearance). Adjacent representative sections were also stained with Masson's Trichrome (yellow gross appearance) to confirm targeting of fibrosis. There was no significant difference observed in scar area as determined by picrosirius red staining (C) or by cardiac cine MRI measurements (D).

Functional impairment in the context of *Lyve1*$^{-/-}$ P1 MI, even in the absence of quantifiable differences in scar area, strongly implies an additional role for LYVE-1 in facilitating cardiac regeneration, supplementary to its role in facilitating lymphatic transmigration of immune cells.

4.3.6 LYVE-1 is also expressed on macrophages, potentially accounting for worsened outcomes in the global knockout

To investigate the possibility of additional roles for LYVE-1 in the context of neonatal heart regeneration, I considered the expression pattern of LYVE-1 in the heart at this timepoint. In addition to its expression on LECs, LYVE-1 is also expressed on tissue-resident macrophages (Figure 4-17). It is well established that the tissue-resident macrophage population is essential for neonatal cardiac regeneration, I therefore hypothesised that global knockout of *Lyve1* may be impacting regenerative function in this macrophage population. This is discussed in Results II.

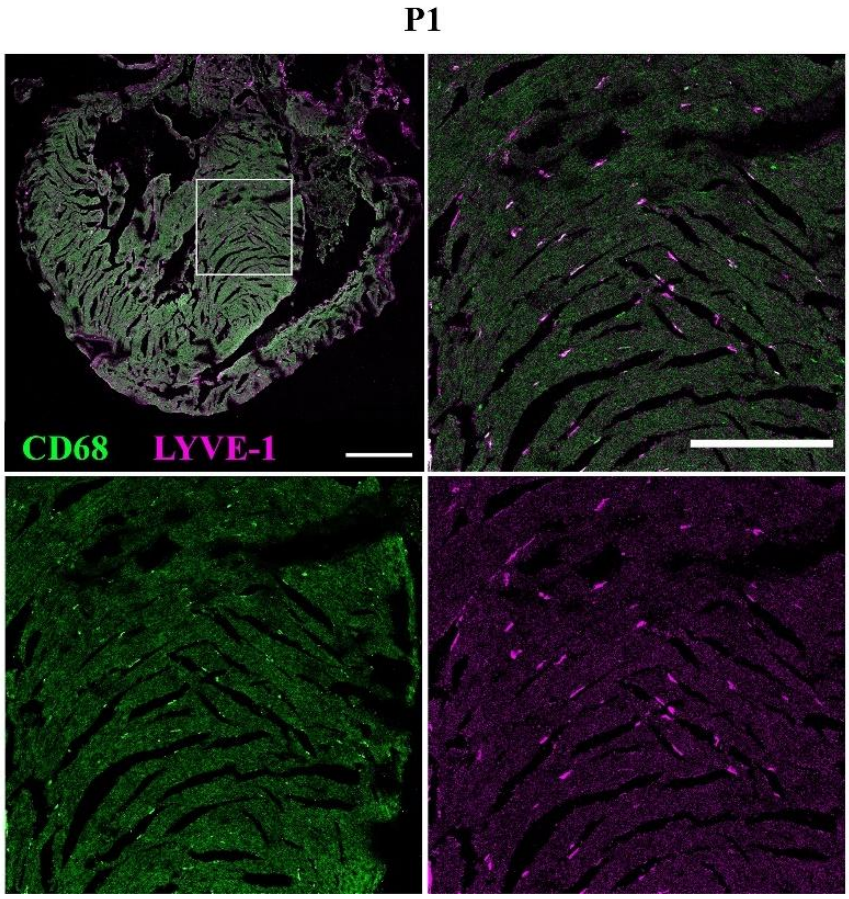

Figure 4-17. LYVE-1$^+$ macrophages are present in the P1 heart.LYVE-1$^+$ tissue-resident macrophages are present throughout the myocardium in the uninjured P1 heart, as indicated by co-staining of CD68 and LYVE-1. Scale bars: 0.5 mm in whole view panel and 250 μm in magnified panels.

4.4 Discussion

This chapter extends previous work from the group to demonstrate macrophages are not effectively cleared by the cardiac lymphatics to MLNs following MI at P1, in contrast to detectable macrophage trafficking at P7. This is attributable to morphological, functional, and transcriptional immaturity of the lymphatics.

4.4.1 Neonatal cardiac lymphatics are not well understood

Although the cardiac lymphatics have received considerable attention to-date, studies have largely focused on their developmental origins and the adult lymphangiogenic response to heart injury across model organisms[9,80,81,87]. There has been little prior investigation of the function of the cardiac lymphatics during neonatal heart regeneration and the transition to fibrotic repair within the first week of life.

The lymphatics of the heart have been described to emerge and grow not only through sprouting of pre-existing vessels (lymphangiogenesis), but also – as reported for zebrafish and mice – from isolated LECs (lymphvasculogenesis), and from a variety of sources including haemogenic endothelium, second heart field progenitors, and paraxial mesoderm[138]. Previous observation in the group of short, isolated lymphatic vessels present mainly on the dorsal surface during early postnatal stages, suggests a further undefined non-venous source[87,89,139].

4.4.2 Adult cardiac lymphatics clear macrophages to improve outcomes

In adult mammals, the lymphatic vasculature is compromised near the site of injury (infarct region), resulting in increased oedema and reduced ability to clear immune cells. Although lymphatics grow and sprout through lymphangiogenesis after MI in adult mice, this endogenous response is insufficient to optimise repair and preserve cardiac function[80,81]. Several gain-of-function studies have used the ligand VEGFC to enhance lymphangiogenesis after MI in adult mice and have reported improved clearance of interstitial fluids and immune cells, most notably macrophages, consequently improving pathological remodelling of the heart and function[9,69,80,81]. Interestingly, a previous study reported that blocking endogenous lymphangiogenesis, through VEGFR3 or VEGFC/D

loss-of-function, does not lead to increased oedema or impaired cardiac function after MI[140]. However, this loss-of-function study targeted endogenous lymphangiogenesis, which in-itself is sub-optimal, and did not investigate the effects of gain-of-function to promote enhanced lymphangiogenesis as previously demonstrated[9,69,80,81]. Collectively, these studies support the hypothesis that the endogenous response of cardiac lymphatics is insufficient to influence outcome post-MI, whereas an augmented lymphatic response, through the administration of exogenous growth factors, improves repair and function.

In contrast to adult mammals (including humans), it is well established that zebrafish[22,141], the surface-dwelling Mexican cavefish[24], neonatal mice, and human infants can regenerate their hearts after injury[17,18,142]. In zebrafish, cryoinjury stimulates cardiac lymphatic growth at the site of injury[87,143] and disruption of VEGFC-VEGFR3 signalling impairs the lymphatic response and associated clearance of infiltrating immune cells, leading to prolonged inflammation, persistent scarring and reduced regeneration[144]. In the presence of an intact lymphatic network, scarring in the adult zebrafish heart is only transient, whereas it is more permanent in the adult mouse heart.

4.4.3 Temporal determination of macrophage subtype and clearance

Functional cardiac lymphatics are required to maintain an optimal immune cell load after adult heart injury, by providing conduits for efficient clearance of immune cells (neutrophils, macrophages, dendritic cells and T cells) to draining MLNs[9]. Macrophages dominate the acute response to MI in terms of sheer numbers derived from infiltrating monocytes which are recruited from bone marrow and splenic reservoirs, with an initial pro-inflammatory ($CCR2^{+}$, $Ly6C^{hi}$) phenotype which then gives rise to pro-reparative ($Ly6C^{lo}$) macrophages *in situ*[145]. The infiltrating monocyte-derived macrophages are

thought to replace a tissue-resident macrophage population (defined as $CCR2^-$, $Ly6C^-$) during the initial acute response to injury. The timing of lymphatic clearance in adult infarcted hearts appears to coincide with the initial pro-inflammatory phase but impacts on downstream repair, suggesting a continuum of monocyte-macrophage function across the acute stages of heart injury[9].

4.4.4 Tissue-resident macrophage retention following P1 MI

In contrast, in neonatal mice after MI, tissue-resident macrophages increase in number without infiltration of monocytes from remote sources[54,70,71] and general depletion of macrophages by clodronate liposome treatment inhibits cardiac regeneration and leads to reduced cardiac function after MI at P1[55]. Thus, we reasoned that pro-regenerative macrophages would not need to be cleared by the cardiac lymphatics following injury at P1; whereas at P7 when macrophages contribute to fibrotic repair there would need to be trafficking, analogous to that in the injured adult heart[9]. This suggestion was strengthened by previous work from the group which demonstrated a significantly reduced lymphatic response 7-days after MI at P1 compared to P7; an observation which was background-dependent. Previous work in the group also demonstrated impaired trafficking at P1 by adoptive transfer of adult splenic hCD68-$eGFP^+$ macrophages into wildtype infarcted neonatal recipient hearts followed by analysis of the recipient MLNs. Here, the adult donor-sourced labelled macrophages were competent for trafficking and clearance, as previously demonstrated[9].

4.4.5 Early postnatal cardiac lymphatics are functionally immature

We validated the capacity of macrophages for trafficking at P7 via MLN imaging in *hCD68-eGFP* mice post-MI and demonstrated this was absent following injury at P1.

Given the macrophage response to neonatal MI comprises a large number of tissue-resident macrophages, I imaged *CX3CR1-eGFP* mouse[118,119] MLNs to confirm $CX3CR1^{+}$ tissue-resident macrophages are also trafficked following injury at P7 but not at P1.

Impaired lymphatic clearance at P1 may be the result of several emergent factors during the postnatal period, including maturation of the lymphatic vessels to a state permissive for macrophage ingress and clearance, differences in signalling between LECs and macrophages, and/or temporal functional requirements for essential candidate facilitators of lymphatic trafficking such as LYVE-1. The LECs that form lymphatic vessels are interconnected by specialised cell-cell junctions, with previous studies describing a transition from impermeable zipper-like to cell permeable button-like junctions during embryonic development as evidenced in the mouse trachea, diaphragm, and lungs[83,95,146]. This transition starts at approximately E17.5 and is completed by P14[96]. We observed a similar process in the early postnatal heart with zipper-like junctions predominating in the initial lymphatic vessels during the first days after birth and button-like junctions appearing during the second week of life. This maturation of the initial lymphatics likely affects their ability to clear immune cells from the heart to lymph nodes at early neonatal (P1) stages. At P7 when clearance was evident from our adoptive transfer experiments, there was still an incidence of zipper-like junctions suggesting an ongoing developmental process through to adulthood when all junctions are button-like and the lymphatic endothelium is relatively cell permeable[9].

Automating this analysis is challenging, as is obtaining images similar to those defining the junctions in the seminal paper that characterised button-/zipper-like junctions for the

first time[83]. This is due to inherent differences in cardiac versus tracheal tissue (for example, the well-known autofluorescence associated with the underlying myocardium of the heart). The present analysis serves to illustrate that the transition between junctions, as previously defined, is also present in the heart rather than to comprehensively characterise the junctions.

I considered manipulation of the button state as a potentially informative experiment to demonstrate an impact on trafficking. However, current methods to manipulate these junctions are largely restricted to disrupting VEGF signalling, for example, activation of VEGFA-VEGFR2 signalling induces conversion of buttons to zippers in lacteals and inducible knockout of VEGFR3 prevents maturation of zippers into buttons[84,98]. There are two potential confounders with disrupting VEGF signalling. Firstly, VEGF signalling (especially VEGFC/VEGFR3) is important in the context of cardiac lymphangiogenesis post-MI[9] and consequently it would be challenging to delineate the effects of altered lymphatic sprouting versus lymphatic permeability. Secondly, these manipulations are relatively well-characterised in terms of morphological effect and permeability to Evans blue (i.e., fluid/macromolecule permeability), but there is little characterisation pertaining to whether these induced junctional alterations are suitable for our purpose of altering immune cell trafficking.

4.4.6 Macrophage-lymphatic endothelial cell crosstalk

To investigate whether temporal alterations in signalling between the LECs and macrophages might influence clearance of the latter, I examined scRNA-seq of P1 versus P7 infarcted hearts at days 1, 4, and 7 post-injury in collaboration with Dr M. Weinberger. Prior work identified multiple signals from macrophages to LECs, while the reciprocal

signalling was remarkably restricted to only a single pathway that was elevated at P1 versus P7 following injury. I observed that the extracellular matrix glycoprotein protein reelin (RELN) was expressed in LECs at high levels at P1 compared to P7 and prior pathway analyses identified a potential interaction with integrin β1 (ITGB1) on macrophages, a receptor already hypothesised to be required for RELN signalling[137]. In a recent study, RELN was identified as a lymphangiocrine signal important for cardiomyocyte homeostasis and efficient heart repair and function after neonatal mouse MI[137]. Moreover, RELN has been identified in LECs in human foetal hearts, adding potential relevance to human physiology and disease[147]. Neither the target cell type(s) nor relevant receptor(s) were previously identified, and it will be of interest in future studies to functionally assess the RELN-ITGB1 pathway in LECs and macrophages correlated with heart regeneration.

4.4.7 Functional impairment in *Lyve1*$^{-/-}$ P1 hearts post-MI

Finally, we investigated a role for LYVE-1 acting across the P1-P7 regenerative window, given its pivotal role in the hyaluronic acid (HA) mediated adhesion and entry of immune cells to initial lymphatics[103]. We hypothesised that global *Lyve1* gene deletion would have no effect on P1 heart regeneration given that macrophage trafficking is negligible at this stage, consistent with the need to retain the pro-regenerative tissue-resident population *in situ*[55]. Unexpectedly, MRI of *Lyve1* knock-out hearts 28-days after MI at P1, a time point when regeneration would be anticipated to be complete[16], revealed aberrant functional parameters. This prompted a re-evaluation of the role of LYVE-1 beyond the lymphatic endothelium, drawing on its known expression pattern in tissue-resident macrophages[148].

4.4.8 LYVE-1 is also expressed on tissue-resident macrophages

I therefore hypothesised that the regenerative impairment observed following global *Lyve1* knockout in the context of P1 MI was due to a role for LYVE-1 on tissue-resident macrophages and not lymphatics.

4.5 Summary

In summary, neonatal cardiac lymphatics are functionally immature at P1, with zipper-like junctions predominating, limited lymphangiogenesis, and reduced macrophage egress to MLNs. By P7, junctional maturation and network expansion coincide with detectable trafficking. scRNA-seq highlights age-dependent LEC-macrophage signalling (including RELN-ITGB1), and the *Lyve1*$^{-/-}$ phenotype at P1 suggests a role for LYVE-1 on tissue-resident macrophages in regeneration.

5 RESULTS II: TISSUE-RESIDENT MACROPHAGES REQUIRE LYVE-1 TO FACILITATE REGENERATIVE HEALING POST-MI

5.1 Background

Owing to the impaired cardiac function exhibited by neonatal mice with global knockout of *Lyve1*, this chapter will investigate the contribution of tissue-resident macrophage LYVE-1. For this purpose, *hCD68-CreERT2* mice (kindly provided by Professor David Greaves) were crossed with a homozygous *Lyve1* LoxP 'floxed' mouse line (kindly provided by Professor David Jackson), and their offspring used to produce conditional homozygous *Lyve1* deletion (*hCD68-CreERT2;Lyve1*$^{fl/fl}$). This allowed tamoxifen-driven knockout of *Lyve1* in tissue-resident (TR) macrophages, concurrent with MI-inducing surgery in neonatal mice. Subsequent histological and functional assessment of cardiac regeneration was carried out to identify any deficit caused by loss of macrophage *Lyve1*.

5.2 Aims

To establish whether the impaired regenerative response observed post-MI in *Lyve1*$^{-/-}$ neonatal mice is attributable to loss of LYVE-1 on macrophages, rather than lymphatics.

In this chapter, I address the possibility that global *Lyve1* knockout impairs regenerative function of the neonatal mouse heart following myocardial infarction (MI), not by its effect on lymphatic endothelial cells, but by its role in tissue-resident macrophages. To investigate this: (1) I used *hCD68-CreERT2;Lyve1*$^{fl/fl}$ to knock down *Lyve1* in macrophages prior to MI and (2) assessed cardiac function and neovascularisation.

5.3 Results

5.3.1 Characterisation of *hCD68-CreERT2;Lyve1$^{fl/fl}$* construct

The *Lyve1* global knock-out phenotype suggested an additional, unanticipated role for LYVE-1 outside of facilitating transmigration of immune cells into lymphatics, especially given its known expression in tissue-resident macrophages which are essential for regeneration[55] and are retained rather than cleared from injured P1 hearts. Accordingly, I hypothesised that LYVE-1 in resident cardiac macrophages (Figure 4-17) may play an active role in maintaining their pro-regenerative phenotype. To address this possibility, I conditionally deleted *Lyve1* in macrophages by crossing a newly-derived *Lyve1-floxed* line (Jackson, DG, unpublished) with the recently described *hCD68-CreERT2* mouse line that effectively targets resident macrophages across tissues[120].

5.3.1.1 Tamoxifen delivery with neonatal coronary artery ligation

In order to assess the contribution of macrophage LYVE-1 to neonatal cardiac regeneration, *Lyve1* was conditionally deleted in macrophages before MI. This was achieved by intraperitoneal tamoxifen injection of *hCD68-CreERT2;Lyve1$^{fl/fl}$* mice at P1 and MI-inducing surgery at P2, with subsequent analysis at 7dpi and 28dpi (Figure 5-1). The timepoints for tamoxifen injection and MI were spread across two days to minimise the mortality associated with their concurrent performance – tamoxifen injection predisposes to respiratory failure in this context – while remaining within the reported regenerative window of the post-MI neonatal mouse heart[44].

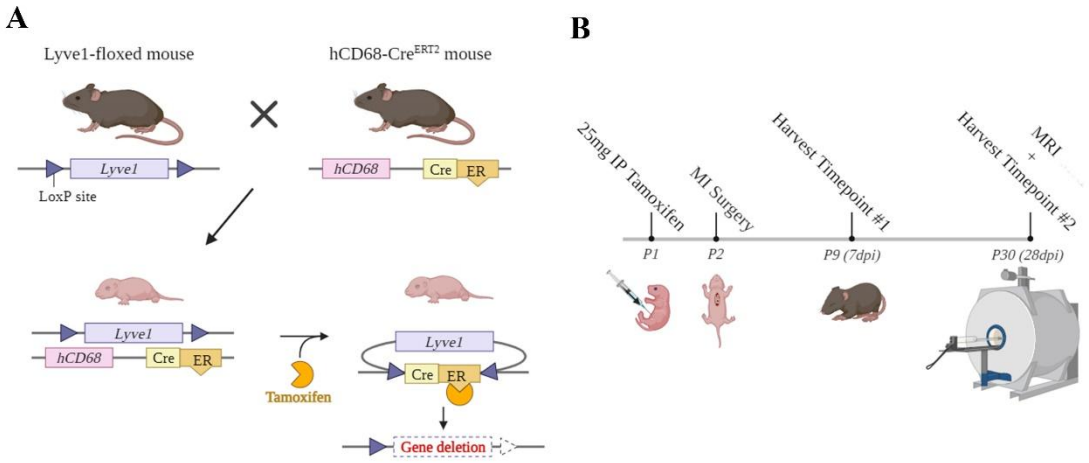

Figure 5-1. Protocol for concurrent tamoxifen administration with neonatal MI.

Mice are injected intraperitoneally at P1 with 0.25 mg tamoxifen and undergo coronary artery ligation surgery at P2. Mice are subsequently culled for analysis at P9 (P2MI;7dpi) or P30 (P2MI;28dpi) following cardiac cine MRI analysis. Panels created using BioRender.com

5.3.1.2 Rosa26^{TdTomato} quantification

The *hCD68-CreERT2* line has been previously characterised in the adult, but not in the neonatal setting. The line was therefore crossed with a *Rosa26^{TdTomato}* reporter line[149] to investigate recombination efficiency and to optimise tamoxifen dose. *hCD68-CreERT2;Rosa26^{TdTomato}* pups were treated with the experimental protocol (Intraperitoneal tamoxifen at P1; MI induced by coronary ligation at P2), before CD68-TdTomato co-expression was assessed at 7dpi**.** Approximate efficiency of recombination was determined by immunofluorescence across whole sections (~45% LYVE1^{+}TdTomato^{+}/LYVE1^{+}; Figure 5-2). TdTomato fluorescence was also confirmed in the absence of immunostaining to confirm positive signal was not due to spectral bleed-through from CD68 or LYVE-1 stains.

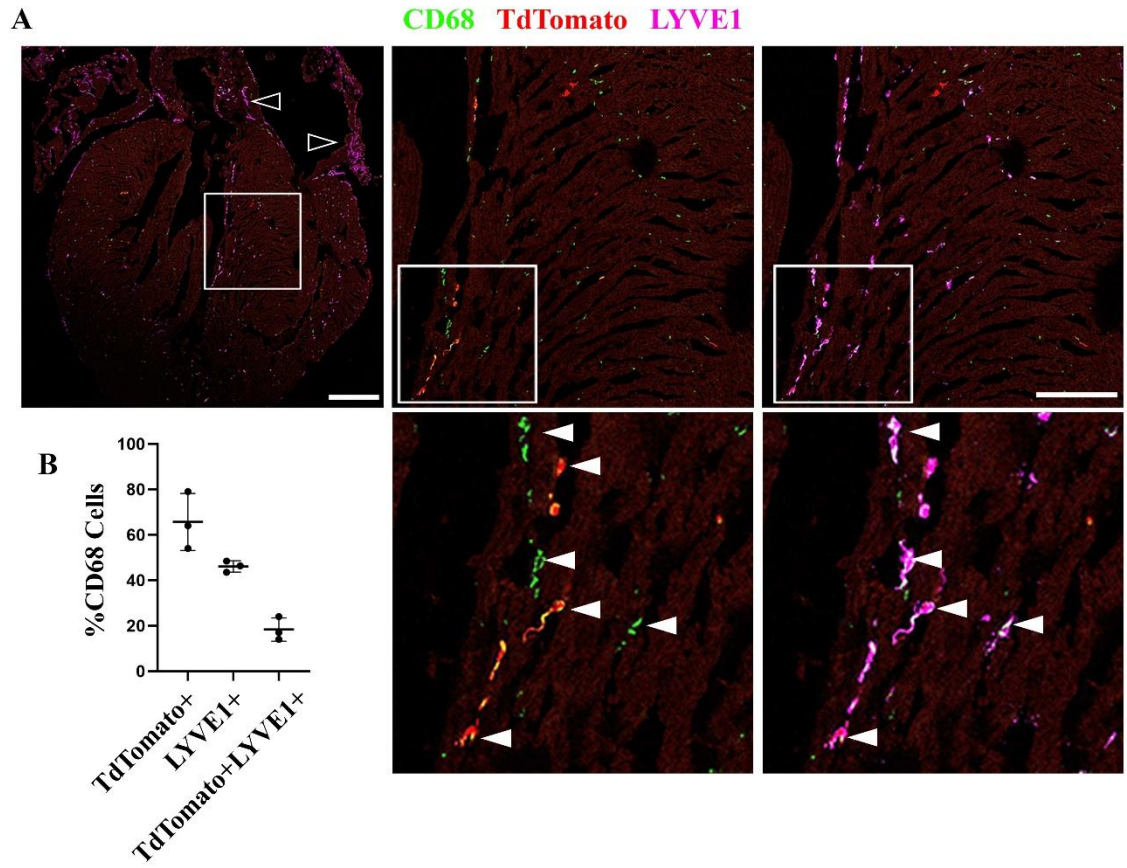

Figure 5-2. Characterisation of *hCD68-CreERT2;TdTomato* line.

Hearts were injected with tamoxifen at P1 before MI at P2 and imaging 7 days post-injury. Sections were co-stained with CD68 and LYVE-1 to determine efficiency and assess for any off-target TdTomato expression. CD68+ macrophages shown with white arrows, lymphatics with black arrows. Quantification of co-staining in sections (B). Tamoxifen injected at P1, MI surgery at P2 to avoid inducing respiratory failure. Data are presented as mean ± SEM. n = 3. Scale bar 350 μm in whole view panel; 150 μm in magnified panel.

5.3.1.3 *Lyve1^{flox}* knockdown quantification

Following validation that the *hCD68-CreERT2* line was effectively targeting LYVE-1^{+} macrophages, and that the tamoxifen dose was sufficient to induce recombination, I crossed the *hCD68-CreERT2* line with the *Lyve1^{flox}* line to produce *hCD68-Cre^{ERT2};Lyve1$^{fl/fl}$* x *Lyve1$^{fl/fl}$* pairings in order to conditionally knock down macrophage *Lyve1*. The litters of these pairings comprised ~50% *Cre^{+}* animals and ~50% *Cre-* littermate controls, all homozygous for the *Lyve1^{flox}*. The extent of knockdown in these animals was first validated by immunofluorescent staining and quantification in paraffin

sections using antibodies against LYVE-1 and the established macrophage marker IBA1 in P2MI7dpi hearts, following tamoxifen injection at P1 and MI at P2 (Figure 5-3). Subsequently, I conducted flow cytometry analysis of hearts at this timepoint (Figure 5-3). Flow cytometry analysis proved technically challenging due to the small number of cells that could be isolated from neonatal mouse hearts, and the inability to pool samples given the unknown genotype associated with our littermate control breeding protocol. Given the evidence already established by immunofluorescent staining, it was deemed contrary to the '3Rs' of animal research (Replacement, reduction, and refinement) to continue this avenue of work. The subsequent observation of a Cre^{+} phenotype validated this decision and is discussed next.

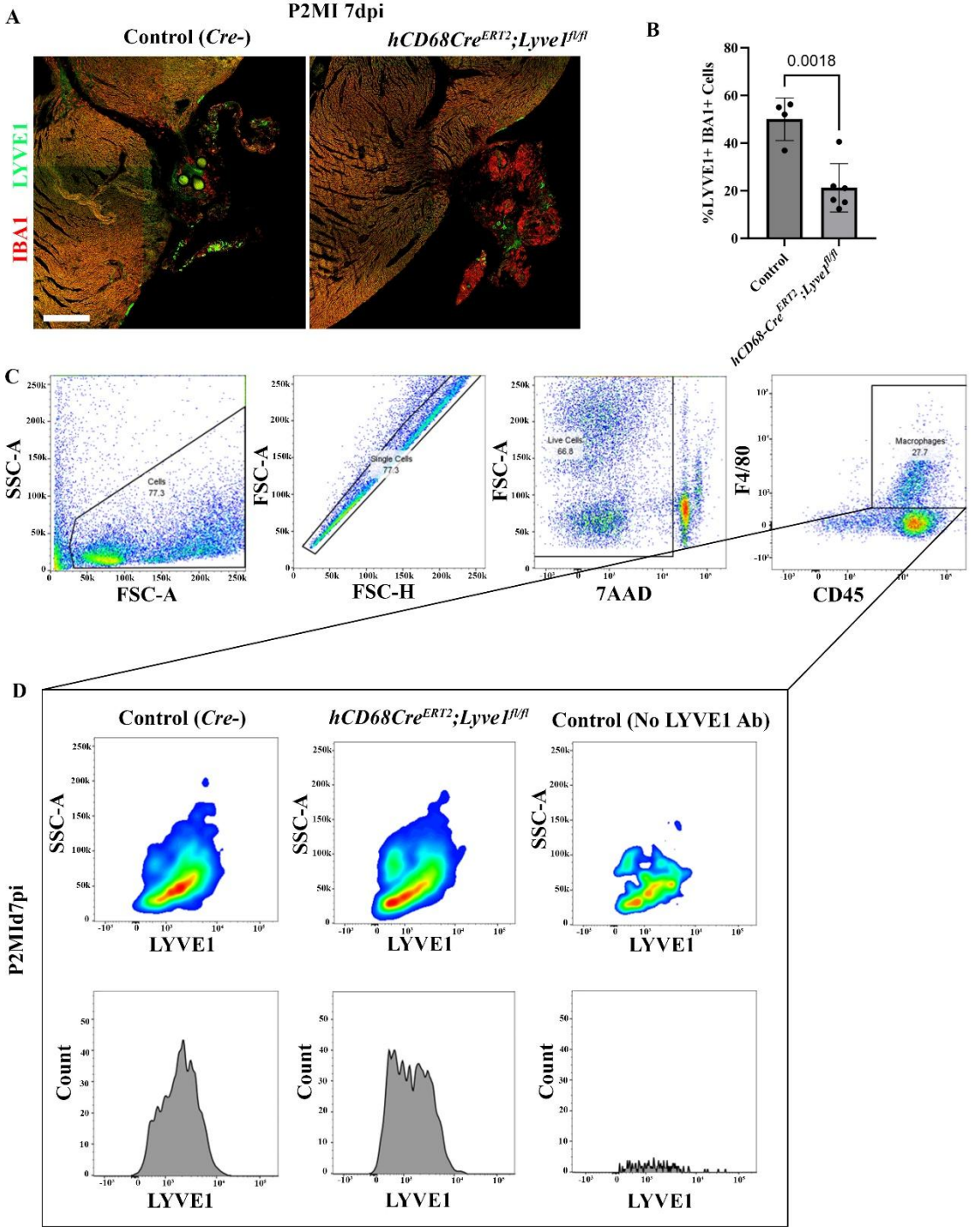

Figure 5-3. Characterisation of *hCD68-CreERT2;Lyve1*$^{fl/fl}$ knockdown.

Hearts were injected with tamoxifen at P1 before MI at P2 and imaging 7 days post-injury. Knockdown was validated by LYVE-1/IBA1 co-staining (A). Proportion of IBA1+ cells also positive for LYVE-1 was quantified and shown to be significantly reduced in *Cre*+ hearts (B). Flow cytometry gating strategy: following tamoxifen administration at P1, P2MI7dpi hearts were dissociated and events gated as follows. Cells by size/complexity, FSC-A vs SSC-A; singlets, FSC-A vs FSC-H; live cells, 7-AAD-; leukocytes, CD45+; and macrophages, CD45+F4/80+ (C). Representative density plots of SSC-A vs LYVE-1 with corresponding LYVE-1 fluorescence histograms for *Cre*- littermate control, *hCD68CreERT2;Lyve1*$^{fl/fl}$, and a

background control processed without anti-LYVE-1 antibody (D). LYVE-1 signal is reduced in *Cre*+ macrophages relative to *Cre*-.

5.3.2 Cardiac cine MRI of P2MI28dpi *hCD68-CreERT2;Lyve1$^{fl/fl}$* mice

I then assessed functional parameters by MRI of macrophage-specific *Lyve1* knock-out animals compared to littermate controls 28 days after MI (Figure 5-1). MRI was conducted in collaboration with Professor Carolyn Carr using the same protocol as previously employed in our global *Lyve1*$^{-/-}$ study (Figure 4-15). Representative images illustrate longitudinal views, used to identify the apex-to-base axis, through which multiple transverse videos were captured at regular intervals (Figure 5-4). This revealed impaired function with significantly reduced CO ($p = 0.0046$) in the *hCD68-CreERT2;Lyve1$^{fl/fl}$* P2 infarcted hearts at day 28 (Figure 5-5). Stroke volume and end diastolic volume (Figure 5-5) were also decreased significantly ($p = 0.0052$ and $p = 0.0352$, respectively), consistent with what we observed in the global *Lyve1* knock-out animals P1MI (Figure 4-15, Figure 5-6).

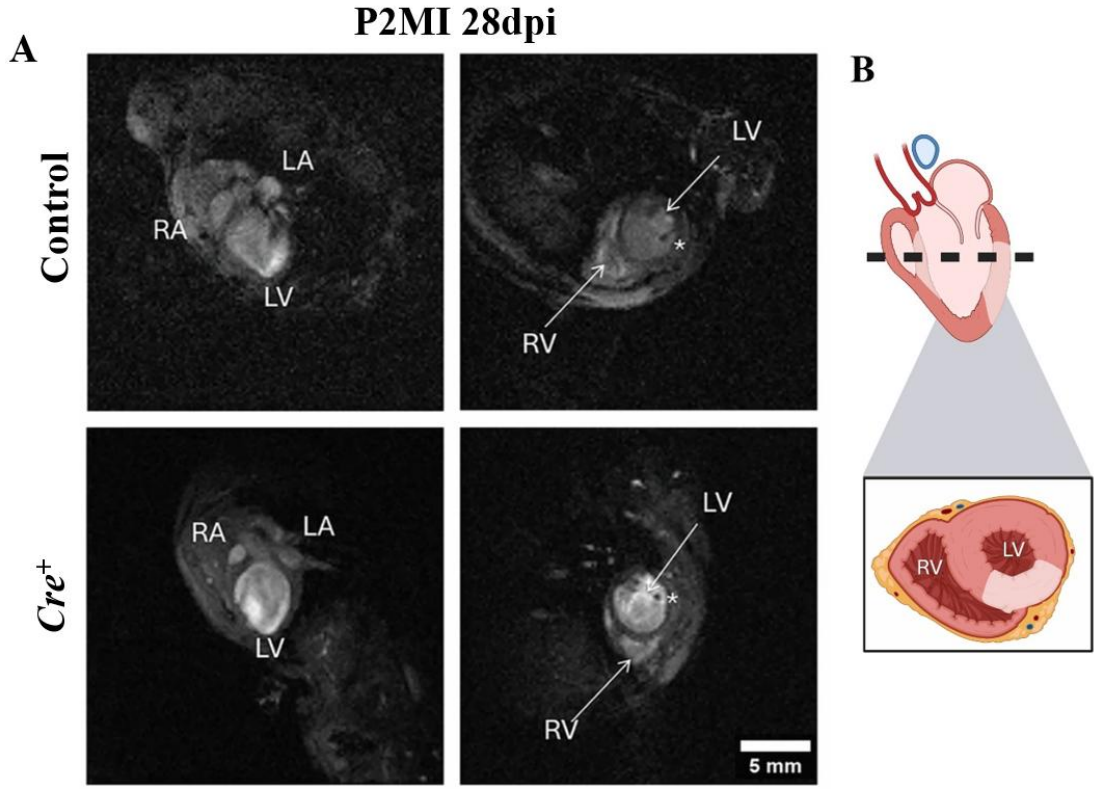

Figure 5-4. Cardiac cine MRI representative images.Transverse and longitudinal cine MRI representative images from control and *hCD68-CreERT2*$^{+}$ animals at P2MI28dpi illustrating infarct location and anatomical landmarks (A). Illustration of transverse and longitudinal views including highlighted infarct zone to aid interpretation of MRI (B). Scale bar 5 mm. Panel B created using BioRender.com

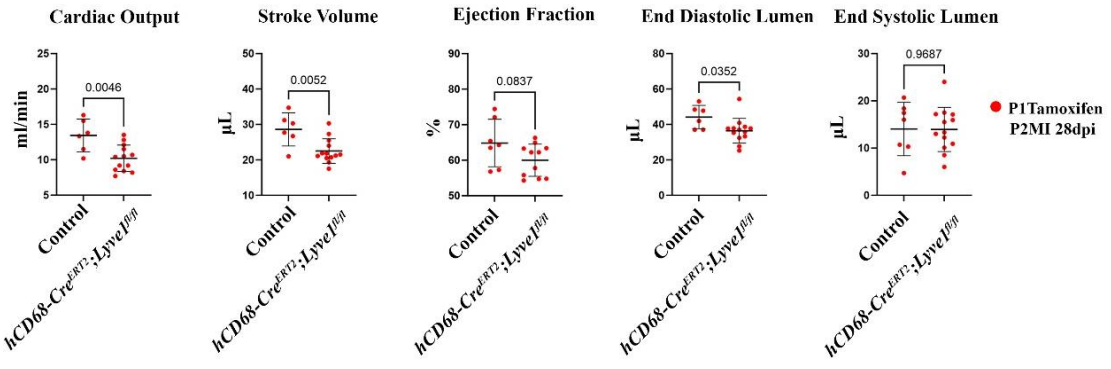

Figure 5-5. Conditional *Lyve1* knockout MRI quantification.

Plots from cine MRI performed on *hCD68-CreERT2;Lyve1*$^{fl/fl}$ mice 28 days after MI at P2 reveal impaired functional recovery across cardiac output, stroke volume, ejection fraction, end diastolic volume consistent with Figure 4-15A, differing only in end systolic volume. Data are presented as mean ± SD. n = 7 for control, n = 13 for *Cre*+. Significant differences were calculated using unpaired two-tailed Student's t-test.

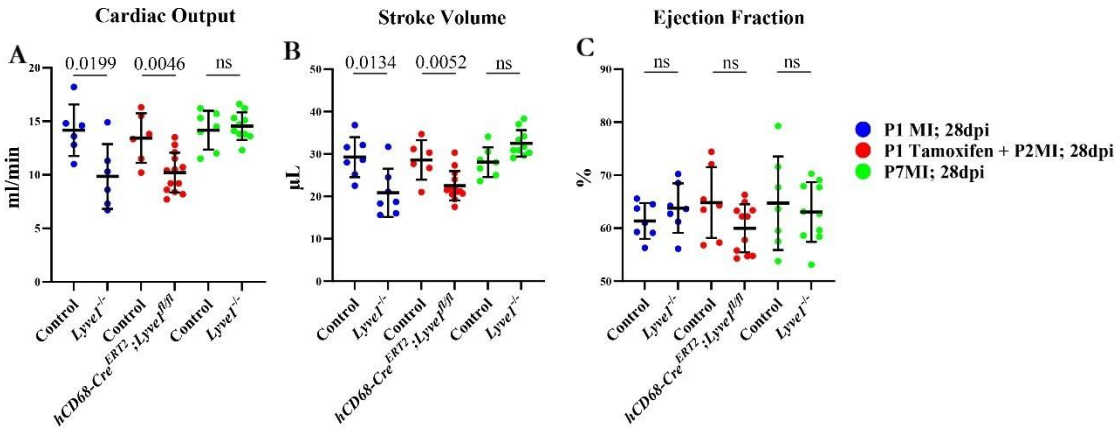

Figure 5-6. MRI-derived cardiac function at 28 days post-MI across conditions.

Adapted from data displayed in Figure 5-5 and Figure 4-16. Comparison of *hCD68-CreERT2;Lyve1-flox* functional readouts 28dpi with previously obtained global *Lyve1*$^{-/-}$ data. *Lyve1* loss reduces cardiac output in the neonatal P1 MI cohort and in the conditional *Cre*+ cohort at 28 dpi, whereas no difference is detected after P7 MI (A). Stroke volume shows the same pattern; reduced in P1 MI and *Cre*+ but not significantly altered after P7 MI (B). Ejection fraction does not differ significantly between genotypes in any cohort at 28 dpi (C). The conditional knockout recapitulates the functional deficit observed in the global knockout. Data are presented as mean ± SD. n = 6 for P29 control, n = 7 for P1MI28dpi control, n = 8 for P29 *Lyve1*$^{-/-}$, n = 7 for P1MI28dpi *Lyve1*$^{-/-}$, n = 8 for P35 control, n = 7 for P7MI28dpi control, n = 8 for P35 *Lyve1*$^{-/-}$, n = 10 for P7MI28dpi *Lyve1*$^{-/-}$, n = 7 for P2MI28dpi *Cre*$^{-}$, n = 13 for P2MI28dpi *Cre*$^{+}$. Significant differences were calculated using two-way ANOVA for P1MI28dpi and P7MI28dpi and unpaired two-tailed Student's t-test for P2MI28dpi.

5.3.3 Histological analysis of *hCD68-CreERT2;Lyve1*$^{fl/fl}$ hearts post-MI

To explore structural correlates of the MRI findings, I assessed scar burden and the neovascular response within the infarct. I first carried out picrosirius red staining, which indicated no significant difference between *hCD68-CreERT2;Lyve1*$^{fl/fl}$ P2 infarcted hearts and littermate controls at either 7- or 28-days post-injury (Figure 5-7, Figure 5-8). Identification of the infarct zone was validated by staining with Wheat Germ Agglutinin (WGA). WGA is a lectin which is an established marker for fibrotic cardiac tissue that binds exposed N-acetyl-D-glucosamine- and sialic-acid–bearing glycoproteins, revealing infarct ECM remodelling in tissue sections[150] (Figure 5-8). Lack of significant difference in infarct size observed between control and *hCD68-CreERT2;Lyve1*$^{fl/fl}$ hearts – even in

the presence of impaired functional recovery – is consistent with the phenotype observed in global *Lyve1*$^{-/-}$ animals (Figure 4-16).

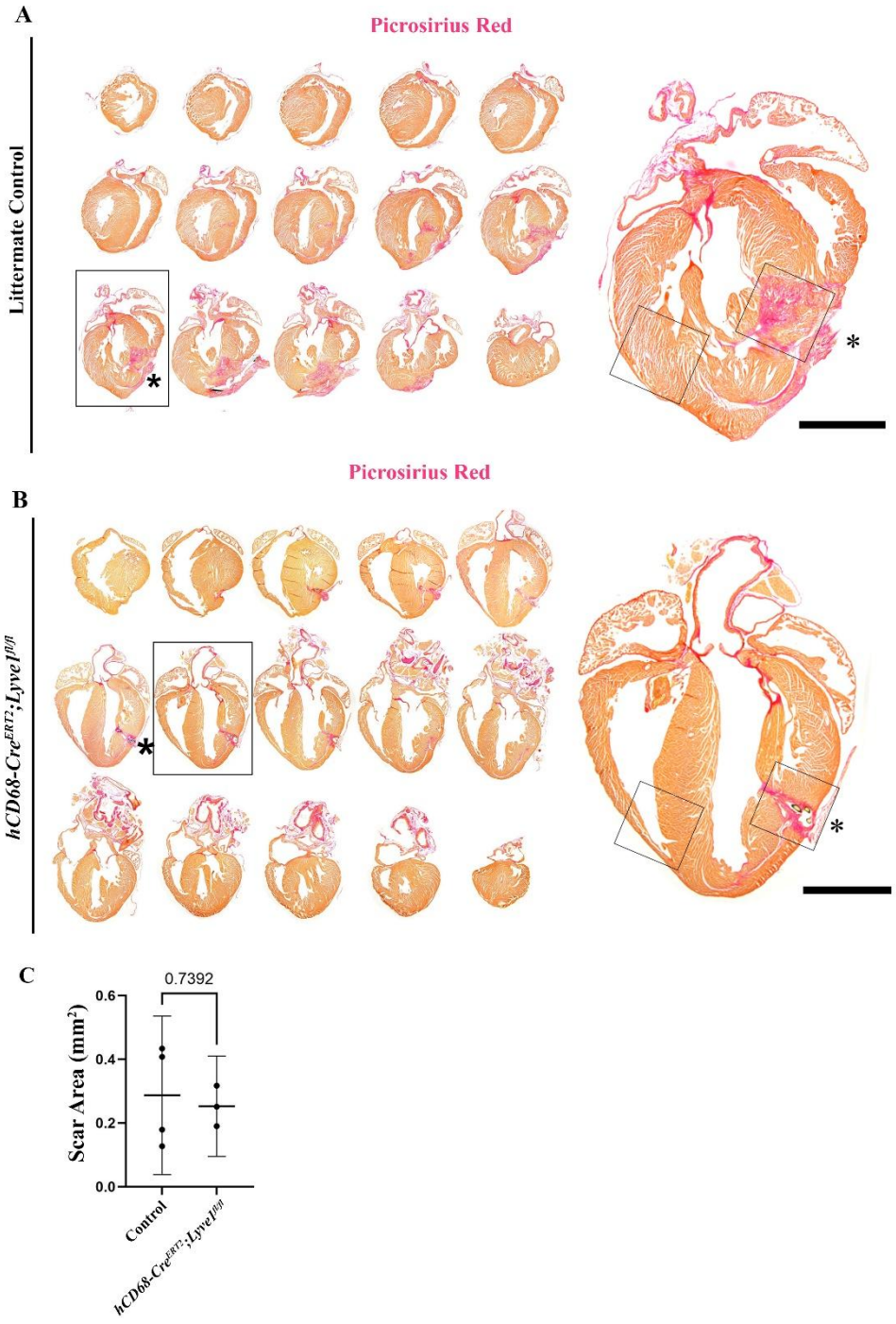

Figure 5-7. Quantification of *hCD68-CreERT2;Lyve1*$^{fl/fl}$ infarct scar at 28dpi.

Representative serial long-axis sections from *Cre*- littermate control (A) and *hCD68CreERT2;Lyve1*$^{fl/fl}$ (B) hearts 28 days after P2 MI following tamoxifen at P1.Sections

were stained with Picrosirius Red to visualise collagen. Insets highlight infarct/distal zones; asterisks mark the infarct. Scar area was quantified in sections with the largest infarct per heart (C). n = 4 for *Cre*- and n = 3 for *Cre*+ hearts. Scale bars: 1 mm. Significant differences were calculated using unpaired two-tailed Student's t-test.

Given the established role of macrophages in infarct neovascularisation, I then conducted further histological analyses with CD31/PECAM immunostaining, in line with previous work[55]. This approach was used in the seminal paper demonstrating that macrophages have a role in revascularisation during regenerative repair[55] as follows: "In monocyte/macrophage-depleted hearts, PECAM staining was sparse in the [infarct zone]…" "Defects in neovascularization following cardiac injury in monocyte/macrophage-depleted neonates imply that P1 monocytes/macrophages directly or indirectly influence neovascularization during cardiac regeneration."

Intriguingly, analysis of control versus *hCD68-CreERT2;Lyve1*$^{fl/fl}$ PECAM1 staining within the infarct zone revealed an impaired vascular response at day 7 post-MI in the macrophage-specific mutants post-MI (Figure 5-8). There were no significant differences in macrophage cell density within the infarct zone between conditions, demonstrated by quantification of IBA1 immunofluorescent staining (Figure 5-8).

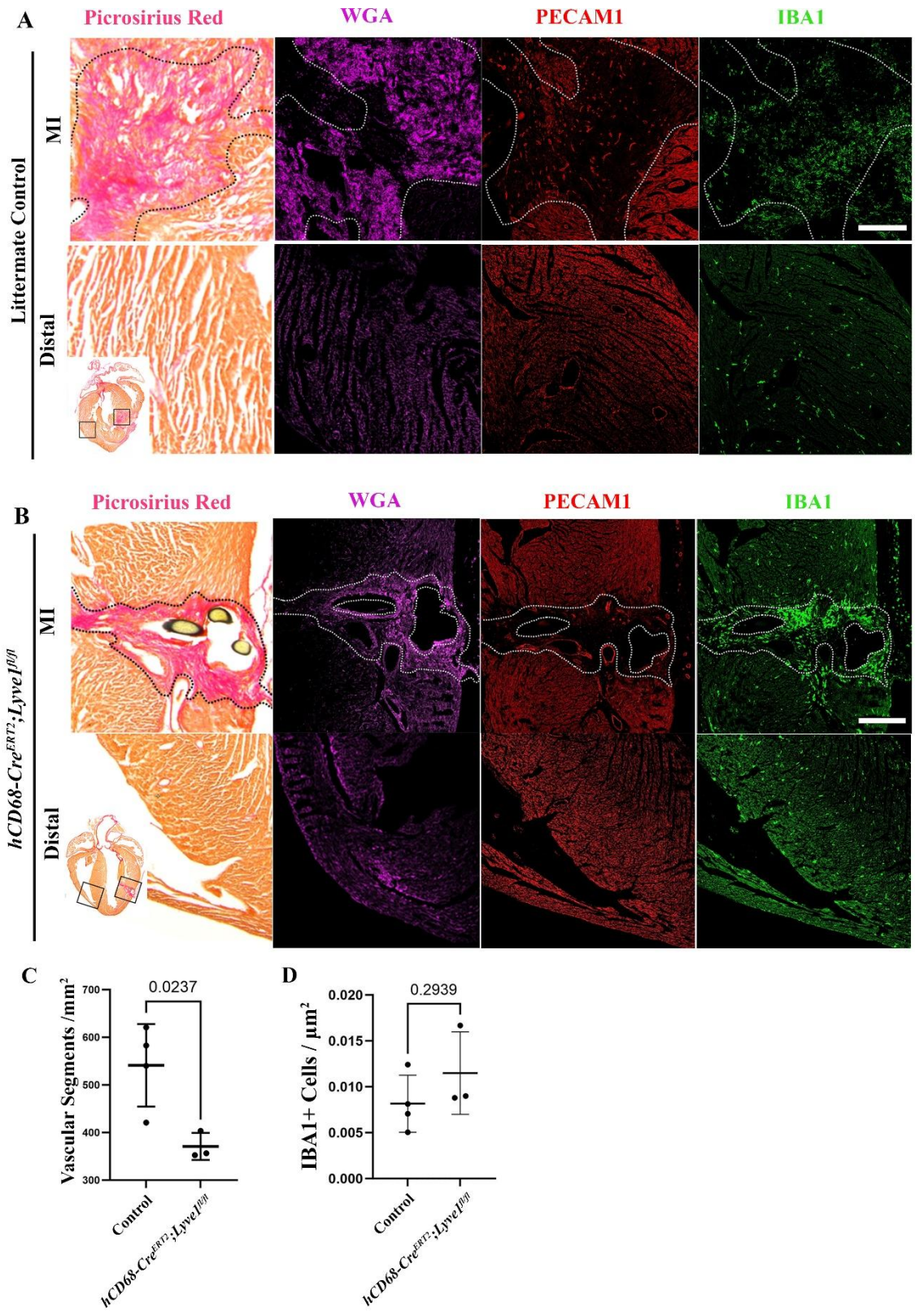

Figure 5-8. Infarct zone histology: scar, neovascularisation, and macrophages.The infarct zone was identified by wheat germ agglutinin (WGA) fibrosis stain, consistent with regions already defined by picrosirius red stain. Staining for PECAM1 (CD31), a well-established marker for endothelial cells, allowed visualisation of the neovascular response within the infarct zone. IBA1 staining was used to identify macrophages within the infarct zone in control (A) and *hCD68-CreERT2;Lyve1*$^{fl/fl}$ (B) hearts at 7 days following MI at P2. Quantification of discrete PECAM1

signal within the infarct zone revealed significantly-reduced PECAM1-stained vasculature in *hCD68-CreERT2;Lyve1*$^{fl/fl}$ hearts (C). Quantification of macrophage cell density by IBA1 stain within the infarct zone revealed no significant difference between conditions (D). n = 4 control hearts, n = 3 *hCD68–CreERT2;Lyve1*$^{fl/fl}$ hearts; four sections per heart. Scale bar: 200 μm.

5.4 Discussion

In this chapter, I investigated the effect of macrophage-specific knockout of *Lyve1* in neonatal heart regeneration using the *hCD68-CreERT2;Lyve1*$^{fl/fl}$ line.

5.4.1 Macrophage-specific *Lyve1* knockdown in the neonatal mouse

A pan-myeloid marker, CD68, was employed to target deletion of *Lyve1* across all macrophage subsets. Given the predominance of tissue-resident macrophages in the neonatal response to cardiac injury[54], any observed phenotype from this intervention is attributable to CCR2^{-}LYVE-1^{+} macrophage population. Thus, conditional deletion of *Lyve1* with a *hCD68-CreERT2*;*Lyve1*$^{fl/fl}$ construct was used experimentally to assess the contribution of tissue-resident macrophage LYVE-1 to neonatal cardiac regeneration.

The inducible *CreERT2* knockout model was used to allow conditional knockout and avoid targeting *Lyve1* during development which – as established in unpublished scRNA-seq work in the *Lyve1*$^{-/-}$ setting – alters the immune populations present in the uninjured heart, even in the absence of other observable phenotype[116]. Tamoxifen administration was therefore carried out postnatally.

It was not feasible to perform concurrent intraperitoneal tamoxifen injection and MI-inducing surgery at P1 due to high mortality risk. Therefore, injections were carried out at P1, and MI surgeries were conducted at P2. Though a less-commonly used timepoint, P2 lies within the regenerative window of the neonatal mouse and full cardiac

regeneration does occur following ischaemic injury[44]. However, alternative routes of tamoxifen administration have been explored to minimise mortality and facilitate P1 MI induction in future work. An established alternative is the intraperitoneal delivery of tamoxifen to the dam immediately postnatally, to avoid disrupting parturition, with subsequent delivery to pups via the milk[44]. This method would facilitate continuous dosing across the first week of life and may be deployed in future studies.

The *hCD68-CreERT2* line has previously been characterised in adults, but no studies currently exist characterising the efficiency of targeting in the neonatal heart[120]. Here, subjecting the *hCD68-CreERT2;R26TdTomato* line to the neonatal MI protocol, recombination efficiency was determined to be ~66% at 7 days post-injury (dpi) – lower than reported for adults in liver (~80%)[120]. The single tamoxifen dose, rather than multiple[120], and the expansion of the resident macrophage population during the 7 days post-MI likely contributed towards this reduced efficiency. Nonetheless, this analysis confirmed a single dose of tamoxifen is sufficient for macrophages affected by *Cre* recombination at P1 to be present within the regenerating heart up to 7dpi.

5.4.2 Macrophage LYVE-1 is required for cardiac regeneration

Intriguingly, macrophage-specific deletion of *Lyve1* provoked an impaired regenerative response post-MI, recapitulating the global knockout phenotype. This impairment was characterised by reduced neovascularisation and impairment of cardiac functional recovery.

The functional readout does not reveal significant differences in ejection fraction (EF) or fibrotic area though the data certainly indicate a trend towards decreased EF in the injured

hCD68-CreERT2;Lyve1$^{fl/fl}$ mice. However, we observe significant reduction in both cardiac output and stroke volume. Cardiac output is regarded as a significant indicator of overall cardiac function, taking both stroke volume and heart rate into account. For example, heart failure with preserved ejection fraction (HFpEF) which is a major clinical burden, cannot be diagnosed by EF measurements alone. While the extent of fibrotic area is not significantly different between conditions, we do not propose that cardiac outcomes post-MI are inextricably linked to scar area. We observe a difference in the neovascular response that could account for functional impairment, for example via altered oxygen/nutrient delivery to surviving cardiomyocytes.

It is known that macrophages actively participate in angiogenesis and that disrupted coronary angiogenesis contributes to impaired cardiac regeneration in macrophage-depleted mice[55,77]. Here, *hCD68-CreERT2-Lyve1*$^{fl/fl}$ mice revealed a significantly reduced neovascular response within the scar region at 7dpi compared to controls. It would be beneficial to repeat this analysis in a *Cx3cr1-CreERT2;Lyve1*$^{fl/fl}$ cross to confirm specificity to tissue-resident macrophages. There is also scope to assess the neovascular process in 3-dimensions using whole-mount staining and tissue-clearing, which would allow quantification of macrophage proximity to vessels.

My findings on the neovascular response post-MI supports the case for a pro-angiogenic role of LYVE-1 proposed in other studies[151,152]. LYVE-1^{+} macrophages are necessary for angiogenesis in epididymal adipose tissue, inducing secretion of matrix metalloproteases (MMP-9, MMP-7, MMP-12), CXCL12, and activation of the VEGF-VEGFR2 system[151]. Enforced expression of *Lyve1* in a monocyte cell line increased mRNA expression of pro-angiogenic MMPs (*Mmp2, Mmp9*), as well as *Vegfa*[152]. The ability of lymphatic

endothelial LYVE-1 to directly interact with FGF to induce lymphangiogenesis via the VEGF-VEGFR2 system also provides a potential avenue of investigation[153], with the implication that FGF may also bind to macrophage LYVE-1.

Despite reduced neovascularisation, there was no significant difference in fibrosis between *hCD68-CreERT2;Lyve1*$^{fl/fl}$ and control hearts at 7dpi. However, this result was also observed in the global knockout, and not entirely unexpected as 7dpi is too early for complete scar resolution to be observed in wildtype animals and so any failure in resolution may not yet be apparent[55]. By 28dpi some divergence in capacity of *hCD68-CreERT2;Lyve1*$^{fl/fl}$ and control mice to resolve fibrosis became apparent, with *hCD68-CreERT2;Lyve1*$^{fl/fl}$ hearts trending towards increased scar area. Existing work demonstrates macrophages are capable of direct collagen deposition post-MI[78], and that LYVE-1-expressing macrophages mediate vascular arterial tone by degrading collagen on smooth muscle cells via MMP-9-dependent proteolysis following binding of LYVE-1 to hyaluronan in the pericellular matrix[154].

The presence of functional impairment aligns with that observed in constitutive *Lyve1*$^{-/-}$ mice at 28dpi following MI at P1. Given the same functional effect was observed in both global and CD68-specific deletions of *Lyve1*, I conclude that it is highly likely the contribution of *Lyve1* to cardiac regeneration is macrophage-specific acting at the level of pro-regenerative tissue-resident macrophages.

5.5 Summary

Macrophage-specific *Lyve1* deletion in the neonatal heart before MI induction at P2 impaired cardiac regeneration, recapitulating the phenotype observed in the global *Lyve1*

knockout. Compared to littermate controls, I observed impaired cardiac function on cine-MRI and a reduced neovascular response by infarct capillary-density assessment. These findings establish that LYVE-1 in tissue-resident macrophages is required for neonatal cardiac regeneration. The mechanistic basis for this requirement is examined in the next chapter.

6 RESULTS III: LOSS OF LYVE-1 PREDISPOSES TISSUE-RESIDENT MACROPHAGES TO APOPTOSIS, FACILITATING REPLACEMENT BY INFILTRATING MACROPHAGES AND MONOCYTES

6.1 Background

In the previous chapter, I established that loss of *Lyve1* in tissue-resident macrophages impairs neonatal cardiac regeneration. In this chapter, I investigate the possible function of LYVE-1 in these macrophages that, when disrupted, prevents an effective regenerative response.

The most definitive demonstration of LYVE-1 function comes from the lymphatics, where LEC LYVE-1 mediates HA-dependent 'cup' formation and passage of dendritic cells into the lymphatic lumen[103,104]. Few studies describe the function of LYVE-1 on macrophages.

Across organs, LYVE-1 marks a tissue-resident subset of macrophages with matrix-maintenance and vessel-support functions. In arterial walls, LYVE-1$^+$ perivascular macrophages degrade smooth muscle collagen via MMP-9 and thereby help maintain arterial tone. Macrophage depletion or disruption of this axis increases collagen stiffness, establishing a direct role for the subset in vascular homeostasis[154]. Beyond the vasculature, LYVE-1$^+$ macrophages form stromal niches that influence tissue remodelling, for example modulating adipocyte stem cells in white adipose tissue and shaping hyaluronan-rich extracellular matrix in mammary gland[155,156]. These studies primarily ascribe functions to the LYVE-1$^+$ macrophage subset as a whole (i.e., cells identified by LYVE-1 expression), rather than demonstrating a requirement for the LYVE-1 receptor within those macrophages.

More broadly, work on the LYVE-1 homologue CD44 provides mechanistic precedent for HA-dependent control of macrophage behaviour. CD44 functions as a phagocytic/efferocytic receptor for apoptotic cells, and cross-linking CD44 enhances macrophage phagocytosis, whereas disruption of the HA glycocalyx impairs uptake[104,114,157].

6.2 Aims

To define a likely mechanism for how loss of LYVE-1 on macrophages impairs the regenerative response.

In this chapter I aim to identify mechanisms by which loss of *Lyve1* in macrophages impairs neonatal cardiac regeneration after MI: (1) Identify differentially expressed genes and enriched pathways between wildtype and *Lyve1*$^{-/-}$ macrophage subsets by scRNA-seq of CD45^{+} cells at P2MI7 dpi. (2) Validate findings *in vivo*. (3) Interrogate mechanisms *in vitro* using LYVE-1^{+} bone-marrow–derived macrophages (BMDMs) to manipulate *Lyve1* expression, assaying effects on phagocytosis/efferocytosis, survival, and angiogenesis. (4) Integrate findings to propose a mechanistic model.

6.3 Results

6.3.1 scRNA-seq analysis

6.3.1.1 CD45^{+} cell clustering analysis

To interrogate the molecular role of LYVE-1 in macrophages, scRNA-seq analysis of pooled CD45^{+} enriched cells from neonatal *Lyve1*$^{-/-}$ versus wildtype (WT) hearts (n = 5 per group) at P2MI7dpi was conducted, thus capturing all immune cells including macrophages at a timepoint consistent with the observed impaired neovascularisation in

hCD68-CreERT2;Lyve1$^{fl/fl}$ animals (Figure 6-1). Hearts were pooled due to the technical challenge of isolating or pooling sufficient macrophage for analysis identified in earlier flow cytometry experiments (Figure 5-3). *Lyve1*$^{-/-}$ hearts were used instead of *hCD68-CreERT2;Lyve1*$^{fl/fl}$ to allow harvesting of whole litters at the required timepoint with 100% genotype, avoiding early genotyping and the higher tamoxifen-related mortality in mixed-genotype litters that would make pooling per group unreliable. In addition, *CreERT2*-mediated deletion in macrophages is not 100% efficient, hence residual *Lyve1* would dilute differential signals in scRNA-seq, whereas the global knockout provides a clean comparator. It should be noted that this leaves open the possibility that any phenotype observed may be due to disruption of outgoing lymphatic signalling possibly mediated by LYVE-1. I thus focused our analysis on the macrophage subsets specifically.

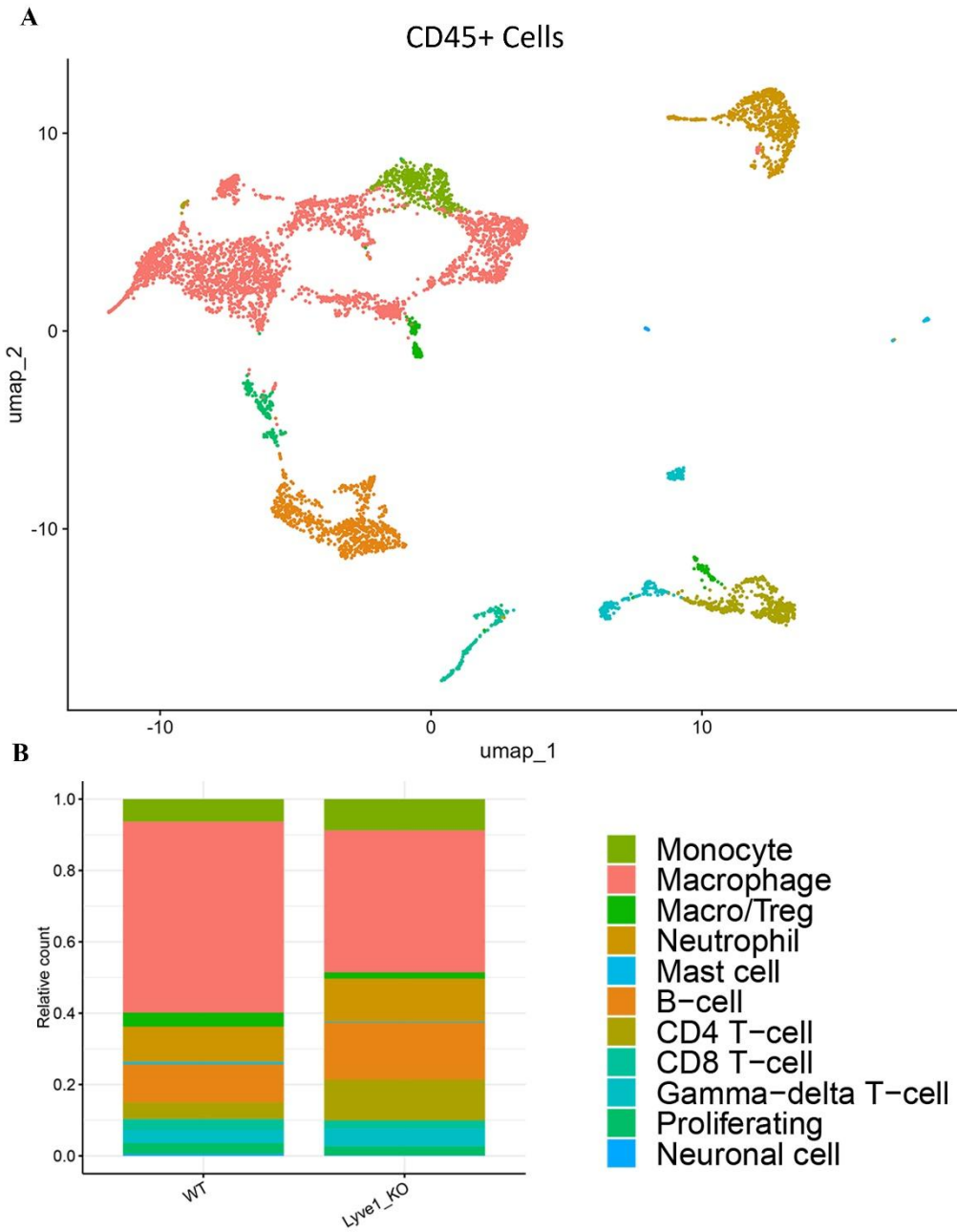

Figure 6-1. Wildtype versus *Lyve1*$^{-/-}$ P2MI7dpi scRNA-seq dataset.ScRNA-seq was conducted, comparing CD45^{+} enriched cells from neonatal *Lyve1* knockout versus WT hearts at P2MI7dpi. The samples were FACS-sorted using 7AAD and CD45 to isolate live CD45^{+} cells and libraries were prepared for sequencing using the 10x Genomics platform. UMAP plot of grouped wildtype and *Lyve1*-KO CD45^{+} cells (A). Comparison of CD45^{+} cell subset proportions between wildtype and *Lyve1*-KO conditions (B).

6.3.1.2 Macrophage sub-cluster analysis

scRNA-Seq is often carried out on pooled samples across genotypes/treatments to enable sufficient cells to be sequenced however this precludes statistical analyses across

biological replicates. To facilitate statistical analysis of pooled samples, deconvolution of individuals by unique single nucleotide polymorphisms (SNPs) per heart was carried out by Dr M. Weinberger using vireo5[128] (Figure 6-2). Initial clustering identified macrophage subsets, grouped broadly as monocytes, $CCR2^{+}$ macrophages, and CCR2- macrophages (Figure 6-2). We observed statistically significant reductions in the CCR2- sub-population cell neighbourhoods (p = 0.012 - 4.51E-9) and corresponding statistically significant elevation of the $CCR2^{+}$ sub-population in the *Lyve1*$^{-/-}$ samples compared to wildtype (p = 0.014 - 0.00067) (Figure 6-2). This represents a loss of the tissue-resident macrophage population, which is replaced by monocyte-derived populations in the knockout background. Importantly, the *Lyve1*$^{+}$ macrophage cluster identified in wildtype was still present in the knockout setting, albeit in significantly smaller numbers and without expressing *Lyve1*, confirming loss of *Lyve1* does not result in complete loss of this sub-population (Figure 6-3).

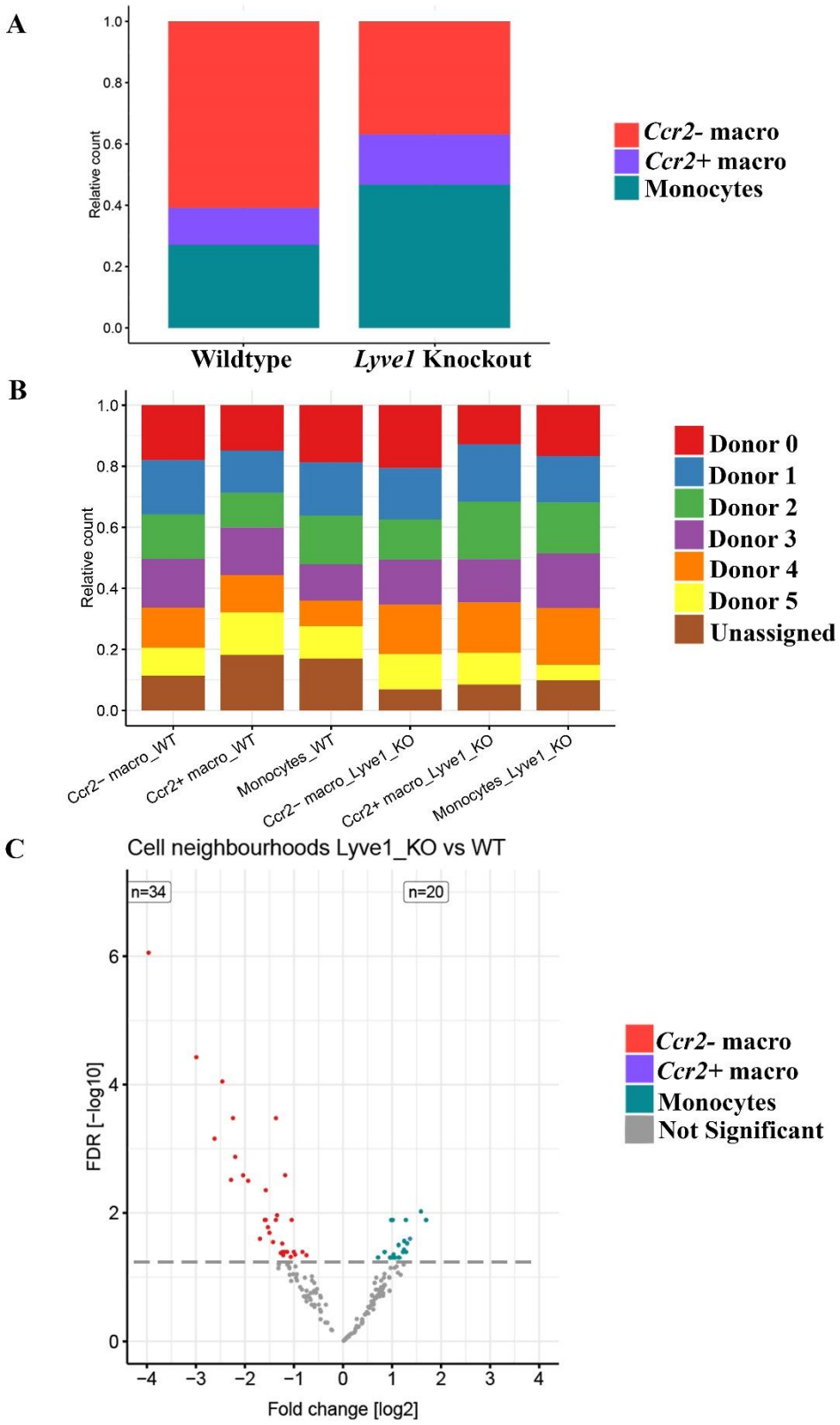

Figure 6-2. Macrophage subcluster differential abundance.Stacked bar chart illustrating the differential abundance of macrophage subclusters, there is a significant reduction in the number and proportion of *Ccr2*- (tissue-resident) macrophages, with an accompanying increase in number of infiltrating *Ccr2*$^{+}$ macrophages and monocytes (A). By de-multiplexing the pooled hearts according to SNPs, quantification of subcluster proportion by donor was possible, revealing similar proportions between animals (B). Cell-neighbourhoods were compared, which revealed

the observed reduction in *Ccr2*- cells and increase in *Ccr2*$^{+}$ cells were both statistically significant (C).

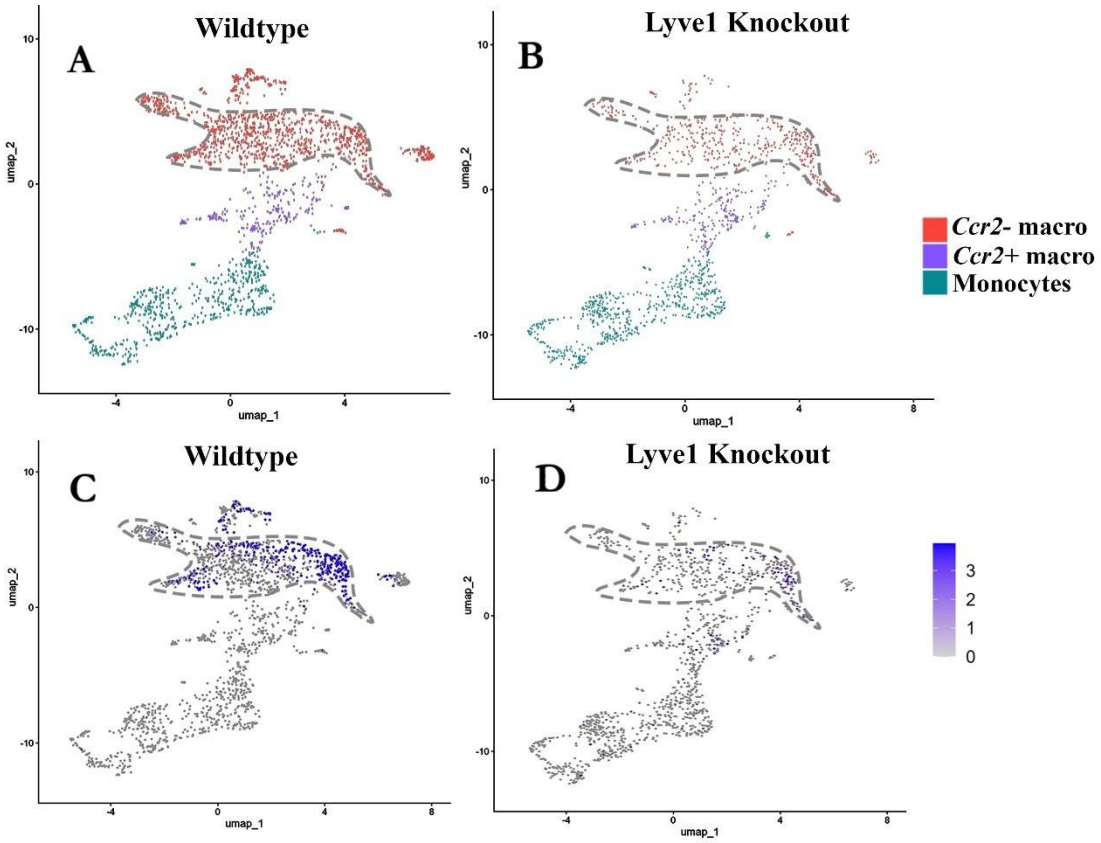

Figure 6-3. Visualisation by UMAP of macrophage subclusters.Wildtype UMAP coloured by identity showing three populations present at P2MI7dpi: tissue-resident *Ccr2*- macrophages (dotted outline), Ccr2+ macrophages, and monocytes (A). *Lyve1*$^{-/-}$ UMAP illustrating the same three populations, indicating preservation of the resident *Ccr2*- subcluster despite *Lyve1* knockout (B). Feature plot of *Lyve1* expression in wildtype; signal is largely restricted to the *Ccr2*- macrophage subcluster (C). Feature plot of *Lyve1* in the knockout showing near-background expression with persistence of the *Ccr2*- cluster (D).

6.3.1.3 GO term and DEG analysis

To determine to what extent shifting *Ccr2*$^{+}$/*Ccr2*-/monocyte populations alone are responsible for worsened functional outcomes, unbiased gene ontology (GO) and differential gene expression (DEG) analysis were conducted within macrophage subclusters to identify any alteration in molecular phenotype between wildtype and *Lyve1*$^{-/-}$.To examine whether the phenotype of resident macrophages changes in addition

to their proportions, we compared transcriptional profiles within the *Ccr2*$^{-}$ *Lyve1*$^{+}$ subcluster at P2MI7dpi (Figure 6-4). As expected, *Lyve1* itself was strongly reduced in the knockout. Beyond this internal control, several transcripts were lower in *Lyve1*$^{-/-}$ than wildtype (e.g. *Trim12a*/*Trim30d*, *Mid1*, *Rnf141*, *Dynlt1b*), whereas others were increased in the knockout, including genes linked to membrane organisation/lipid handling and signalling (*Atp11a*, *Plekha7*, *Gdpd3*, *Wdfy1*, *Pde2a*, *Lars2*).

GO analysis of the knockout-upregulated set (Figure 6-5) was dominated by translation-related Molecular Function terms (structural constituent of ribosome, rRNA binding, aminoacyl-tRNA ligase activity) and Cellular Component terms mapping to small/large ribosomal subunits and mitochondrial/respiratory-chain complexes, with additional enrichment for recycling endosome. The data suggest that, when *Lyve1* is knocked out, the population of macrophages corresponding to the LYVE1+ subset in wildtype are characterised by increased protein-synthesis capacity and mitochondrial/vesicular machinery, alongside shifts in membrane-lipid and cyclic-nucleotide pathways. These differences occur within the resident subcluster, so they are not attributable to changes in the balance of Ccr2^{+} vs Ccr2^{-} cells alone.

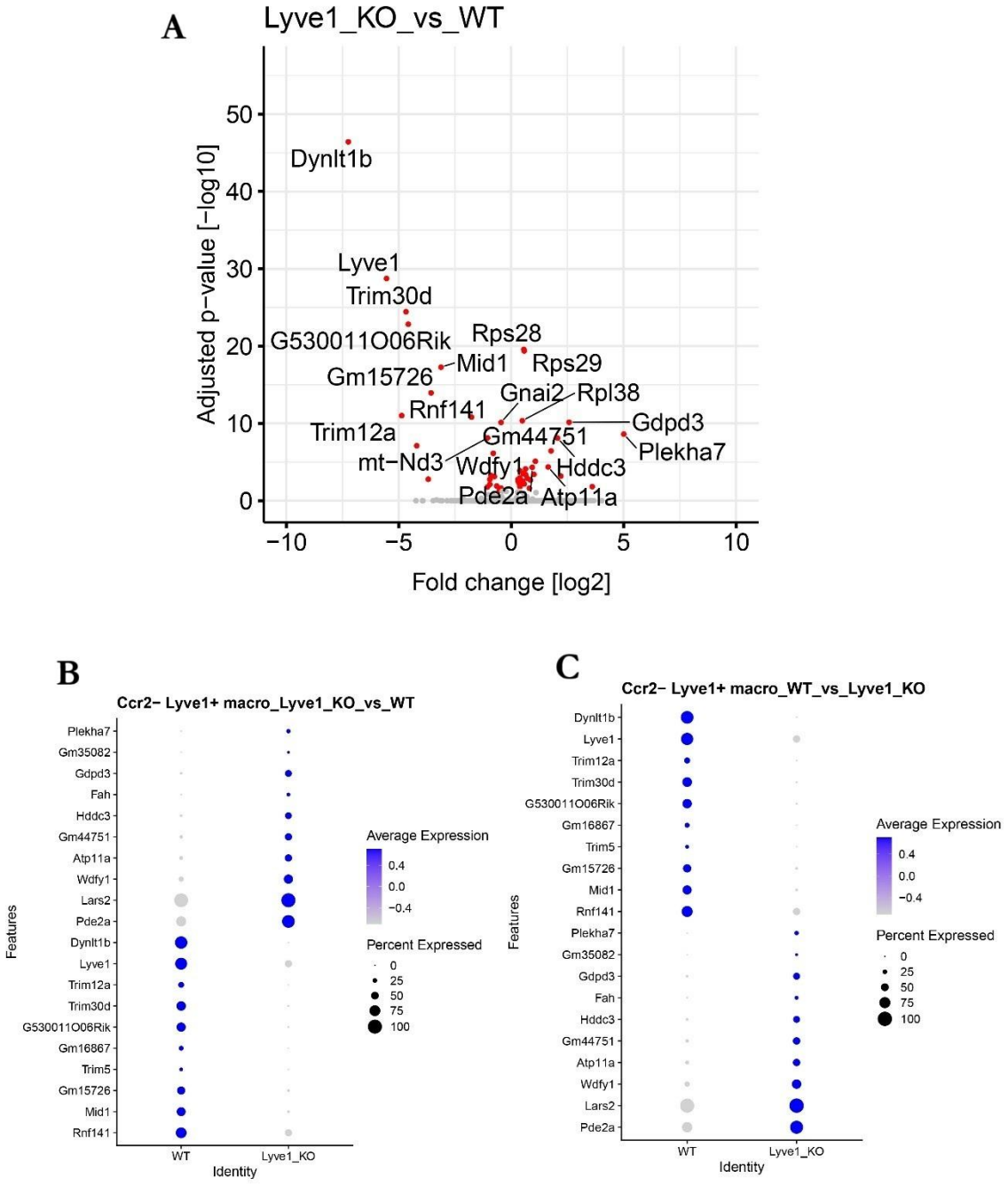

Figure 6-4. Differential expression within *Ccr2*$^{-}$ macrophage subcluster.

ScRNA-seq datasets were integrated and the *Ccr2*$^{-}$ *Lyve1*$^{+}$ macrophage subcluster was compared between wildtype and *Lyve1*$^{-/-}$ at P2MI7dpi. Visualisation of DEGs in *Lyve1*$^{-/-}$ vs wildtype by volcano plot; each point is a gene; selected genes are labelled (A). Dot plot of representative knockout-enriched genes in the *Ccr2*$^{-}$ *Lyve1*$^{+}$ subcluster; dot size indicates percentage of cells expressing the gene; colour scale indicates average scaled expression (B). Dot plot of representative wildtype-enriched genes in the same subcluster (C), displayed as in B.

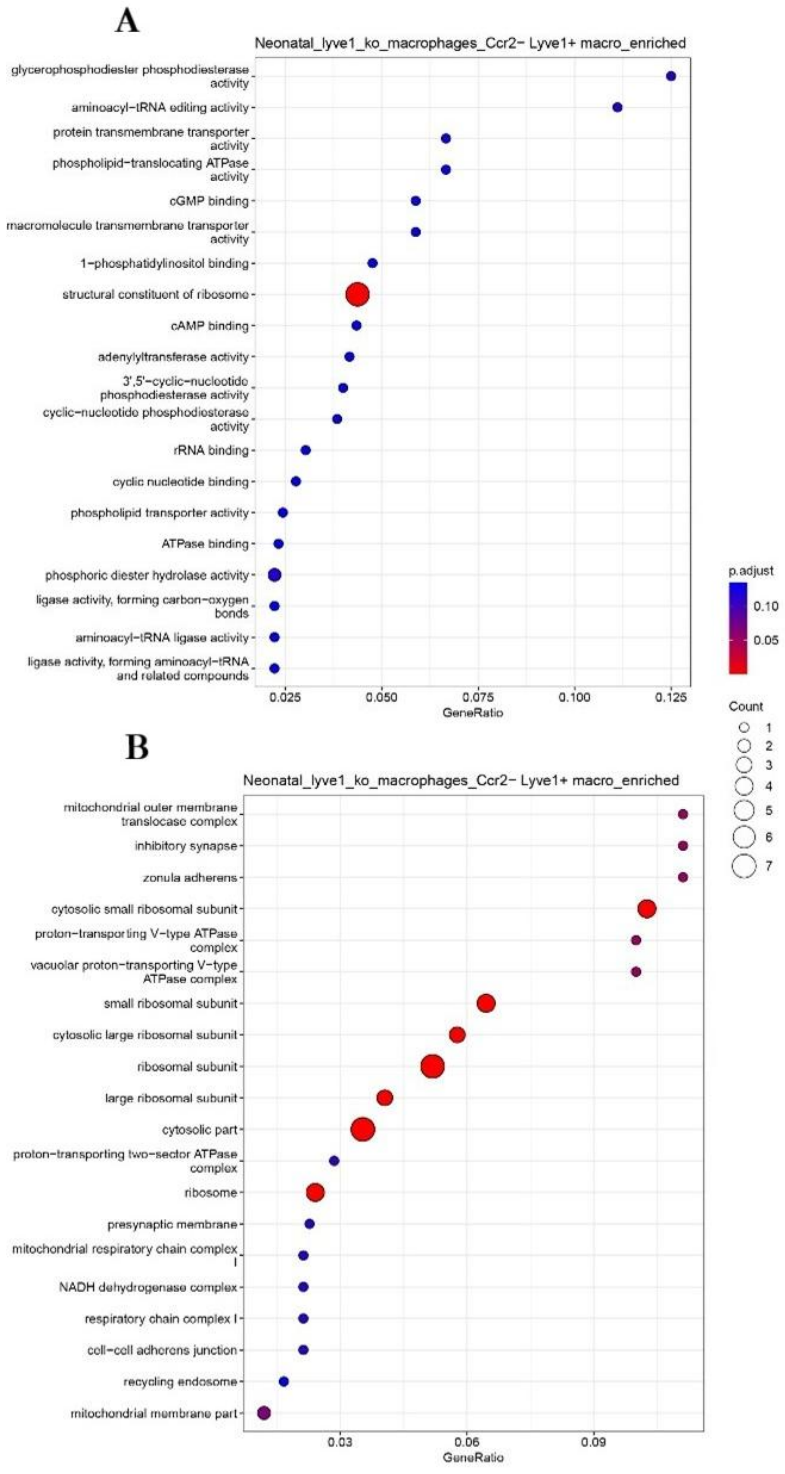

Figure 6-5. GO enrichment of DEGs in the *Ccr2*$^{-}$ *Lyve1*$^{+}$ subcluster.

Molecular function terms enriched in knockout-upregulated genes, dominated by translation-related functions; e.g., structural constituent of ribosome, rRNA binding, aminoacyl-tRNA ligase activity, with additional phospholipid-translocating ATPase activity (A). Cellular

component terms enriched in knockout-upregulated genes, highlighting ribosomal small/large subunits, mitochondrial membrane/respiratory-chain complexes, and recycling endosome (B).

Subsequently, the DEG analysis was narrowed to examine genes associated with pro-angiogenic, pro-fibrotic, and pro-inflammatory macrophage phenotypes (Figure 6-6). This further analysis demonstrated alignment of our three identified populations (monocytes, CCR2^{+}, CCR2-) with previously reported signatures in terms of effects on angiogenesis, fibrosis, and inflammation. These gene expression profiles were unchanged between wildtype and knockout conditions, strengthening the likelihood that the observed phenotype in the *Lyve1* knockout background is due to an effect on the reduced CCR2- macrophage population leading to increased inflammatory monocyte recruitment, rather than due to any shift in molecular phenotype of LYVE-1^{+} macrophages.

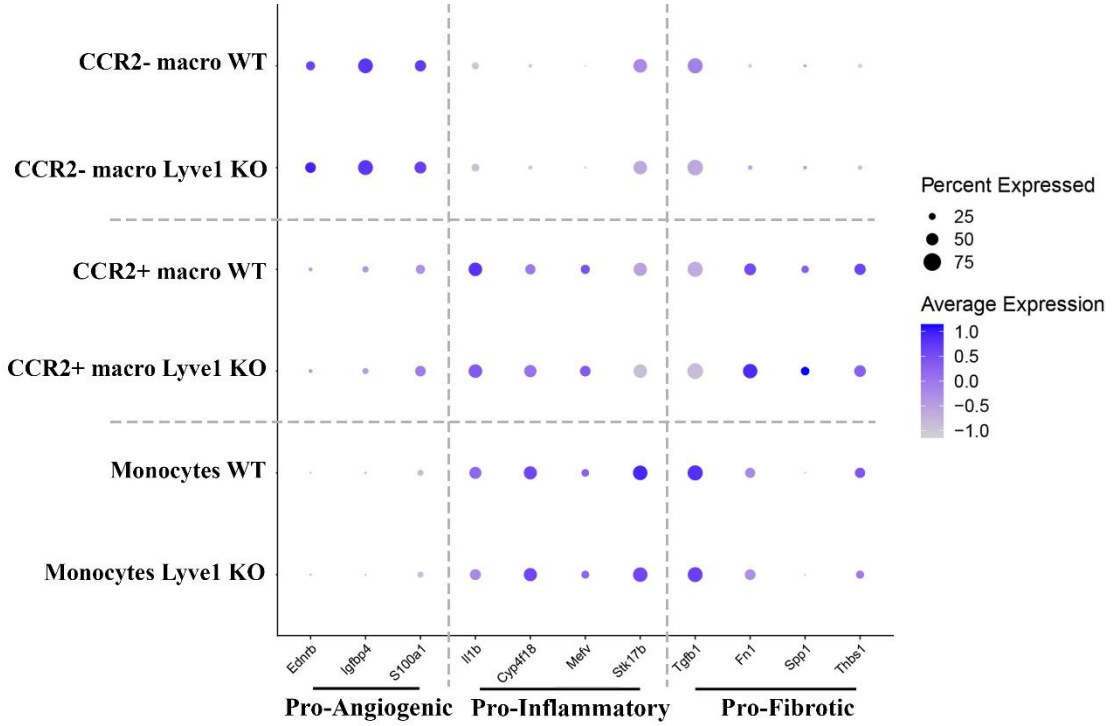

Figure 6-6. Dot plot mapping macrophage subcluster phenotypes by gene.The dot plot illustrates relative expression of key pro-angiogenic, pro-inflammatory and pro-fibrotic genes in each macrophage subset and between WT and *Lyve1*$^{-/-}$. Within subclusters, there is little difference in GO terms or DEGs relating to angiogenesis, fibrosis, or inflammation between wildtype and

knockout conditions. Between subclusters, there is a clear propensity of *Ccr2*$^{+}$ macrophages and monocytes towards pro-inflammatory and pro-fibrotic traits, while *Ccr2*$^{-}$ macrophages possess a more pro-angiogenic signature.

6.3.1.4 Speculative Mechanism for Shift in Macrophage Subpopulations

Given the shift in macrophage subpopulations is the apparent sole driver in reparative impairment, the mechanism behind this shift was investigated further. The reduction in CCR2- macrophages was accompanied by a statistically significant increase in apoptotic marker expression (Figure 6-7) and decreased proliferative marker expression within this subset (Figure 6-7). In CCR2^{+} macrophage and monocyte populations, there is no change in apoptotic or proliferative score (Figure 6-7). Increased macrophage apoptosis was validated *in vivo* via staining WT and *Lyve1* knockout hearts for F4/80 and the apoptosis marker cleaved caspase 3 (CC3) at 7 days following MI at P2, matching the timepoint of the single-cell dataset. Staining revealed a significant increase in the number of cells co-expressing CC3 and F4/80 in knockout hearts post-MI (Figure 6-7).

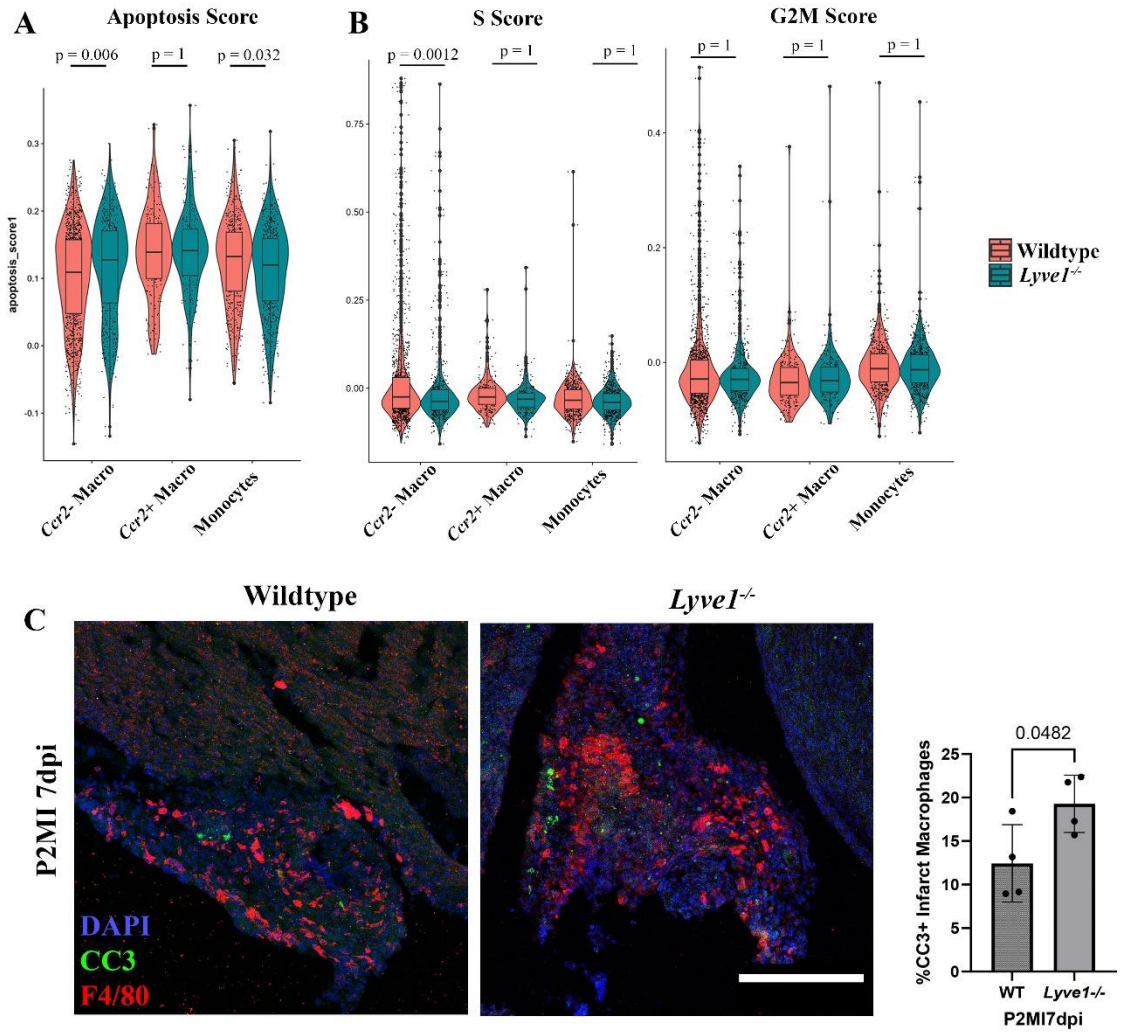

Figure 6-7. Assessment of apoptotic markers in the scRNA-seq dataset and *in vivo*.Violin plot showing cumulative apoptotic marker expression scores between conditions and macrophage subsets; there is an increased apoptotic marker score for the *Ccr2*- macrophage subcluster, likely accounting for the reduction in this population in the *Lyve1* knockout setting (A). Cumulative expression scores of cell cycle markers showed a decrease in *Lyve1*$^{-/-}$ *Ccr2*- macrophage proliferation, but no change in *Ccr2*$^{+}$ or monocytes (B). *In vivo* validation of increased apoptosis; CC3 co-expression with F4/80 within the infarct zone 7 days following MI at P2 was significantly increased in the *Lyve1*$^{-/-}$ context (C). Bonferroni-corrected pairwise Wilcoxon rank-sum test was used to determine significance in A, B. Unpaired Student's t tests were used to determine significance in C. n = 4, 4 for C. Scale bar: 200 μm.

To investigate the mechanism by which loss of *Lyve1* predisposes CCR2- macrophages to apoptosis, I considered the known role of the LYVE-1 homologue CD44 in dendritic cells and certain macrophage populations, where it anchors the hyaluronic acid (HA) glycocalyx. It is known that *Cd44* knockout disrupts the dendritic cell glycocalyx and

predisposes the cell to apoptosis by revealing pro-apoptotic elements on its surface[104,158]. Furthermore, our scRNA-seq analysis revealed CD44 expression was significantly lower in the CCR2- macrophage population (where LYVE-1 is expressed), compared to $CD44^{+}$ macrophages and monocytes, suggesting LYVE-1 may substitute the role of CD44 in this subpopulation (Figure 6-8). I, therefore, carried out immunostaining for hyaluronic acid binding protein (HABP) to confirm the presence of a HA glycocalyx in $LYVE\text{-}1^{+}$ macrophages in WT mice 7 days following MI at P2 (Figure 6-9). Subsequently, I examined representative images of macrophages between WT and *Lyve1*$^{-/-}$ hearts at 7 days following MI at P2 and identified an apparent loss or notable reduction of glycocalyx in a proportion *Lyve1*$^{-/-}$ macrophages (Figure 6-9) suggesting that these cells may be predisposed to apoptosis in the absence of LYVE-1 as previously described for dendritic cells in the context of CD44[104,158]. Accurate visualisation and quantification of the HA glycocalyx is inherently challenging in the infarcted neonatal heart, given the large amount of extracellular matrix HA deposited in this setting preventing accurate delineation of morphology.

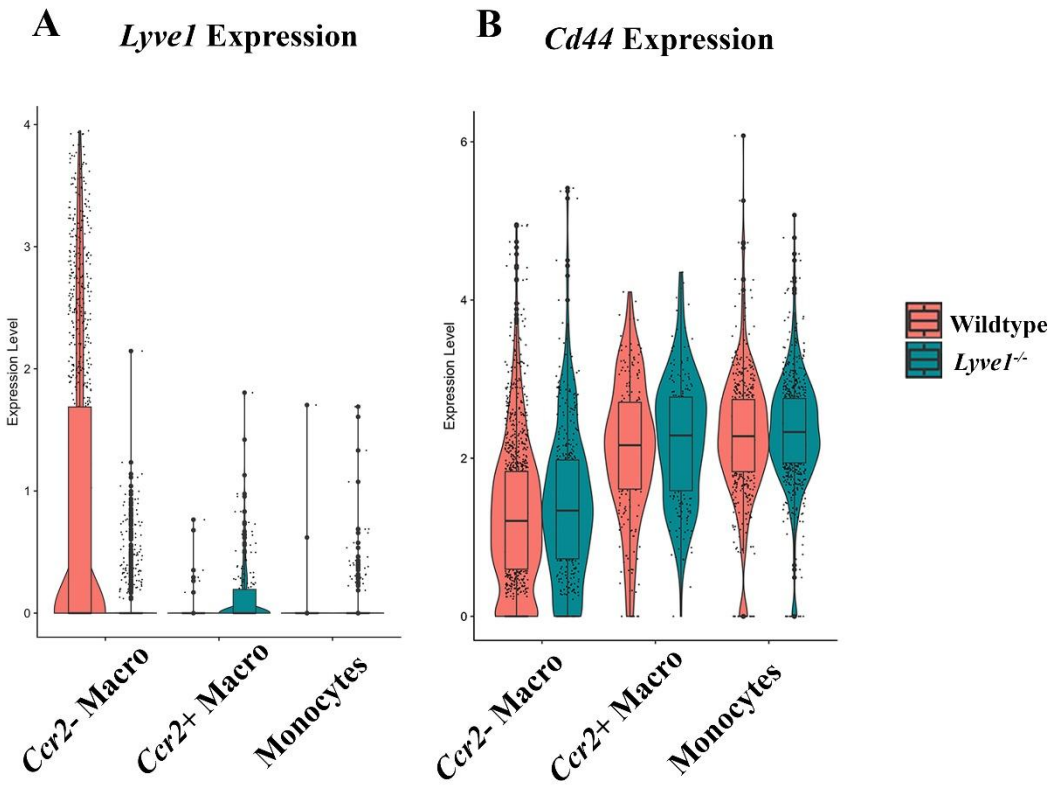

Figure 6-8. Differential expression of *Lyve1* and *Cd44* in macrophage subclusters.Violin plot indicating expression of *Lyve1* is restricted to the wildtype *Ccr2*$^{-}$ macrophage subcluster and is absent in the knockout (A).Violin plot indicating expression levels of the *Lyve1* homologue *Cd44* were significantly reduced in the *Ccr2*$^{-}$ macrophage cluster – where *Lyve1* is expressed – but were unchanged following loss of *Lyve1* (B).

6.3.1.5 Glycocalyx Visualisation in wildtype and *Lyve1*$^{-/-}$ hearts

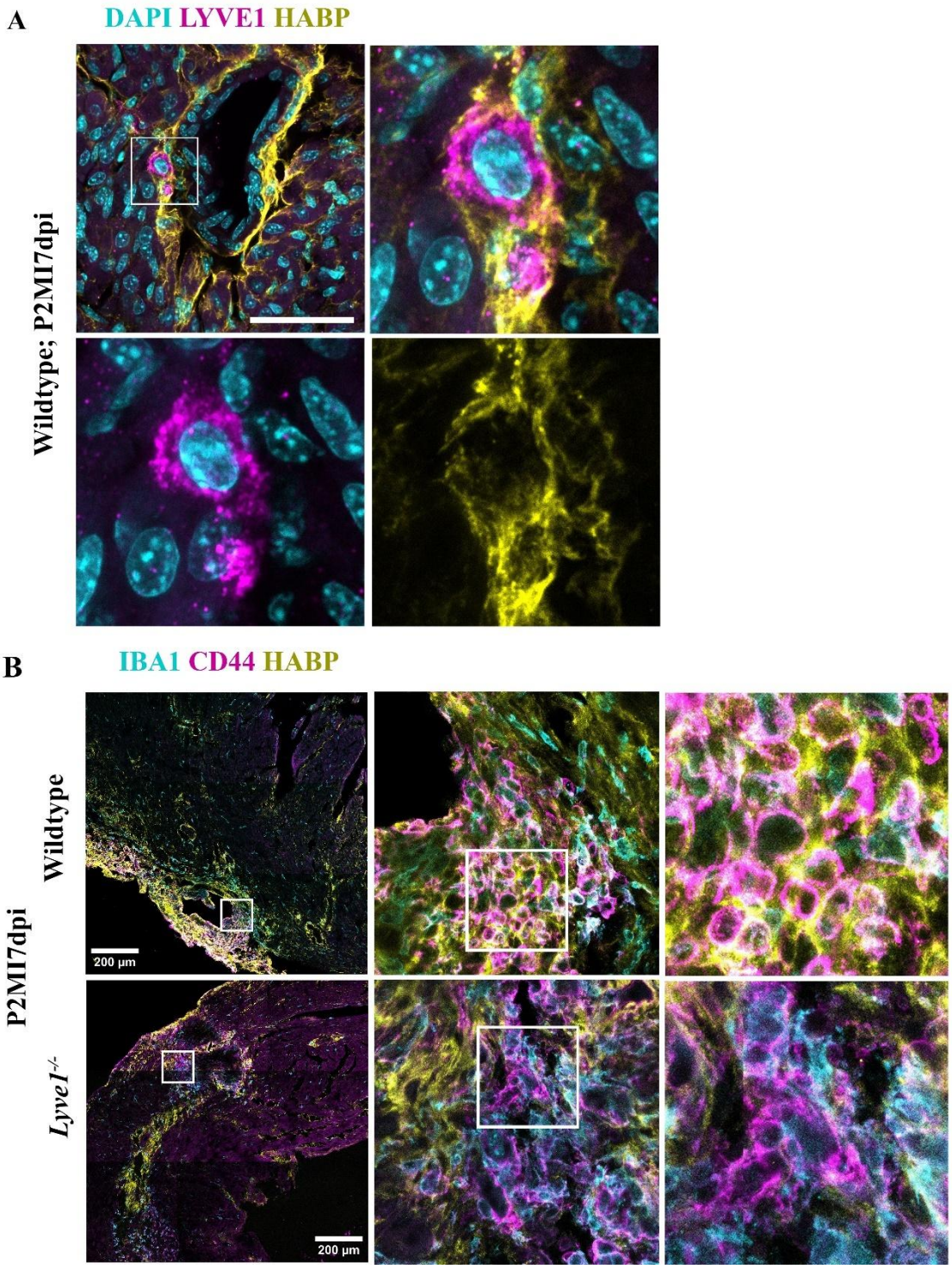

Figure 6-9. Macrophage glycocalyx visualisation.Representative LYVE-1^{+} macrophage possessing a HA glycocalyx (A). Reduced and disrupted HA glycocalyx morphology in the *Lyve1*$^{-/-}$ as compared to wildtype controls (B). Qualitative observations in A and B were repeated across the scar and in a second infarcted heart. Scale bars, 50 µm for A; 200 µm for B.

6.3.2 Investigating the expression of LYVE-1 in BMDMs

6.3.2.1 Unstimulated BMDMs do not express LYVE-1

Given that a large amount of hyaluronic acid (HA) is present throughout the infarct zone following MI, there are inherent challenges with delineating the macrophage HA glycocalyx from extracellular matrix HA. I therefore explored the possibility of examining the macrophage HA glycocalyx *in vitro* using bone marrow-derived macrophages (BMDMs). In order to obtain a model of infiltrating macrophages *in vitro*, a protocol for extracting and culturing bone-marrow derived macrophages was developed with assistance from Professor Robin Choudhury's group, University of Oxford (Figure 6-10).

A challenge to overcome with this approach is the inherent difference between BMDMs and neonatal yolk-sac derived tissue-resident macrophages. Not only do these macrophage populations arise from different tissue sources, but are known to express different genes, including *Lyve1*. When BMDMs are induced from monocytes by M-CSF in the absence of additional stimulation, they do not express LYVE-1. This was confirmed during my optimisation of the BMDM induction protocol by immunofluorescent staining (Figure 6-10).

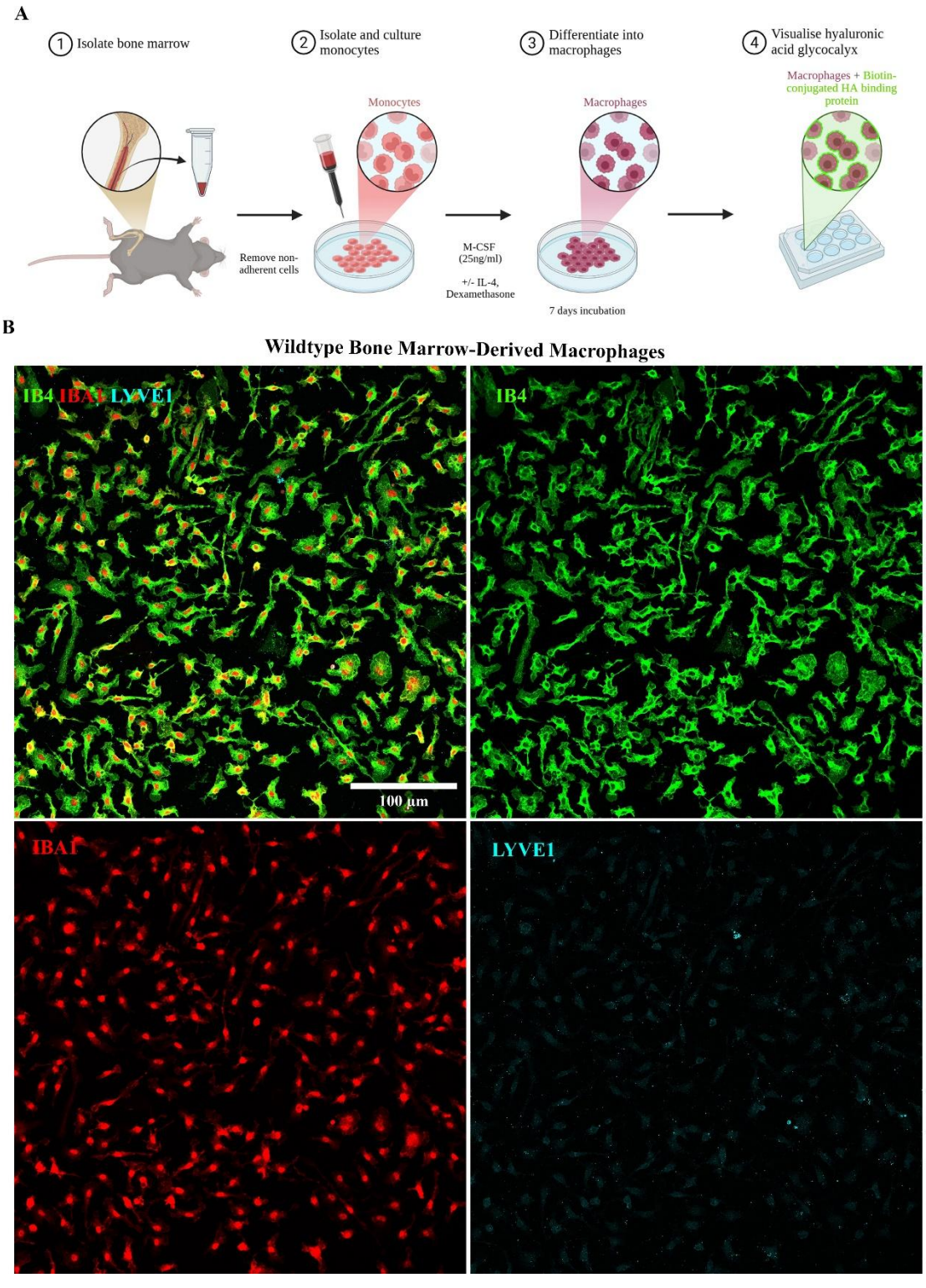

Figure 6-10. BMDM isolation and induction.BMDMs were isolated and cultured using M-CSF as previously described; bone marrow was harvested from adult wildtype mice, plated after removal of non-adherent cells, and differentiated for 7 days in M-CSF (A). BMDMs induced by M-CSF expressed macrophage markers IB4 and IBA1 but did not express LYVE-1 (B). Scale bar: 100 µm. Panel A was created using BioRender.com.

6.3.2.2 BMDM stimulation fails to induce LYVE-1 expression

Peripheral blood monocytes have been reported to express LYVE-1 on stimulation by IL-4[159], and the RAW264.7 monocyte cell line has previously been reported to express LYVE-1 following treatment with M-CSF, IL-4, and dexamethasone ('MID')[152]. Stimulation by traditionally pro-reparative factors in this manner is expected to polarise macrophages towards what is classically described as an M2 phenotype.

BMDM induction was repeated, firstly with the addition of IL-4 (Figure 6-11), and subsequently with the addition of IL-4, dexamethasone, and prostaglandin$_{E2}$ in various combinations (Figure 6-12). While visualisation of the HA glycocalyx was possible by HA binding protein (HABP) staining, induction of LYVE-1 was not possible under any condition, assessed both by immunofluorescent staining and flow cytometry. Perhaps unsurprisingly given the failure of LYVE-1 induction, there were no apparent differences in HABP morphology between wildtype and *Lyve1*$^{-/-}$ BMDMs (Figure 6-11). Furthermore, staining for the apoptotic marker CC3 was conducted to assess any potential difference in apoptosis under stimulated conditions in the *Lyve1* knockout. Again, as expected given the lack of LYVE-1 expression under stimulated conditions, there was no significant difference in CC3 expression between wildtype and *Lyve1*$^{-/-}$.

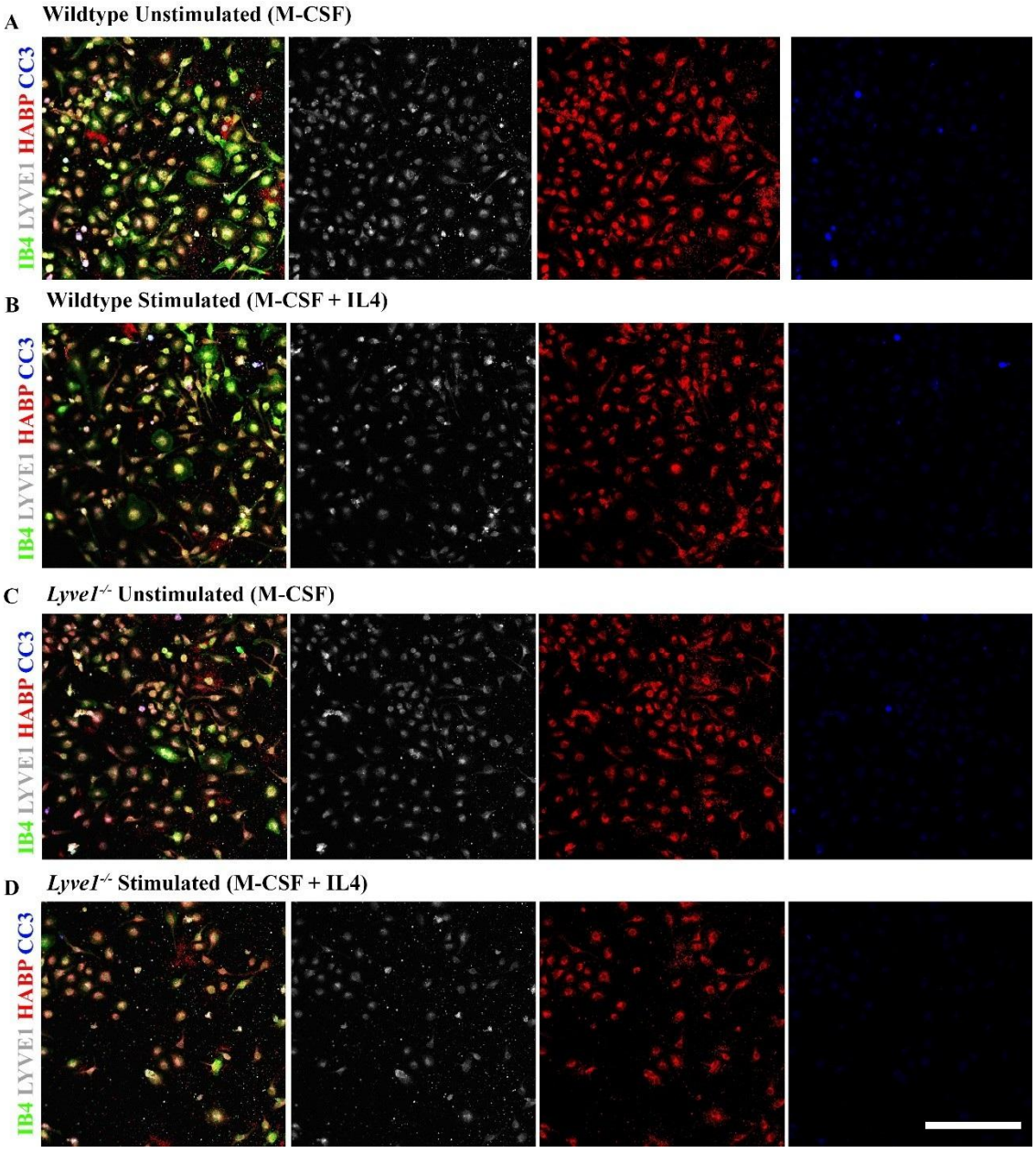

Figure 6-11. Stimulation by IL-4 fails to induce LYVE-1 expression in BMDMs.Wildtype and *Lyve1*$^{-/-}$ BMDMs were cultured in M-CSF (A, C) or M-CSF + IL-4 (B, D). Left panels are merges; single-channel images show LYVE-1 (grey), HABP (red), and cleaved caspase-3 (blue). Across all conditions, BMDMs lacked membrane-localised LYVE-1 staining; a faint diffuse signal in the LYVE-1 channel was present in both WT and *Lyve1*$^{-/-}$ cultures and was identified as non-specific antibody background by control staining. HABP identified a hyaluronan glycocalyx with no apparent change with IL-4. CC3+ cells were rare across conditions. Scale bar; 100 µm.

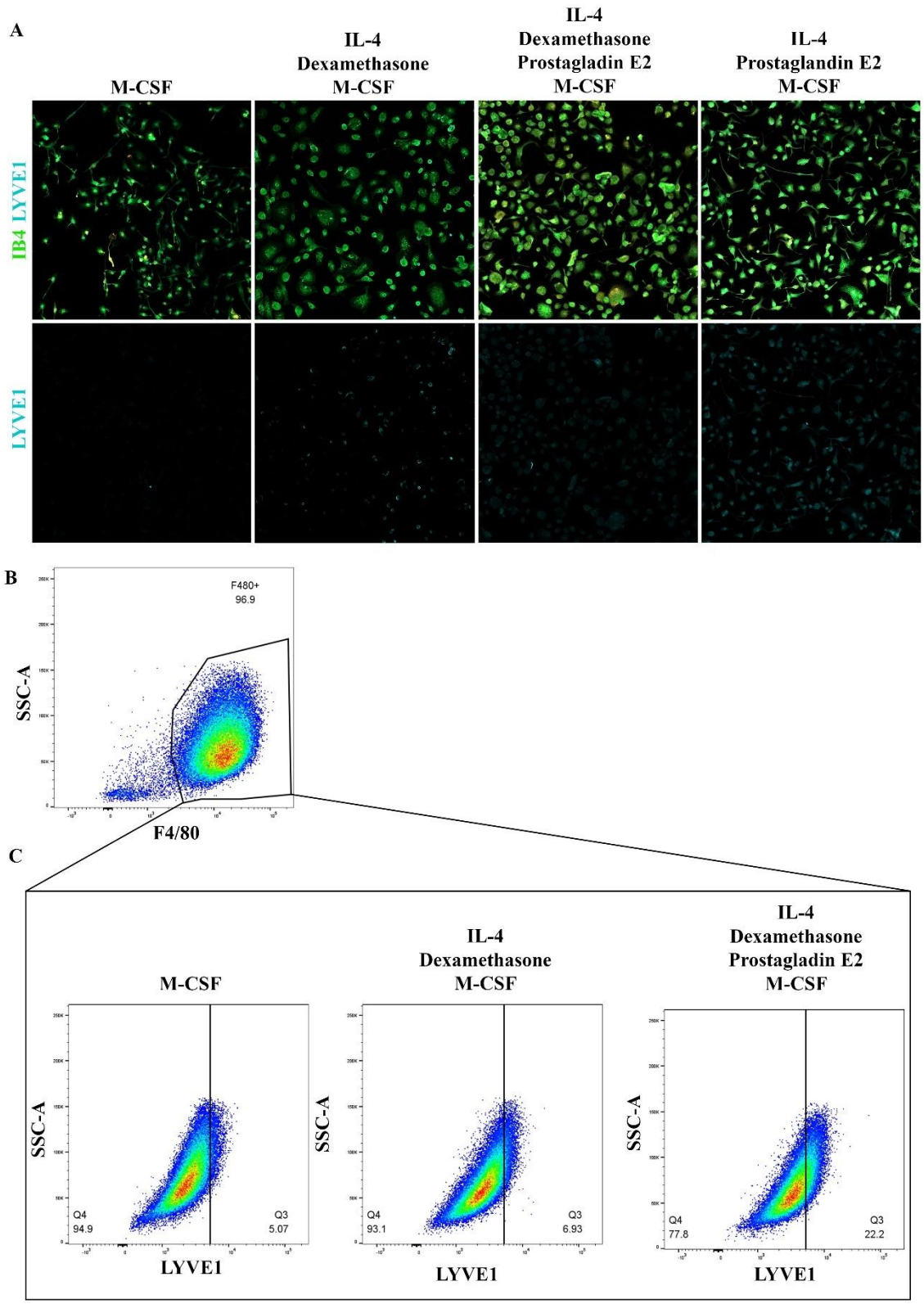

Figure 6-12. BMDM flow-cytometry and IF after IL-4, dexamethasone, PGE_2.

WT BMDMs cultured in M-CSF alone or with IL-4, IL-4 + dexamethasone, or IL-4 + dexamethasone + PGE_2; The LYVE-1 channel again shows only background staining with no

membrane localisation (A); intensity and pattern are comparable to the background seen in Fig. 6-12. Flow-cytometry gate for macrophages; F4/80$^+$ (B). LYVE-1 vs SSC-A within the F4/80$^+$ gate (C). Across conditions, apparent LYVE-1$^+$ events remain at or near background; the right-shift observed with IL-4+dexamethasone+PGE_2 likely reflects increased non-specific signal rather than true induction.

6.4 Discussion

This chapter examines differential gene expression in *Lyve1*$^{-/-}$ macrophages, highlights an increase in apoptotic programmes, and advances a working mechanism for this effect.

6.4.1 Loss of *Lyve1* results in depletion of CCR2$^-$ resident macrophages

Mechanistic insight into how *Lyve1* loss-of-function affects macrophages was provided by scRNA-seq comparing wildtype and *Lyve1* knockout CD45$^+$ cells at P2MI7dpi, which revealed significant reduction in a CCR2- tissue-resident macrophage subpopulation and corresponding elevation in a CCR2$^+$ monocyte population; with the loss of CCR2- cells associated with a significantly increased apoptotic score against a panel of established marker genes for programmed cell death. This would be predicted to impair regeneration through exacerbating inflammation and subsequent fibrosis, as per the P7 or adult response. It has previously been shown that tissue-resident CCR2- macrophages inhibit inflammatory and pro-fibrotic monocyte recruitment[76], consequently the decreased presence of the CCR2- tissue-resident macrophages explains the increased monocyte infiltration leading to a worse outcome in the knockout background.

Unbiased differential gene expression analysis confirmed that our identified CCR2$^+$/- macrophage and monocyte clusters aligned with previously reported signatures in terms of effects on angiogenesis, fibrosis, and inflammation. These gene expression profiles remained unchanged between wildtype and knockout conditions, strengthening the

likelihood that the phenotype observed in the *Lyve1* knockout is due to loss of function in CCR2- macrophages leading to increased inflammatory monocyte recruitment, rather than intrinsic changes in molecular phenotype. Importantly, the *Lyve1*$^{+}$ macrophage clusters identified in the wildtype setting are still present in the knockout background, albeit without expressing *Lyve1*. This suggests our observations in the tissue-resident macrophages are *Lyve1*-dependent, rather than via other mechanisms mediated by macrophages that are lost in the knockout background.

6.4.2 The glycocalyx and macrophage survival: implications for LYVE-1

LYVE-1 is a hyaluronan (HA) receptor. A putative mechanism as to how LYVE-1 may maintain the CCR2- macrophage population was attributed to maintenance of a hyaluronic acid (HA)-rich glycocalyx, which is known to protect cells from the exposure of apoptotic membrane cues that trigger phagocytosis[104,158]. CD44, a HA receptor and a homologue of LYVE-1, is known to anchor the HA glycocalyx in dendritic cells and certain macrophage populations[104,160].

In alveolar macrophages, a CD44-anchored HA glycocalyx is detectable *in situ* and its enzymatic removal induces apoptosis; furthermore, *Cd44* knockdown reduces macrophage numbers and predisposes to cell death[104,160]. This constitutes direct evidence that HA-CD44 engagement supports macrophage survival *in vivo*. A similar role for LYVE-1 in the context of neonatal heart regeneration appears plausible.

6.4.3 Limitations of BMDMs for studying the HA–LYVE-1 axis

Induction of LYVE-1 expression in bone marrow-derived macrophages (BMDMs) was not possible, despite what has been reported in the literature.

Unstimulated, M-CSF–derived BMDMs did not express LYVE-1. This is concordant with the distinct ontogeny and niche dependence of resident macrophages, many of which are embryo-derived and maintained by local tissue cues, whereas BMDMs are monocyte-derived cells differentiated ex vivo. Tissue environments impose enhancer programmes that specify macrophage identity and can reprogramme incoming precursors; in their absence, resident features such as LYVE-1 are not expected to appear reliably *in vitro* [75,161].

Stimulation with IL-4 alone, or in combination with dexamethasone and/or PGE_2, failed to induce LYVE-1 by immunofluorescence or flow cytometry. Reports of LYVE-1 induction by stimulation with IL-4 derive from different systems, including human peripheral blood monocytes[159] and the RAW264.7 line[152], where M-CSF with IL-4 and dexamethasone increased LYVE-1; these differences support a model in which lineage and context, rather than stimulus alone, govern LYVE-1 expression.

These observations indicate that interrogation of the HA-LYVE-1 axis should prioritise models closer to the tissue-resident state, for example hES/hiPSC-derived macrophages, or tissue-resident macrophages directly isolated from organs.

6.4.4 Other possible roles for macrophage LYVE-1

Promoting angiogenesis has been attributed to tissue-resident macrophages previously in the setting of neonatal heart regeneration[55] and our findings are consistent with this earlier study, but also identify an important and novel role for LYVE-1 in orchestrating this

response. Elsewhere, bone marrow derived LYVE-1^{+} macrophages have a proangiogenic role in adipose tissue[151], but mechanistically, whether LYVE-1 may directly upregulate angiogenic signalling in tissue-resident macrophages remains unknown. It has been reported that LYVE-1 has signalling activity and can function to sequester proangiogenic growth factors, including FGF2 and to a lesser extent PDGF and VEGF, to induce their internalisation and transduce downstream tyrosine kinase receptors and promote endothelial cell proliferation[153].

6.5 Summary

Sc-RNA-seq analysis at P2MI7dpi showed a selective loss of *Ccr2*- *Lyve1*$^{+}$ resident macrophages in *Lyve1*$^{-/-}$ neonatal hearts with a reciprocal expansion of *Ccr2*$^{+}$ monocytes/macrophages. Within the resident cluster, apoptotic markers increased and proliferative markers decreased, corroborated *in vivo* by an increased macrophage cleaved caspase 3 expression. Differentially expressed genes linked CCR2- tissue-resident macrophages to pro-angiogenic signatures and infiltrating subsets to inflammatory/fibrotic traits, aligning with the observation of reduced neovascularisation when macrophage *Lyve1* is knocked down. LYVE-1 expression was confined to the resident cluster, and HABP staining indicated a hyaluronan-rich glycocalyx on wildtype macrophages that was attenuated in the *Lyve1*$^{-/-}$ setting, supporting a role for LYVE-1 in maintaining the macrophage HA glycocalyx.

Efforts to induce LYVE-1 in bone-marrow–derived macrophages (IL-4, dexamethasone, PGE_2) were unsuccessful, possibly emphasising the importance of tissue context.

Together, the data support a model in which macrophage LYVE-1 preserves tissue-resident macrophage survival and a pro-angiogenic milieu after neonatal MI. Its loss drives tissue-resident macrophage apoptosis, replacement by $CCR2^{+}$ infiltrates, and a shift toward the inflammatory repair observed in the adult setting. The next chapter outlines my preliminary investigation into analogous mechanisms that may operate in the non-regenerative adult heart.

7 RESULTS IV: LYVE-1 KNOCKOUT IN ADULT MYOCARDIAL INFARCTION

7.1 Background

In adult mouse models of MI, enhancing lymphangiogenesis promotes resolution of inflammation and improves function. Recombinant VEGF-C (C156S) drives cardiac lymphatic growth, increases leukocyte trafficking from the infarct to mediastinal lymph nodes (MLNs), and improves ventricular remodelling and performance; critically, this immune-cell clearance requires LYVE-1 on lymphatic endothelium. Stimulation of cardiac lymphangiogenesis reduces oedema and fibrosis and preserves function after MI. Conversely, constitutive *Lyve1* knockout blocks leukocyte transit across initial lymphatics, leading to impaired clearance to MLNs, persistent inflammatory burden in the myocardium, and worsened outcomes[9].

Within this context, neutrophil persistence is notable in *Lyve1*$^{-/-}$ hearts post-MI. Neutrophil entry into afferent lymphatics is generally mediated by β2-integrins engaging ICAMs and associated signalling. These pathways do not involve LYVE-1 as a neutrophil ligand[162-164]. By contrast, LYVE-1-dependent 'transmigratory cups' are well-defined for dendritic cells which rely on a LYVE-1-dependent mechanism of transit into the lymphatics[103]. The coexistence of high neutrophil burden with retained macrophages in *Lyve1*$^{-/-}$ hearts raises the possibility that defective efferocytosis of apoptotic neutrophils contributes to persistent inflammation, alongside impaired lymphatic egress. In the adult heart post-MI, inefficient macrophage efferocytosis, for example with MerTK pathway disruption, delays resolution and leads to increased infarct area, reduced functional recovery, highlighting neutrophil clearance as a determinant of outcome[64,66,165]. This chapter establishes pilot data to inform future investigation into whether macrophage-

intrinsic LYVE-1 supports neutrophil removal during adult cardiac repair, in addition to its established role in lymphatic trafficking.

7.2 Aims

To establish whether expression of *Lyve1* by macrophages is required for effective neutrophil clearance following MI in the adult mouse.

In this final chapter, I aim to investigate a putative role for LYVE-1$^+$ macrophages in the adult response to MI. The *in vivo* consequences of macrophage specific *Lyve1* deletion in the adult heart post-MI will be assessed. (1) The mechanism by which LYVE-1 may facilitate phagocytosis will be probed by applying an unbiased scRNA-seq approach utilising wildtype versus *Lyve1*-deficient macrophages post-MI. (2) Adult *hCD68-CreERT2;Lyve*$^{fl/fl}$ mice will undergo MI, and immune populations will be assessed using FACS and immunostaining.

7.3 Results

7.3.1 A LYVE-1$^+$ macrophage subset in the adult heart following MI

Recent unpublished scRNA-seq work from the group has complemented a previously published study illustrating retention of neutrophils in the heart post-MI by predicting the presence of infiltrating LYVE-1$^+$ macrophage populations[9]. This analysis estimates the proportion of CCR2$^+$ infiltrating macrophages that express LYVE-1 to be 9%. (Figure 7-1) and demonstrates the absence of this infiltrative macrophage subset in the uninjured heart (Figure 7-1). Wider comparative analysis of CD45$^+$ populations from wildtype and *Lyve1*$^{-/-}$ adult populations was also conducted to assess broader changes in the size of these populations (Figure 7-2). This latter analysis provides a striking illustration of

retention of polymorphonuclear (PMN) cells, predominantly neutrophils, previously observed within the *Lyve1*$^{-/-}$ heart post-MI[9].

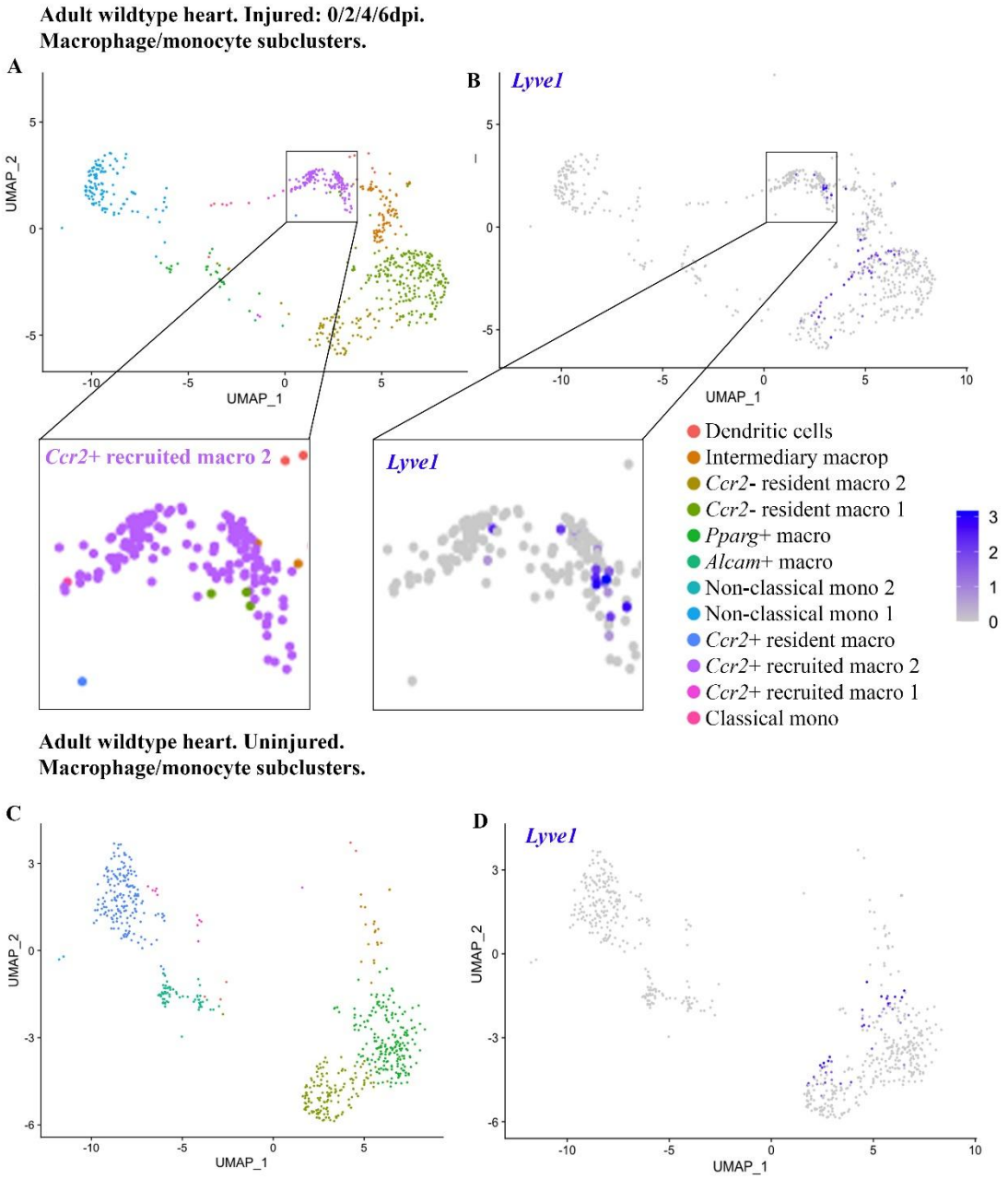

Figure 7-1. Adult heart scRNA-seq shows *Lyve1* in a macrophage subset after MI.ScRNA-seq of adult wildtype hearts was integrated across post-MI time points (0/2/4/6 dpi) and compared with uninjured controls. UMAP of post-MI myeloid cells coloured by subcluster identity, including *Ccr2*$^{+}$ recruited macro 1/2, *Ccr2*$^{-}$ resident macro 1/2, *Pparg*$^{+}$ macro, *Alcam*$^{+}$ macro, dendritic cells, and classical/non-classical monocytes (A). Feature plot of *Lyve1* expression on the same post-MI UMAP; *Lyve1* signal localises to a subset within the Ccr2^{+} recruited macrophage clusters (B; inset). UMAP of uninjured adult heart myeloid cells showing resident and monocyte

subclusters (C). Feature plot of *Lyve1* in uninjured hearts showing minimal expression and no *Lyve1*$^{+}$ *Ccr2*$^{+}$ recruited subset at steady state (D).

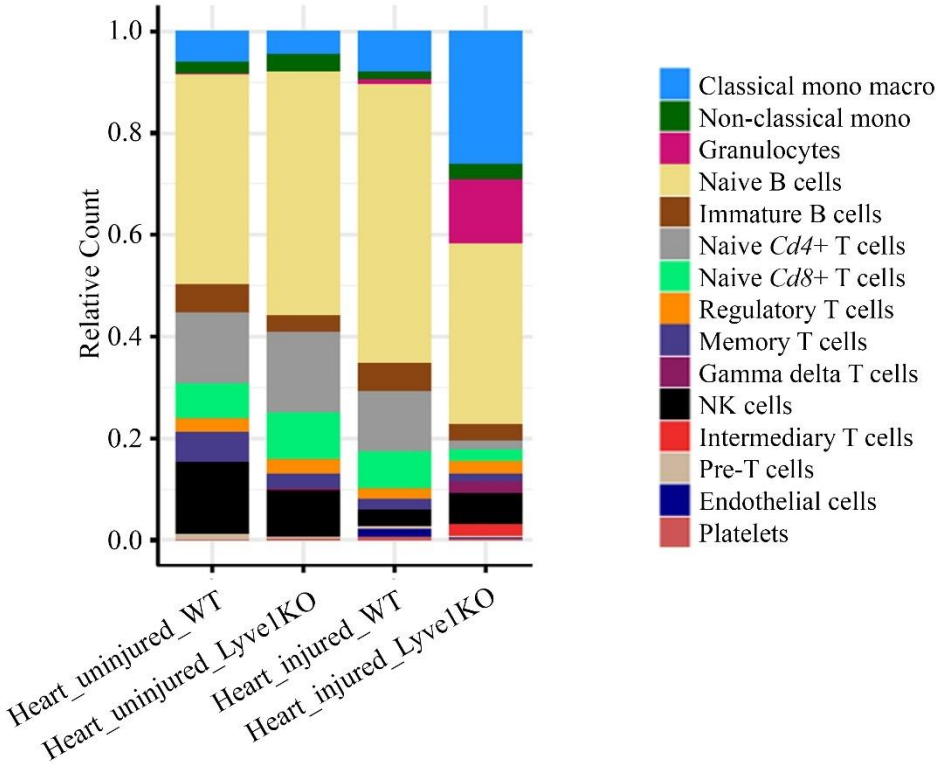

Figure 7-2. Immune cell composition in the *Lyve1*$^{-/-}$ adult heart post-MI.Stacked bars show relative proportions of scRNA-seq–derived immune populations per condition (uninjured WT, uninjured *Lyve1*$^{-/-}$, post-MI WT, post-MI *Lyve1*$^{-/-}$). Post-MI hearts show expansion of classical monocyte/macrophage compartments in both genotypes, with a further increase in *Lyve1*$^{-/-}$. The granulocyte proportion is also relatively expanded after injury in *Lyve1*$^{-/-}$.

7.3.2 Differential expression of efferocytosis-associated genes

The finding of neutrophil retention within the adult *Lyve1*$^{-/-}$ heart post-MI, reproduced in the present scRNA-seq data, is unexpected given the reported independence of neutrophil trafficking on lymphatic endothelial cell LYVE-1[105,108,162]. Other than direct transmigration into the lymphatics, the only other route of neutrophil clearance in the inflammatory response is via phagocytosis of neutrophils by macrophages (‘efferocytosis’). Prompted by the presence of LYVE-1^{+} infiltrating macrophages in the

adult heart post-MI, and considering role of LYVE-1 homologue CD44 as a receptor for phagocytosis[114], I hypothesised that loss of *Lyve1* within this population may account for reduced efferocytosis of apoptotic neutrophils by a similar mechanism.

Given the pro-survival role for macrophage LYVE-1 established in the previous chapter, loss of *Lyve1* may result in an efferocytosis deficit as a result of increased apoptosis within the LYVE-1^+ subset. Regardless of the mechanism, this hypothesis includes the assumption that LYVE-1^+ infiltrating macrophages are indispensable for efferocytosis of neutrophils.

To probe possible differences in efferocytotic capacity of macrophages, specifically the *Lyve1*$^+$ subset, in the context of *Lyve1* knockout, I identified a list of candidate genes within the scRNA-seq dataset to be investigated for differential expression between macrophage subsets and conditions. 11 genes relevant to phagocytosis were selected following a literature search on the basis of their contribution specifically to macrophage efferocytosis (Table 7-1) for comparative analysis between WT and *Lyve1*$^{-/-}$ hearts 7 days post-MI.

Differential expression analysis of efferocytosis-associated genes (Figure 7-3) revealed significant differences in *Rac1* and *Cd36* in certain macrophages subclusters between conditions (*Ccr2*$^+$ recruited macrophages, 'Non-classical monocytes 2', and *Pparg*$^+$ macrophages). Given the significant contribution of CCR2$^+$ macrophages to the infiltrative response, the potential interaction between CD36 and LYVE-1 should be considered further. It is known that glycocalyx disruption can prevent or hinder binding of *plasmodium falciparum* to CD36[166,167], raising the tentative possibility of similar

interaction hindering CD36 function in the context of *Lyve1*$^{-/-}$ as a possible avenue for further investigation. However, having established increased macrophage apoptosis as a driver of regenerative impairment in the neonate, if increased neutrophil retention is caused by loss of LYVE-1 on macrophages, it seems more likely due to macrophage apoptosis in this context.

Table 7-1. List of phagocytosis-associated genes.

Gene	**Reported Function in Phagocytosis**
Actr2	Actin assembly[168]
Ppard	Activated by LRP1-mediated efferocytosis. Induces LXR- $^{+}$ ABCA1-mediated cholesterol efflux[63]
Mfge8	Bridging molecule necessary for maximal neutrophil uptake. Potential involvement in inducing PS exposure on neutrophils[169]
Rac1	Downstream of ELMO1 $^{+}$ DOCK180[63]
Diaph1	Fc-gamma-R signalling pathway[168]
Nr1h3	Induce abca1 expression[63]
Gas6	PS-recognising bridge molecule[63]
Cd36	Receptor for apoptotic cells[168]
Stab2	Receptor for apoptotic cells. Involved in hyaluronan clearance[168]
Timd4	Receptor for apoptotic cells[168]
Rab7	Recruited by EEA1[168]
Cybb	Stabilised by PI3K to produce ROS[63]
Mertk	Downstream of bridging molecule[63]

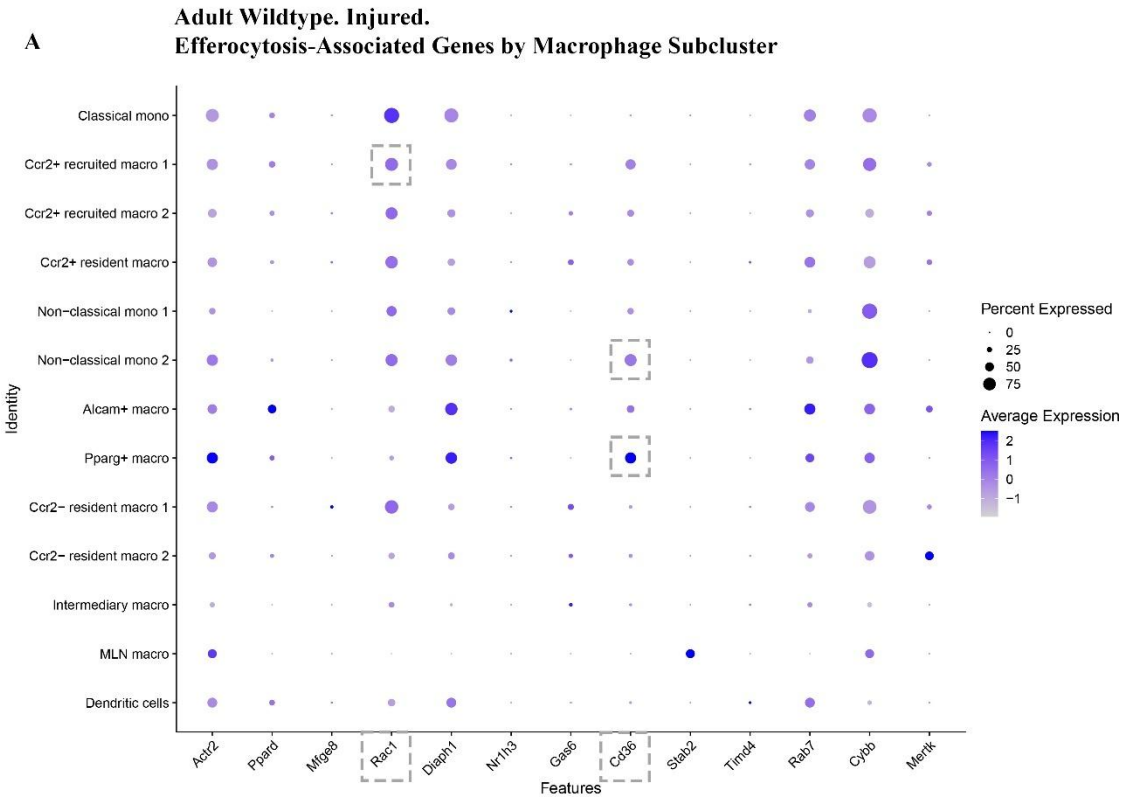
A
Adult Wildtype. Injured.
Efferocytosis-Associated Genes by Macrophage Subcluster
Classical mono
Ccr2+ recruited macro 1
Ccr2+ recruited macro 2
Ccr2+ resident macro
Non−classical mono 1
Non−classical mono 2
Alcam+ macro
Pparg+ macro
Ccr2− resident macro 1
Ccr2− resident macro 2
Intermediary macro
MLN macro
Dendritic cells
Identity
Actr2
Ppard
Mfge8
Rac1
Diaph1
Nr1h3
Gas6
Cd36
Stab2
Timd4
Rab7
Cybb
Mertk
Features
Percent Expressed
0
25
50
75
Average Expression
2
1
0
−1

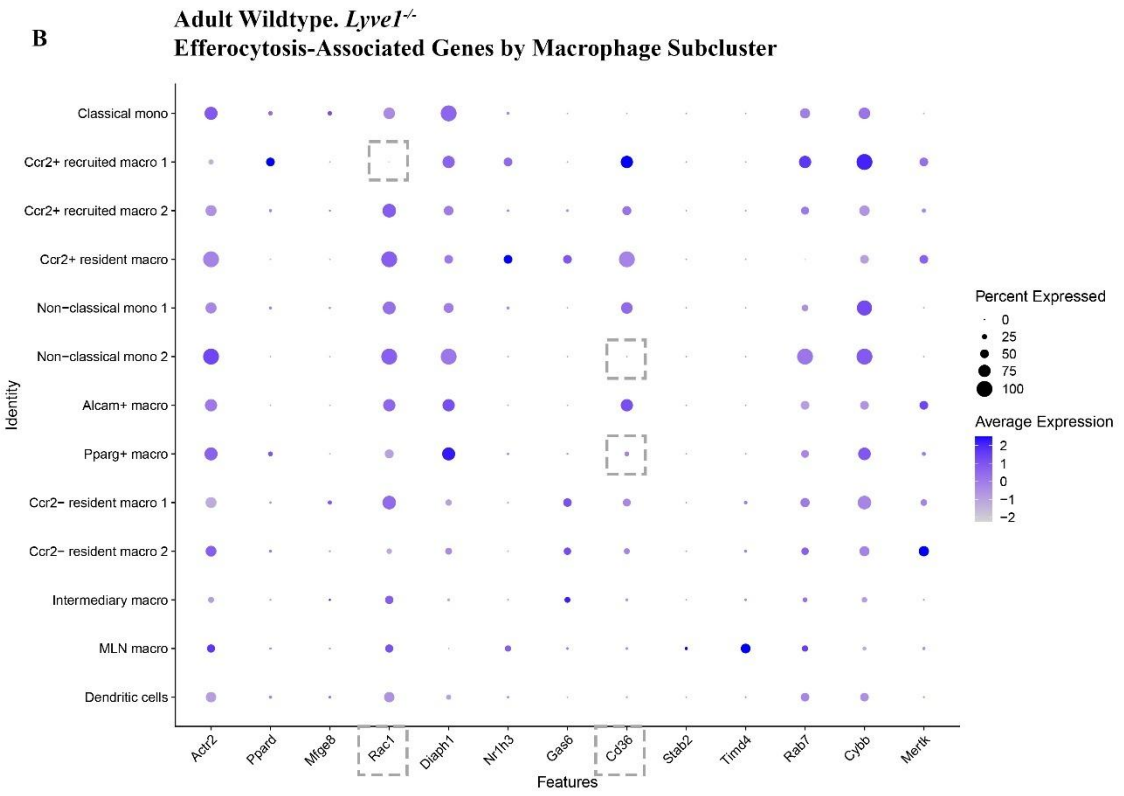
B
Adult Wildtype. Lyve1-/-
Efferocytosis-Associated Genes by Macrophage Subcluster
Classical mono
Ccr2+ recruited macro 1
Ccr2+ recruited macro 2
Ccr2+ resident macro
Non−classical mono 1
Non−classical mono 2
Alcam+ macro
Pparg+ macro
Ccr2− resident macro 1
Ccr2− resident macro 2
Intermediary macro
MLN macro
Dendritic cells
Identity
Actr2
Ppard
Mfge8
Rac1
Diaph1
Nr1h3
Gas6
Cd36
Stab2
Timd4
Rab7
Cybb
Mertk
Features
Percent Expressed
0
25
50
75
100
Average Expression
2
1
0
−1
−2

Figure 7-3. Efferocytosis-associated genes by macrophage subcluster after adult MI.

In wildtype subclusters, canonical efferocytosis receptors and adaptors are concentrated in resident-like subsets: *Mertk*/*Gas6* and *Timd4* are detectable in *Ccr2*$^{-}$ resident and *Pparg*$^{+}$ macrophages, with strong *Cd36* in the *Pparg*$^{+}$ subset; *Stab2* appears in a minority of non-classical mono 2 (A). In *Lyve1*$^{-/-}$ subclusters, expression broadens toward recruited populations: *Rac1* and *Cd36* are more frequent in *Ccr2*$^{+}$ recruited macro 1/2, while *Cd36* in *Pparg*$^{+}$ macrophages is relatively reduced; *Stab2* shows lower representation in non-classical mono 2. *Mertk*/*Gas6* levels are largely preserved across resident subsets (B). Dashed boxes mark illustrative differences; dot size denotes the percentage of cells expressing each gene; colour indicates average expression.

7.3.3 Neutrophil retention in *hCD68-CreERT2;Lyve1*$^{-/-}$ adult hearts post-MI

Given the transcriptomic differences described, I next quantified post-MI neutrophil/macrophage retention by flow cytometry in macrophage-specific *Lyve1* knockout mice. The *hCD68-CreERT2;Lyve1*$^{fl/fl}$ line with *Cre*$^{-}$ control littermate controls were used as previously in neonates. Tamoxifen was administered by gavage daily over 4 days and MI-inducing surgery was conducted on the 5th day.

Flow cytometry was conducted in *hCD68-CreERT2;Lyve1*$^{fl/fl}$ and *Cre*- control hearts at 4dpi, the timepoint associated with complete neutrophil clearance in wildtype[78] (Figure 7-4; Figure 7-5). The gating strategy was selected to closely match the original study that identified neutrophil retention in the *Lyve1*$^{-/-}$ adult heart post-MI[9] (Figure 7-4). This analysis confirmed the presence of an infiltrating LYVE-1^{+} macrophage population which was reduced in the *hCD68-CreERT2;Lyve1*$^{fl/fl}$ compared to control (Figure 7-5B).

This preliminary flow cytometry data showed evidence of an increase in Ly6G^{+} neutrophils in the knockout condition. Ly6G is highly specific for neutrophils, while eosinophils and basophils are Ly6G-negative[170]. There was also evidence of increased macrophage and neutrophil cell death within the knockout condition. This could be

explained by the same underlying mechanism proposed for the neonatal condition, which increased LYVE-1^{+} macrophage apoptosis, potentially via disruption to the HA glycocalyx, reduces the number of macrophages available for efferocytosis and clearance of dead and dying neutrophils.

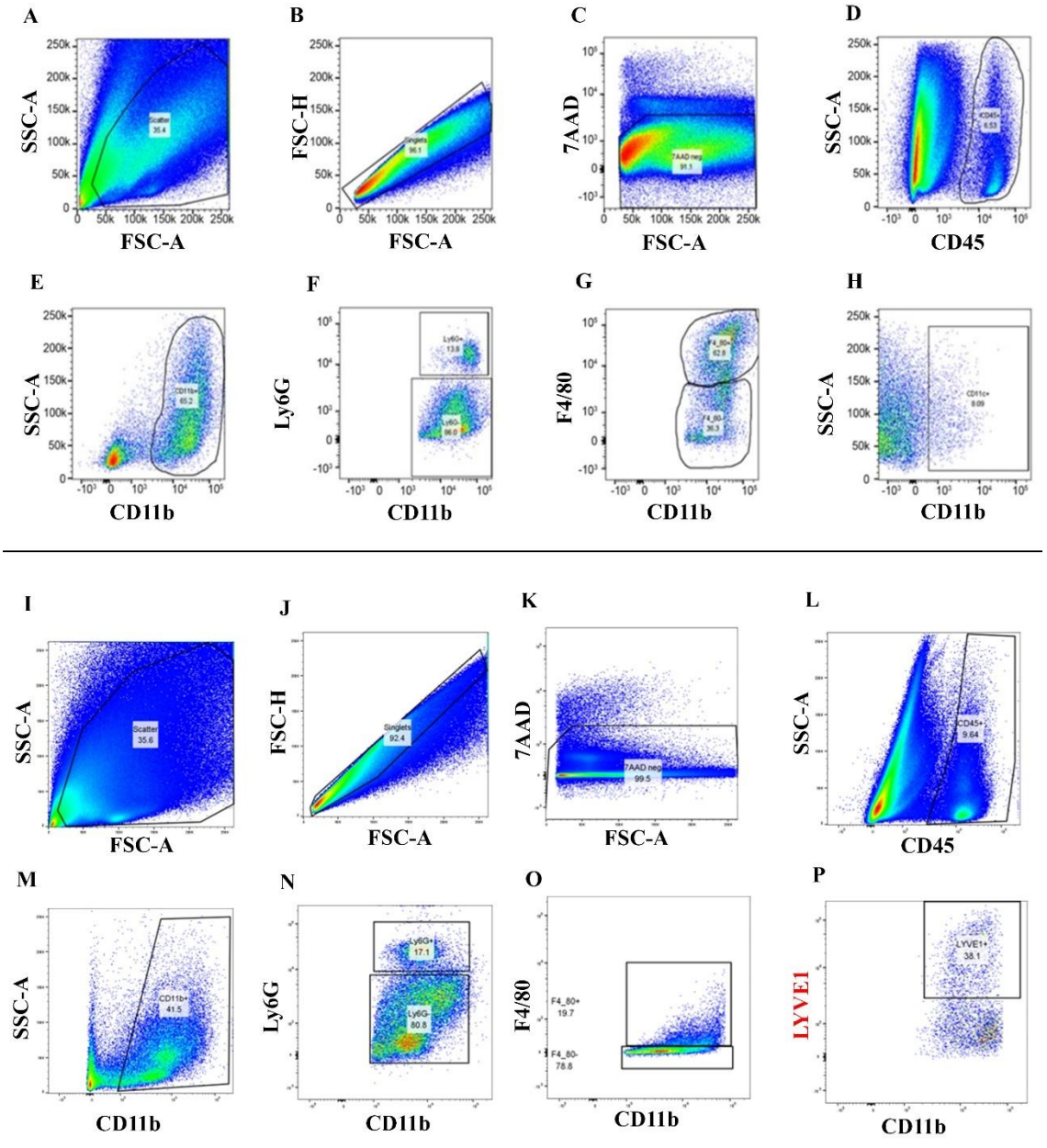

Figure 7-4. Flow cytometry panel for neutrophil and macrophage quantification.Baseline panel as used by Vieira et al.[9] (A-H). Cells were gated by size/complexity, FSC-A vs SSC-A (A); singlets, FSC-H vs FSC-A (B); and viability, 7-AAD^{-} (C). Leukocytes were selected, CD45^{+} (D); then myeloid cells, CD11b^{+} (E). Neutrophils were identified as CD11b^{+}Ly6G^{hi} (F). From the Ly6G^{-} fraction, macrophages were defined as CD11b^{+}F4/80^{+} (G); lastly, the carried-forward CD11b gate is shown (H). I adapted this panel with the addition of LYVE-1 (I-P). After gating

as in I–O (equivalent to A–G), LYVE-1 expression could be measured within CD11b^{+}F4/80^{+} macrophages (P).

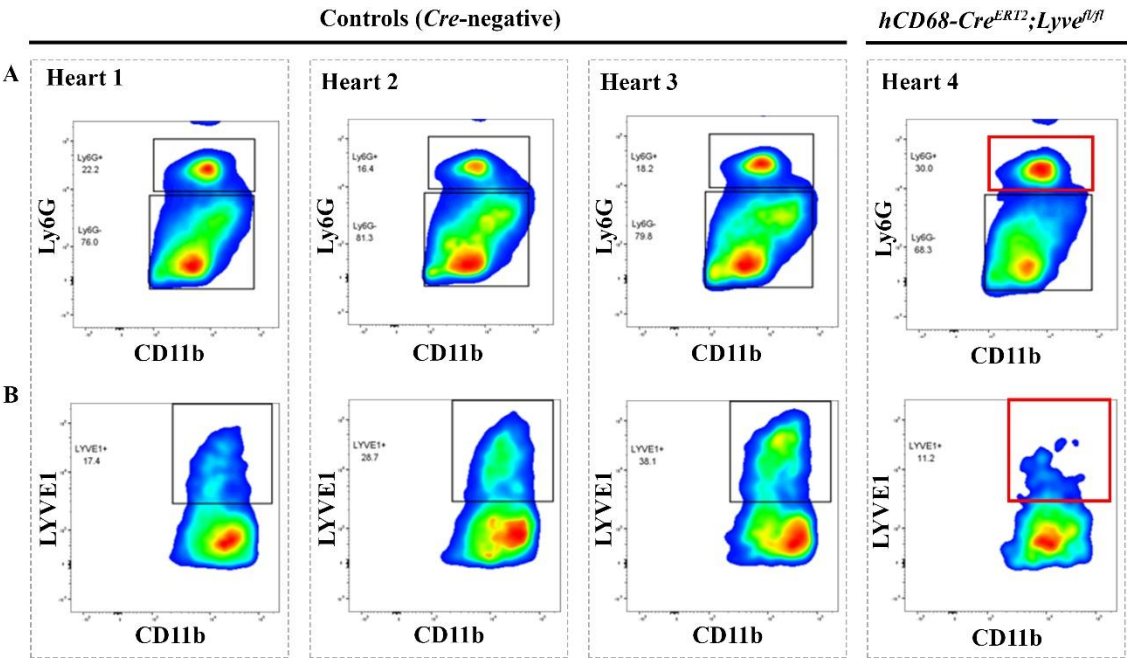

Figure 7-5. Adult neutrophils and LYVE-1^{+} macrophages: conditional KO post-MI.Representative flow-cytometry dot plots from three *Cre*$^{-}$ littermate controls (Hearts 1–3) and one *hCD68CreERT2;Lyve1*$^{fl/fl}$ heart (Heart 4). Neutrophils gated as CD11b^{+}Ly6G^{hi} (A). LYVE-1 expression within CD11b^{+} macrophages (B). Gating and thresholds follow the panel in Figure 7-4. In this small dataset (*Cre*$^{-}$ n = 3, *Cre*$^{+}$ n = 1), the Cre^{+} heart shows an apparent increase in Ly6G^{hi} neutrophils and a reduction in LYVE-1^{+} macrophages relative to controls (red boxes highlight the regions of interest). Given the sample sizes, these observations are preliminary and not interpreted statistically.

Further work to build on this preliminary data and characterise the adult response to MI in the *hCD68-CreERT2;Lyve1*$^{fl/fl}$ setting is being undertaken by a post-doctoral researcher within the group.

7.4 Discussion

The work in this chapter examines why neutrophils are retained in the *Lyve1*$^{-/-}$ adult heart after MI despite LYVE-1-independent trafficking. As their remaining route of clearance is efferocytosis by macrophages, I consider two non-exclusive possibilities: that LYVE-1 contributes directly to efferocytosis, or that, mirroring the neonatal setting, LYVE-1 supports the survival of efferocytosis-competent macrophages. Analysis of scRNA-seq data identifies candidate pathways for the involvement of LYVE-1 in efferocytosis, and the pilot flow-cytometry data informs further work into this question.

7.4.1 Neutrophil retention in the adult *Lyve1*$^{-/-}$ heart

In the adult heart, the immune landscape post-MI is markedly different than that of the neonate. In the non-injured state, the adult heart is populated by a similar yolk sac-derived CCR2^{-} macrophage subset to the neonate, but these are replaced by pro-inflammatory infiltrating monocyte-derived CCR2^{+} macrophages following MI[54,71]. This infiltration occurs in two distinct phases: an initial pro-inflammatory phase, characterised by Ly6C^{hi} monocyte infiltration between 1 and 4dpi, followed by a pro-reparative phase of Ly6C^{lo} monocyte infiltration between 4 and 8dpi[52]. A primary function of the initial phase is clearance of debris by phagocytosis, including clearance of apoptotic myocytes and neutrophils (‘efferocytosis’). Neutrophil transmigration into the lymphatics is known to be independent of LYVE-1 - consistent with their lack of a hyaluronan glycocalyx - and mediated instead by a mechanism involving integrin β2 and lipoxin[108,162]. However, increased neutrophil retention following MI is observed in mice via FACS analysis with a constitutive *Lyve1* deletion[9], which has been further supported by scRNA-seq illustrating the striking persistence of neutrophils at 7dpi. Neutrophil clearance post-MI, therefore, appears to be dependent on *Lyve1*. As such, it is possible that the predominant

route for neutrophil clearance in wildtype hearts post-MI is via efferocytosis by infiltrating macrophages in a LYVE-1-dependent manner. The retained neutrophils observed in both studies were all viable by virtue of live/dead gating during single cell sorting. Efferocytosis of viable neutrophils by macrophages is indeed possible, either by directly inducing neutrophil apoptosis, or by inducing the expression on neutrophils of pro-phagocytic "eat me" receptors[169].

7.4.2 Efferocytosis analysis

LYVE-1 is a homologue of the hyaluronan receptor CD44 and exhibits minor structural differences at the binding domain which result in a weaker binding affinity[111]. Importantly, macrophage CD44 can act as a phagocytic receptor and directly mediate phagocytosis of apoptotic cells, specifically neutrophils[157], or can act as a co-receptor by inducing inside-out activation of the integrin $\alpha_M\beta_2$ (CD11b/CD18), another efferocytosis receptor[113,114]. Differential expression analysis of 11 genes was conducted using the aforementioned scRNA-seq dataset (adult 7dpi ; *Lyve1*$^{-/-}$ versus WT) to investigate a LYVE-1 role in phagocytosis[171]. The analysis identified the genes encoding the Rho-family GTPase *Rac1* and the scavenger receptor *Cd36* to be differentially downregulated in *Lyve1*$^{-/-}$ macrophages. Intriguingly, CD44-mediated phagocytosis is dependent primarily on Rac1[114]. In this context, Rac1 is controlled by three guanine nucleotide exchange factors (GEFs) – VAV2, TIAM1, and p115 RhoGEF – that bind the cytosolic tail of CD44 when hyaluronan is bound, activating Rho kinase, inducing cytoskeletal reorganisation and facilitating phagocytic cup formation[113]. During efferocytosis, co-signalling occurs between CD44 and other phagocyte receptors: TIM4, $\alpha_v\beta_3$, calreticulin, but most interestingly the scavenger receptor CD36[113] – also downregulated in *Lyve1*$^{-/-}$ macrophages. The contribution of CD44 to phagocytosis may reflect the presence of

hyaluronan fragments within the inflammatory milieu, generated by reactive oxygen and nitrogen species that degrade hyaluronan chains within the ECM. Ligation of CD44 to these fragments is known to enhance phagocytosis and induce chemokine (CCL2, CCL3, CCL5, CXCL10) expression in macrophages[114,172], potentially in proportion to extent of ECM damage. Any contribution of HA-LYVE-1 binding to these processes is currently unknown. Just as organisation of LYVE-1 into cross-linked complexes is crucial for hyaluronan binding, CD44 receptors must be cross-linked to mediate phagocytosis of neutrophils[157,173].

Possible further investigation could examine artificial cross-linking of LYVE-1 using bivalent mAbs to enhance phagocytosis of neutrophils *in vitro*. Similarly, the addition of hyaluronan fragments may be of relevance for use in future LYVE-1+ macrophage phagocytosis assays. This depends on the ability to isolate or induce LYVE-1^{+} macrophages *in vitro*, which was not possible in my initial studies and thus future development of a robust *in vitro* system for study of LYVE-1^{+} macrophages is a necessity for this work to progress.

7.5 Summary

In this chapter I examined the role of LYVE-1 in the adult post-MI response. ScRNA-seq from wildtype and *Lyve1*$^{-/-}$ hearts at baseline and after infarction identified *Lyve1* expression within a subset of infiltrating macrophages, alongside transcriptional shifts consistent with altered phagocytic/efferocytic programmes. Together, these data imply that macrophage-intrinsic LYVE-1 may contribute to resolution after adult MI, acting in parallel with, and distinct from, the lymphatic endothelial role established in earlier work.

8 FINAL CONCLUSIONS AND FUTURE WORK

8.1 Main Findings

In Chapter 4, I demonstrate that, at P1, the cardiac lymphatic network is morphologically and functionally immature, with limited lymphangiogenesis, a predominance of "zippered" junctions, and reduced trafficking of labelled macrophages to mediastinal lymph nodes; by P7, lymphangiogenesis, "button" junctions, and macrophage clearance post-MI are evident. scRNA-seq suggested altered LEC–macrophage signalling across this window, including a stage shift in candidate lymphangiocrine pathways.

In Chapter 5, I carried out conditional tamoxifen-driven macrophage-specific deletion of *Lyve1* in neonatal mice following MI at P2 using a *hCD68-CreERT2;Lyve1*$^{fl/fl}$ line. I demonstrated that these mice exhibit impaired functional recovery and reduced neovascularisation compared to wildtype. This data recapitulated the global *Lyve1*$^{-/-}$ data, implying the effect is via a macrophage LYVE-1-dependent mechanism.

In Chapter 6, the mechanism by which LYVE-1 knockdown leads to impaired cardiac regeneration was investigated. ScRNA-seq at P2MI7dpi indicated relative depletion of *Ccr2-Lyve1*$^{+}$ tissue-resident macrophages, attributable to increased apoptosis. Subsequent imaging of tissue-resident macrophages post-MI revealed apparent morphological defects in the glycocalyx coats of *Lyve1*$^{-/-}$ macrophages. These data are consistent with a model in which glycocalyx disruption promotes macrophage apoptosis via unmasking of pro-apoptotic membrane elements, a mechanism already described in the context of *Cd44* knockout.

Finally, in Results IV, I conduct preliminary work to establish pilot data for future projects investigating the role of macrophage LYVE-1 in adult hearts post-MI. ScRNA-seq analysis of *Lyve1*$^{-/-}$ adult hearts revealed differential expression of efferocytosis-associated genes within subsets defined as *Lyve1*$^{+}$ in wildtype. Flow cytometry data shows that macrophage-specific deletion of *Lyve1* in adult mice post-MI caused increased macrophage cell death and neutrophil retention. Investigating the applicability of neonatal LYVE-1 macrophage mechanisms to the adult MI setting form a promising area of future study.

8.2 Future Work and Translational Potential

8.2.1 Maturation of lymphatic fluid transport

The findings from Chapter 3 demonstrate the lymphatics do not clear macrophages following MI at P1. A possible continuation of this study would be intravital imaging of macrophage transit into lymphatics following MI at P7, and its absence at P1. While likely technically challenging, this would provide direct evidence of impaired transmigration rather than relying on MLN macrophage numbers as a proxy measure.

The function of the lymphatics is broadly twofold, to clear immune cells and to clear tissue fluid. Investigation into the clearance of other immune cell types is an obvious area of follow-up. Similarly, the role of the lymphatics in fluid drainage following MI in the neonatal setting remains completely unexplored. This could be a particularly interesting area for future work given our observation that AQP-1 is differentially expressed in response to injury at P7, but not P1. This would require a method for quantifying post-MI oedema, and subsequent drainage of the fluid. Although T2-weighted cardiac MRI is widely used to visualise myocardial oedema in human patients after acute MI and

myocarditis[174], in neonatal mouse hearts specificity is limited by scale: the small, rapidly-beating heart imposes low spatial resolution with motion artefacts that undermine longitudinal quantification. A possible alternative route for quantification of oedema could involve injection of Evans Blue dye and subsequent histological assessment of MLNs to observe drainage of stained fluid.

8.2.2 Exploration of macrophage LYVE-1$^+$ function

The findings from Results II are based on the assumption that CCR2-LYVE-1$^+$ macrophages have a pro-regenerative effect *in vivo*. While a role in protection from apoptosis appears clear, additional direct functions of macrophage LYVE-1 cannot be precluded. Macrophage endothelial co-culture assays could be used to quantify direct angiogenic outputs from *Lyve1*$^{+/+}$ and *Lyve1*$^{-/-}$ macrophages. Given that BMDMs incompletely recapitulate the tissue-resident macrophage phenotype, macrophage derived from human embryonic stem cells (hESCs) or human induced pluripotent stem cells (hiPSCs) are preferable for these assays, reflecting a yolk-sac–like ontogeny more akin to resident populations[175]. Because LYVE-1 is a hyaluronan receptor, macrophage interactions with the ECM are a plausible additional function to consider. ECM assays comparing *Lyve1*$^{+/+}$ and *Lyve1*$^{-/-}$ macrophages, quantifying HA and type V collagen deposition and assessing fibrillogenesis, are supported by evidence that macrophage-derived collagen V directs early post-MI collagen assembly and alignment[79].

The role of macrophage *Lyve1* in the lymphangiogenic response remains unexplored. I have not pursued this line of investigation based on the following: (1) the lymphangiogenic response observed at P1MI7dpi is minimal, and trafficking is absent suggesting no contribution of LYVE-1$^+$ macrophages to either process. (2) Even at

P7MI7dpi, where an increased lymphangiogenic response is observed, the present work reveals that *Lyve1* macrophage-loss of function has no effect on functional outcome at this stage.

8.2.3 *In vitro* LYVE-1$^+$ macrophage assays

The findings from Results III could be followed up by implementation of an effective *in vitro* method of culturing LYVE-1$^+$ macrophages. The present work is limited by an inability to induce LYVE-1 expression in BMDMs. This has constrained my mechanistic investigation to *in vivo* work. Published *in vitro* induction of LYVE-1 in macrophages is limited and context-specific: upregulation has been shown in murine BMDMs only by stimulation with tumour-conditioned medium in combination with IL-4 and dexamethasone[159,176]. Mechanistic work often relies on cell lines (e.g., enforced LYVE-1 in RAW264.7[152]), whereas robust, reproducible induction in primary BMDMs under standard conditions is not established. Developing an approach for reliably isolating LYVE-1$^+$ macrophages would be invaluable for future study of this cell population. One option is fluorescence-activated cell sorting (FACS) from pooled neonatal hearts; however this relies on isolation of the LYVE-1$^+$ population by their expression of the protein, hence *Lyve1*$^{-/-}$ could not be used as a control. Alternatively, LYVE-1 function could be perturbed *in vitro* using hESC/hiPSC-derived macrophages via siRNA-mediated knockdown or blocking-antibody treatment. The *in vitro* setting would provide an opportunity to test the effect of exogenous fragmented or polymerised hyaluronan administration (i.e., LYVE-1 receptor activation), on the possible macrophage functions outlined above.

8.2.4 Macrophage LYVE-1 contribution to adult repair

The findings from Results IV could be followed up firstly by consolidating and powering the flow cytometry across early post-MI timepoints to confirm increased macrophage death and neutrophil retention, then by employing *in vitro* efferocytosis assays. Neutrophils remain a logical focus given their dual roles in injury amplification and repair, including NET formation in experimental and clinical MI[177,178]. Eosinophils and basophils also warrant targeted profiling, as eosinophils have been linked to cardioprotection after MI and basophils promote healing via IL-4/IL-13 with supportive human correlates[179-181].

8.2.5 Clinical Translation

A practical translational objective is to engineer the post-MI immune microenvironment toward a neonatal-like, pro-repair state by favouring $CCR2^-$, tissue-resident–like macrophages and curbing the influx and persistence of $CCR2^+$ monocyte-derived macrophages[76,182-184]. Prolongation of early lymphatic characteristics and attenuation of monocyte recruitment following cardiac injury may therefore extend the fibrosis-free regenerative window in neonates, with possible applications in congenital cardiac surgery.

One route is to improve lymphatic handling of oedema and inflammatory immune cells. Augmenting cardiac lymphangiogenesis, for example, via VEGF-C/VEGFR3 agonism, accelerates immune cell egress, reduces interstitial fluid, and improves function after experimental MI[9]; mechanistically, LYVE-1 at lymphatic endothelium gates leukocyte entry and thus remains relevant where macrophage-to-lymphatic transit is limiting. Such

approaches could sit alongside standard care in reperfused STEMI and in post-operative settings where tissue swelling and inflammatory load are prominent.

A complementary approach is to reduce CCR2-dependent monocyte recruitment. Proof-of-concept studies using CCR2-targeted RNA interference or nanoparticle-delivered siRNA show reduced Ly6C^{hi} influx, dampened infarct inflammation, and improved remodelling-supporting programmes that transiently suppress this axis during the inflammatory phase[185,186]. Enhancing efferocytosis offers an additional complementary route of translation. Acute blockade of the CD47–SIRPα "don't-eat-me" signal improves apoptotic cell clearance, enhances resolution, and limits infarct size post-MI[187].

Advancing a mechanistic map of the regenerative immune niche offers a possible route to improve the performance of remuscularisation strategies. Evidence that the apparent benefits of cell and patch therapies often reflect acute immunomodulation rather than durable engraftment further supports this emphasis[188]. Cardiac patches can also programme macrophage behaviour, providing a means to reinforce pro-reparative cues at the tissue interface[189]. Optimising the immune microenvironment before implantation, for example, by transiently biasing toward CCR2-negative macrophage predominance and enhancing lymphatic clearance, therefore has a clear rationale to improve graft integration and downstream outcomes.

Finally, the LYVE-1/HA axis itself remains of interest for future therapeutics: endothelial LYVE-1 mediates HA-dependent leukocyte docking and transit into lymphatics, so interventions that modulate ligand–receptor engagement (for example, by altering HA presentation or availability) could, in principle, enhance immune cell clearance where it

is rate-limiting[103,105]. While preclinical, this mechanistic footing strengthens the case for monitoring LYVE-1/HA-related biomarkers in early human studies.

8.3 Final Remarks

Taken together, these studies position the lymphatic-macrophage axis as a stage-dependent determinant of outcome after MI. In the neonatal heart, immature junctional architecture and limited lymphangiogenesis favour retention of tissue-resident, 'pro-regenerative' macrophages, and this is coupled to a requirement for macrophage LYVE-1 to support survival and effective regeneration. In the adult heart, preliminary data indicate that LYVE-1 expressed in infiltrating macrophages contributes to efferocytosis and timely clearance of neutrophils.

If therapies for inducing endogenous cardiac regeneration in the adult heart are to be feasible, the post-MI immune environment will likely need to shift towards dominance of tissue-resident macrophages. There are two tangible routes for achieving this related to the present work. (1) Promote selective lymphatic clearance of $CCR2^{+}$ monocyte-derived macrophages by the lymphatics while permitting CCR2- tissue-resident macrophages to remain within the infarct. (2) Restrict monocyte recruitment (for example via CCR2/CCL2), in combination with a temporary reduction in lymphatic macrophage trafficking, to prevent loss of the limited native tissue-resident population. These approaches would aim to reproduce key features of the neonatal setting, thereby creating conditions more permissive for endogenous regeneration.

9 BIBLIOGRAPHY

1. Khan, M.S., Shahid, I., Bennis, A., Rakisheva, A., Metra, M. & Butler, J. Global epidemiology of heart failure. *Nature Reviews Cardiology* **21**, 717–734 (2024).
2. Byrne, R.A., Rossello, X., Coughlan, J.J., Barbato, E., Berry, C., Chieffo, A., Claeys, M.J., Dan, G.-A., Dweck, M.R., Galbraith, M., Gilard, M., Hinterbuchner, L., Jankowska, E.A., Jüni, P., Kimura, T., Kunadian, V., Leosdottir, M., Lorusso, R., Pedretti, R.F.E., Rigopoulos, A.G., Rubini Gimenez, M., Thiele, H., Vranckx, P., Wassmann, S., Wenger, N.K., Ibanez, B. & Group, E.S.C.S.D. 2023 ESC Guidelines for the management of acute coronary syndromes: Developed by the task force on the management of acute coronary syndromes of the European Society of Cardiology (ESC). *European Heart Journal* **44**, 3720–3826 (2023).
3. Heidenreich, P.A., Bozkurt, B., Aguilar, D., Allen, L.A., Byun, J.J., Colvin, M.M., Deswal, A., Drazner, M.H., Dunlay, S.M., Evers, L.R., Fang, J.C., Fedson, S.E., Fonarow, G.C., Hayek, S.S., Hernandez, A.F., Khazanie, P., Kittleson, M.M., Lee, C.S., Link, M.S., Milano, C.A., Nnacheta, L.C., Sandhu, A.T., Stevenson, L.W., Vardeny, O., Vest, A.R. & Yancy, C.W. 2022 AHA/ACC/HFSA Guideline for the Management of Heart Failure: A Report of the American College of Cardiology/American Heart Association Joint Committee on Clinical Practice Guidelines. *Circulation* **145**, e895–e1032 (2022).
4. Saeed, D., Feldman, D., Banayosy, A.E., Birks, E., Blume, E., Cowger, J., Hayward, C., Jorde, U., Kremer, J., MacGowan, G., Maltais, S., Maybaum, S., Mehra, M., Shah, K.B., Mohacsi, P., Schweiger, M., Schroeder, S.E., Shah, P., Slepian, M., Tops, L.F., Alvarez, P., Arabia, F., Aslam, S., Benson-Louis, L.t., Birati, E., Buchholz, H.W., Cedars, A., Christensen, D., Ciarka, A., Coglianese, E., Cogswell, R., Cook, J., Copeland, J., Costello, J.G., Drakos, S.G., Eghtesady, P., Elliot, T., Estep, J.D., Eulert-Grehn, J.J., Fabrizio, R., Garbade, J., Gelow, J., Guglin, M., Hernandez-Montfort, J., Horstmanshof, D., John, R., Kanwar, M., Khaliel, F., Kim, G., Kumar, S., Lavee, J., Leache, M., Leprince, P., Lim, S., Loforte, A., Maly, J., Najjar, S., Netuka, I., Pamboukian, S.V., Patel, S.R., Pinney, S., Pluym, C.V., Potapov, E., Robson, D., Rochlani, Y., Russell, S., Sandau, K., Sandoval, E., Sayer, G., Schettle, S., Schibilsky, D., Schlöglhofer, T., Schmitto, J., Siddique, A., Silvestry, S., Slaughter, M.S., Sun, B., Takayama, H., Tedford, R., Teuteberg, J.J., Ton, V.K., Uriel, N., Vierecke, J., Zimpfer, D. & D'Alessandro, D. The 2023 International Society for Heart and Lung Transplantation Guidelines for Mechanical Circulatory Support: A 10- Year Update. *J Heart Lung Transplant* **42**, e1–e222 (2023).
5. Jebran, A.-F., Seidler, T., Tiburcy, M., Daskalaki, M., Kutschka, I., Fujita, B., Ensminger, S., Bremmer, F., Moussavi, A., Yang, H., Qin, X., Mißbach, S., Drummer, C., Baraki, H., Boretius, S., Hasenauer, C., Nette, T., Kowallick, J., Ritter, C.O., Lotz, J., Didié, M., Mietsch, M., Meyer, T., Kensah, G., Krüger, D., Sakib, M.S., Kaurani, L., Fischer, A., Dressel, R., Rodriguez-Polo, I., Stauske, M., Diecke, S., Maetz-Rensing, K., Gruber-Dujardin, E., Bleyer, M., Petersen, B., Roos, C., Zhang, L., Walter, L., Kaulfuß, S., Yigit, G., Wollnik, B., Levent, E., Roshani, B., Stahl-Henning, C., Ströbel, P., Legler, T., Riggert, J., Hellenkamp, K., Voigt, J.-U., Hasenfuß, G., Hinkel, R., Wu, J.C., Behr, R. & Zimmermann, W.-H. Engineered heart muscle allografts for heart repair in primates and humans. *Nature* **639**, 503–511 (2025).
6. Gao, L., Gregorich, Z.R., Zhu, W., Mattapally, S., Oduk, Y., Lou, X., Kannappan, R., Borovjagin, A.V., Walcott, G.P., Pollard, A.E., Fast, V.G., Hu, X., Lloyd, S.G., Ge, Y. & Zhang, J. Large Cardiac Muscle Patches Engineered From Human Induced-Pluripotent Stem Cell–Derived Cardiac Cells Improve Recovery From Myocardial Infarction in Swine. *Circulation* **137**, 1712–1730 (2018).
7. Bain, J.D., Barrs, R.W. & Mei, Y. Progress and challenges in transplantation of human pluripotent stem cell derived cardiomyocytes for cardiac therapy. *npj Biomedical Innovations* **3**, 2 (2026).

8. Li, R.G., Meng, F. & Martin, J.F. Targeting the Hippo Pathway for Cardiac Regeneration. *Physiology* **40**, 502–508 (2025).
9. Vieira, J.M., Norman, S., Villa Del Campo, C., Cahill, T.J., Barnette, D.N., Gunadasa-Rohling, M., Johnson, L.A., Greaves, D.R., Carr, C.A., Jackson, D.G. & Riley, P.R. The cardiac lymphatic system stimulates resolution of inflammation following myocardial infarction. *J Clin Invest* **128**, 3402–3412 (2018).
10. Koopmans, T. & van Rooij, E. Molecular gatekeepers of endogenous adult mammalian cardiomyocyte proliferation. *Nature Reviews Cardiology* (2025).
11. Derks, W. & Bergmann, O. Polyploidy in Cardiomyocytes. *Circulation Research* **126**, 552–565 (2020).
12. Li, X., Wu, F., Günther, S., Looso, M., Kuenne, C., Zhang, T., Wiesnet, M., Klatt, S., Zukunft, S., Fleming, I., Poschet, G., Wietelmann, A., Atzberger, A., Potente, M., Yuan, X. & Braun, T. Inhibition of fatty acid oxidation enables heart regeneration in adult mice. *Nature* **622**, 619–626 (2023).
13. Weinberger, M. & Riley, P.R. Animal models to study cardiac regeneration. *Nat Rev Cardiol* **21**, 89–105 (2024).
14. Lam, N.T. & Sadek, H.A. Neonatal Heart Regeneration: Comprehensive Literature Review. *Circulation* **138**, 412–423 (2018).
15. Gunadasa-Rohling, M., Masters, M., Maguire, M.L., Smart, S.C., Schneider, J.E. & Riley, P.R. Magnetic Resonance Imaging of the Regenerating Neonatal Mouse Heart. *Circulation* **138**, 2439–2441 (2018).
16. Porrello, E.R., Mahmoud, A.I., Simpson, E., Johnson, B.A., Grinsfelder, D., Canseco, D., Mammen, P.P., Rothermel, B.A., Olson, E.N. & Sadek, H.A. Regulation of neonatal and adult mammalian heart regeneration by the miR-15 family. *Proceedings of the National Academy of Sciences of the United States of America* **110**, 187–192 (2013).
17. Saker, D.M., Walsh-Sukys, M., Spector, M. & Zahka, K.G. Cardiac recovery and survival after neonatal myocardial infarction. *Pediatr Cardiol* **18**, 139–142 (1997).
18. Haubner, B.J., Schneider, J., Schweigmann, U., Schuetz, T., Dichtl, W., Velik-Salchner, C., Stein, J.I. & Penninger, J.M. Functional Recovery of a Human Neonatal Heart After Severe Myocardial Infarction. *Circ Res* **118**, 216–221 (2016).
19. Fratz, S., Hager, A., Schreiber, C., Schwaiger, M., Hess, J. & Stern, H.C. Long-term myocardial scarring after operation for anomalous left coronary artery from the pulmonary artery. *Ann Thorac Surg* **92**, 1761–1765 (2011).
20. Peng, H., Shindo, K., Donahue, R.R., Gao, E., Ahern, B.M., Levitan, B.M., Tripathi, H., Powell, D., Noor, A., Elmore, G.A., Satin, J., Seifert, A.W. & Abdel-Latif, A. Adult spiny mice (Acomys) exhibit endogenous cardiac recovery in response to myocardial infarction. *npj Regenerative Medicine* **6**, 74 (2021).
21. Koopmans, T., van Beijnum, H., Roovers, E.F., Tomasso, A., Malhotra, D., Boeter, J., Psathaki, O.E., Versteeg, D., van Rooij, E. & Bartscherer, K. Ischemic tolerance and cardiac repair in the spiny mouse (Acomys). *npj Regenerative Medicine* **6**, 78 (2021).
22. Poss, K.D., Wilson, L.G. & Keating, M.T. Heart Regeneration in Zebrafish. *Science* **298**, 2188–2190 (2002).
23. Godwin, J.W., Debuque, R., Salimova, E. & Rosenthal, N.A. Heart regeneration in the salamander relies on macrophage-mediated control of fibroblast activation and the extracellular landscape. *npj Regenerative Medicine* **2**, 22 (2017).
24. Stockdale, W.T., Lemieux, M.E., Killen, A.C., Zhao, J., Hu, Z., Riepsaame, J., Hamilton, N., Kudoh, T., Riley, P.R., van Aerle, R., Yamamoto, Y. & Mommersteeg, M.T.M. Heart Regeneration in the Mexican Cavefish. *Cell Rep* **25**, 1997–2007 e1997 (2018).
25. Bertero, A. & Murry, C.E. Hallmarks of cardiac regeneration. *Nature Reviews Cardiology* **15**, 579–580 (2018).
26. Sayers, J.R. & Riley, P.R. Heart regeneration: beyond new muscle and vessels. *Cardiovascular Research* **117**, 727–742 (2020).

27. Jopling, C., Sleep, E., Raya, M., Martí, M., Raya, A. & Izpisúa Belmonte, J.C. Zebrafish heart regeneration occurs by cardiomyocyte dedifferentiation and proliferation. *Nature* **464**, 606–609 (2010).
28. Secco, I., Backovic, A., Tomczyk, M., Mura, A., Li, G., Bortolotti, F., Vodret, S., Dal Ferro, M., Chiavacci, E., Zentilin, L., Sinagra, G., Zacchigna, S., Mano, M. & Giacca, M. Genetic tracing and topography of spontaneous and stimulated cardiac regeneration in mice. *Nature Cardiovascular Research* **4**, 397–411 (2025).
29. Xin, M., Kim, Y., Sutherland, L.B., Murakami, M., Qi, X., McAnally, J., Porrello, E.R., Mahmoud, A.I., Tan, W., Shelton, J.M., Richardson, J.A., Sadek, H.A., Bassel-Duby, R. & Olson, E.N. Hippo pathway effector Yap promotes cardiac regeneration. *Proceedings of the National Academy of Sciences* **110**, 13839–13844 (2013).
30. Heallen, T., Morikawa, Y., Leach, J., Tao, G., Willerson, J.T., Johnson, R.L. & Martin, J.F. Hippo signaling impedes adult heart regeneration. *Development* **140**, 4683–4690 (2013).
31. Chong, J.J., Yang, X., Don, C.W., Minami, E., Liu, Y.W., Weyers, J.J., Mahoney, W.M., Van Biber, B., Cook, S.M., Palpant, N.J., Gantz, J.A., Fugate, J.A., Muskheli, V., Gough, G.M., Vogel, K.W., Astley, C.A., Hotchkiss, C.E., Baldessari, A., Pabon, L., Reinecke, H., Gill, E.A., Nelson, V., Kiem, H.P., Laflamme, M.A. & Murry, C.E. Human embryonic-stem-cell-derived cardiomyocytes regenerate non-human primate hearts. *Nature* **510**, 273–277 (2014).
32. Shiba, Y., Gomibuchi, T., Seto, T., Wada, Y., Ichimura, H., Tanaka, Y., Ogasawara, T., Okada, K., Shiba, N., Sakamoto, K., Ido, D., Shiina, T., Ohkura, M., Nakai, J., Uno, N., Kazuki, Y., Oshimura, M., Minami, I. & Ikeda, U. Allogeneic transplantation of iPS cell-derived cardiomyocytes regenerates primate hearts. *Nature* **538**, 388–391 (2016).
33. Romagnuolo, R., Masoudpour, H., Porta-Sánchez, A., Qiang, B., Barry, J., Laskary, A., Qi, X., Massé, S., Magtibay, K., Kawajiri, H., Wu, J., Valdman Sadikov, T., Rothberg, J., Panchalingam, K.M., Titus, E., Li, R.-K., Zandstra, P.W., Wright, G.A., Nanthakumar, K., Ghugre, N.R., Keller, G. & Laflamme, M.A. Human Embryonic Stem Cell-Derived Cardiomyocytes Regenerate the Infarcted Pig Heart but Induce Ventricular Tachyarrhythmias. *Stem Cell Reports* **12**, 967–981 (2019).
34. Selvakumar, D., Clayton, Z.E., Prowse, A., Dingwall, S., Kim, S.K., Reyes, L., George, J., Shah, H., Chen, S., Leung, H.H.L., Hume, R.D., Tjahjadi, L., Igoor, S., Skelton, R.J.P., Hing, A., Paterson, H., Foster, S.L., Pearson, L., Wilkie, E., Marcus, A.D., Jeyaprakash, P., Wu, Z., Chiu, H.S., Ongtengco, C.F.J., Mulay, O., McArthur, J.R., Barry, T., Lu, J., Tran, V., Bennett, R., Kotake, Y., Campbell, T., Turnbull, S., Gupta, A., Nguyen, Q., Ni, G., Grieve, S.M., Palpant, N.J., Pathan, F., Kizana, E., Kumar, S., Gray, P.P. & Chong, J.J.H. Cellular heterogeneity of pluripotent stem cell-derived cardiomyocyte grafts is mechanistically linked to treatable arrhythmias. *Nature Cardiovascular Research* **3**, 145–165 (2024).
35. Ronaldson-Bouchard, K., Ma, S.P., Yeager, K., Chen, T., Song, L., Sirabella, D., Morikawa, K., Teles, D., Yazawa, M. & Vunjak-Novakovic, G. Advanced maturation of human cardiac tissue grown from pluripotent stem cells. *Nature* **556**, 239–243 (2018).
36. de Bakker, J.M., van Capelle, F.J., Janse, M.J., Tasseron, S., Vermeulen, J.T., de Jonge, N. & Lahpor, J.R. Slow conduction in the infarcted human heart. 'Zigzag' course of activation. *Circulation* **88**, 915–926 (1993).
37. Sayers, J.R., Martinez-Navarro, H., Sun, X., de Villiers, C., Sigal, S., Weinberger, M., Rodriguez, C.C., Riebel, L.L., Berg, L.A., Camps, J., Herring, N., Rodriguez, B., Sauka-Spengler, T. & Riley, P.R. Cardiac conduction system regeneration prevents arrhythmias after myocardial infarction. *Nature Cardiovascular Research* **4**, 163–179 (2025).
38. Marín-Juez, R., El-Sammak, H., Helker, C.S.M., Kamezaki, A., Mullapuli, S.T., Bibli, S.-I., Foglia, M.J., Fleming, I., Poss, K.D. & Stainier, D.Y.R. Coronary Revascularization During Heart Regeneration Is Regulated by Epicardial and Endocardial Cues and Forms a Scaffold for Cardiomyocyte Repopulation. *Developmental Cell* **51**, 503–515.e504 (2019).

39. Marín-Juez, R., Marass, M., Gauvrit, S., Rossi, A., Lai, S.-L., Materna, S.C., Black, B.L. & Stainier, D.Y.R. Fast revascularization of the injured area is essential to support zebrafish heart regeneration. *Proceedings of the National Academy of Sciences* **113**, 11237–11242 (2016).
40. Smart, N., Risebro, C.A., Melville, A.A., Moses, K., Schwartz, R.J., Chien, K.R. & Riley, P.R. Thymosin beta4 induces adult epicardial progenitor mobilization and neovascularization. *Nature* **445**, 177–182 (2007).
41. Räsänen, M., Sultan, I., Paech, J., Hemanthakumar, K.A., Yu, W., He, L., Tang, J., Sun, Y., Hlushchuk, R., Huan, X., Armstrong, E., Khoma, O.Z., Mervaala, E., Djonov, V., Betsholtz, C., Zhou, B., Kivelä, R. & Alitalo, K. VEGF-B Promotes Endocardium-Derived Coronary Vessel Development and Cardiac Regeneration. *Circulation* **143**, 65–77 (2021).
42. Sultan, I., Ramste, M., Peletier, P., Hemanthakumar, K.A., Ramanujam, D., Tirronen, A., von Wright, Y., Antila, S., Saharinen, P., Eklund, L., Mervaala, E., Ylä-Herttuala, S., Engelhardt, S., Kivelä, R. & Alitalo, K. Contribution of VEGF-B-Induced Endocardial Endothelial Cell Lineage in Physiological Versus Pathological Cardiac Hypertrophy. *Circulation Research* **134**, 1465–1482 (2024).
43. Payne, S., Gunadasa-Rohling, M., Neal, A., Redpath, A.N., Patel, J., Chouliaras, K.M., Ratnayaka, I., Smart, N. & De Val, S. Regulatory pathways governing murine coronary vessel formation are dysregulated in the injured adult heart. *Nature Communications* **10**, 3276 (2019).
44. Das, S., Goldstone, A.B., Wang, H., Farry, J., D'Amato, G., Paulsen, M.J., Eskandari, A., Hironaka, C.E., Phansalkar, R., Sharma, B., Rhee, S., Shamskhou, E.A., Agalliu, D., de Jesus Perez, V., Woo, Y.J. & Red-Horse, K. A Unique Collateral Artery Development Program Promotes Neonatal Heart Regeneration. *Cell* **176**, 1128–1142.e1118 (2019).
45. Russo, E., Teijeira, A., Vaahtomeri, K., Willrodt, A.H., Bloch, J.S., Nitschké, M., Santambrogio, L., Kerjaschki, D., Sixt, M. & Halin, C. Intralymphatic CCL21 Promotes Tissue Egress of Dendritic Cells through Afferent Lymphatic Vessels. *Cell Rep* **14**, 1723–1734 (2016).
46. Ruiz-Villalba, A., Romero, J.P., Hernández, S.C., Vilas-Zornoza, A., Fortelny, N., Castro-Labrador, L., San Martin-Uriz, P., Lorenzo-Vivas, E., García-Olloqui, P., Palacio, M., Gavira, J.J., Bastarrika, G., Janssens, S., Wu, M., Iglesias, E., Abizanda, G., de Morentin, X.M., Lasaga, M., Planell, N., Bock, C., Alignani, D., Medal, G., Prudovsky, I., Jin, Y.-R., Ryzhov, S., Yin, H., Pelacho, B., Gomez-Cabrero, D., Lindner, V., Lara-Astiaso, D. & Prósper, F. Single-Cell RNA Sequencing Analysis Reveals a Crucial Role for CTHRC1 (Collagen Triple Helix Repeat Containing 1) Cardiac Fibroblasts After Myocardial Infarction. *Circulation* **142**, 1831–1847 (2020).
47. Bassat, E., Mutlak, Y.E., Genzelinakh, A., Shadrin, I.Y., Baruch Umansky, K., Yifa, O., Kain, D., Rajchman, D., Leach, J., Riabov Bassat, D., Udi, Y., Sarig, R., Sagi, I., Martin, J.F., Bursac, N., Cohen, S. & Tzahor, E. The extracellular matrix protein agrin promotes heart regeneration in mice. *Nature* **547**, 179–184 (2017).
48. Petrey, A.C. & de la Motte, C.A. Hyaluronan, a crucial regulator of inflammation. *Front Immunol* **5**, 101 (2014).
49. Frangogiannis, N.G. The inflammatory response in myocardial injury, repair, and remodelling. *Nat Rev Cardiol* **11**, 255–265 (2014).
50. Bonafè, F., Govoni, M., Giordano, E., Caldarera, C.M., Guarnieri, C. & Muscari, C. Hyaluronan and cardiac regeneration. *Journal of Biomedical Science* **21**, 100 (2014).
51. Rienks, M., Papageorgiou, A.-P., Frangogiannis, N.G. & Heymans, S. Myocardial Extracellular Matrix. *Circulation Research* **114**, 872–888 (2014).
52. Nahrendorf, M., Swirski, F.K., Aikawa, E., Stangenberg, L., Wurdinger, T., Figueiredo, J.L., Libby, P., Weissleder, R. & Pittet, M.J. The healing myocardium sequentially mobilizes two monocyte subsets with divergent and complementary functions. *J Exp Med* **204**, 3037–3047 (2007).

53. Prabhu, S.D. & Frangogiannis, N.G. The Biological Basis for Cardiac Repair After Myocardial Infarction: From Inflammation to Fibrosis. *Circ Res* **119**, 91–112 (2016).
54. Lavine, K.J., Epelman, S., Uchida, K., Weber, K.J., Nichols, C.G., Schilling, J.D., Ornitz, D.M., Randolph, G.J. & Mann, D.L. Distinct macrophage lineages contribute to disparate patterns of cardiac recovery and remodeling in the neonatal and adult heart. *Proc Natl Acad Sci U S A* **111**, 16029–16034 (2014).
55. Aurora, A.B., Porrello, E.R., Tan, W., Mahmoud, A.I., Hill, J.A., Bassel-Duby, R., Sadek, H.A. & Olson, E.N. Macrophages are required for neonatal heart regeneration. *The Journal of clinical investigation* **124**(2014).
56. Lai, S.L., Marín-Juez, R., Moura, P.L., Kuenne, C., Lai, J.K.H., Tsedeke, A.T., Guenther, S., Looso, M. & Stainier, D.Y. Reciprocal analyses in zebrafish and medaka reveal that harnessing the immune response promotes cardiac regeneration. *Elife* **6**(2017).
57. Li, J., Yang, K.Y., Tam, R.C.Y., Chan, V.W., Lan, H.Y., Hori, S., Zhou, B. & Lui, K.O. Regulatory T-cells regulate neonatal heart regeneration by potentiating cardiomyocyte proliferation in a paracrine manner. *Theranostics* **9**, 4324–4341 (2019).
58. Tan, Y., Duan, X., Wang, B., Liu, X. & Zhan, Z. Murine neonatal cardiac B cells promote cardiomyocyte proliferation and heart regeneration. *NPJ Regen Med* **8**, 7 (2023).
59. Silvis, M.J.M., Kaffka genaamd Dengler, S.E., Odille, C.A., Mishra, M., van der Kaaij, N.P., Doevendans, P.A., Sluijter, J.P.G., de Kleijn, D.P.V., de Jager, S.C.A., Bosch, L. & van Hout, G.P.J. Damage-Associated Molecular Patterns in Myocardial Infarction and Heart Transplantation: The Road to Translational Success. *Frontiers in Immunology* **Volume 11 - 2020**(2020).
60. Dick, S.A., Macklin, J.A., Nejat, S., Momen, A., Clemente-Casares, X., Althagafi, M.G., Chen, J., Kantores, C., Hosseinzadeh, S., Aronoff, L., Wong, A., Zaman, R., Barbu, I., Besla, R., Lavine, K.J., Razani, B., Ginhoux, F., Husain, M., Cybulsky, M.I., Robbins, C.S. & Epelman, S. Self-renewing resident cardiac macrophages limit adverse remodeling following myocardial infarction. *Nat Immunol* **20**, 29–39 (2019).
61. Dick, S.A., Wong, A., Hamidzada, H., Nejat, S., Nechanitzky, R., Vohra, S., Mueller, B., Zaman, R., Kantores, C., Aronoff, L., Momen, A., Nechanitzky, D., Li, W.Y., Ramachandran, P., Crome, S.Q., Becher, B., Cybulsky, M.I., Billia, F., Keshavjee, S., Mital, S., Robbins, C.S., Mak, T.W. & Epelman, S. Three tissue resident macrophage subsets coexist across organs with conserved origins and life cycles. *Sci Immunol* **7**, eabf7777 (2022).
62. van Amerongen, M.J., Harmsen, M.C., van Rooijen, N., Petersen, A.H. & van Luyn, M.J. Macrophage depletion impairs wound healing and increases left ventricular remodeling after myocardial injury in mice. *Am J Pathol* **170**, 818–829 (2007).
63. Doran, A.C., Yurdagul, A., Jr. & Tabas, I. Efferocytosis in health and disease. *Nat Rev Immunol* **20**, 254–267 (2020).
64. Wan, E., Yeap, X.Y., Dehn, S., Terry, R., Novak, M., Zhang, S., Iwata, S., Han, X., Homma, S., Drosatos, K., Lomasney, J., Engman, D.M., Miller, S.D., Vaughan, D.E., Morrow, J.P., Kishore, R. & Thorp, E.B. Enhanced efferocytosis of apoptotic cardiomyocytes through myeloid-epithelial-reproductive tyrosine kinase links acute inflammation resolution to cardiac repair after infarction. *Circ Res* **113**, 1004–1012 (2013).
65. Schilperoort, M., Ngai, D., Sukka, S.R., Avrampou, K., Shi, H. & Tabas, I. The role of efferocytosis-fueled macrophage metabolism in the resolution of inflammation. *Immunol Rev* **319**, 65–80 (2023).
66. DeBerge, M., Yeap, X.Y., Dehn, S., Zhang, S., Grigoryeva, L., Misener, S., Procissi, D., Zhou, X., Lee, D.C., Muller, W.A., Luo, X., Rothlin, C., Tabas, I. & Thorp, E.B. MerTK Cleavage on Resident Cardiac Macrophages Compromises Repair After Myocardial Ischemia Reperfusion Injury. *Circ Res* **121**, 930–940 (2017).
67. Rurik, J.G., Aghajanian, H. & Epstein, J.A. Immune Cells and Immunotherapy for Cardiac Injury and Repair. *Circ Res* **128**, 1766–1779 (2021).

68. Grune, J., Lewis, A.J.M., Yamazoe, M., Hulsmans, M., Rohde, D., Xiao, L., Zhang, S., Ott, C., Calcagno, D.M., Zhou, Y., Timm, K., Shanmuganathan, M., Pulous, F.E., Schloss, M.J., Foy, B.H., Capen, D., Vinegoni, C., Wojtkiewicz, G.R., Iwamoto, Y., Grune, T., Brown, D., Higgins, J., Ferreira, V.M., Herring, N., Channon, K.M., Neubauer, S., Sosnovik, D.E., Milan, D.J., Swirski, F.K., King, K.R., Aguirre, A.D., Ellinor, P.T., Nahrendorf, M. & Oxford Acute Myocardial Infarction, S. Neutrophils incite and macrophages avert electrical storm after myocardial infarction. *Nature Cardiovascular Research* **1**, 649–664 (2022).
69. Houssari, M., Dumesnil, A., Tardif, V., Kivela, R., Pizzinat, N., Boukhalfa, I., Godefroy, D., Schapman, D., Hemanthakumar, K.A., Bizou, M., Henry, J.P., Renet, S., Riou, G., Rondeaux, J., Anouar, Y., Adriouch, S., Fraineau, S., Alitalo, K., Richard, V., Mulder, P. & Brakenhielm, E. Lymphatic and Immune Cell Cross-Talk Regulates Cardiac Recovery After Experimental Myocardial Infarction. *Arteriosclerosis, thrombosis, and vascular biology*, ATVBAHA120314370 (2020).
70. Wang, Z., Cui, M., Shah, A.M., Ye, W., Tan, W., Min, Y.L., Botten, G.A., Shelton, J.M., Liu, N., Bassel-Duby, R. & Olson, E.N. Mechanistic basis of neonatal heart regeneration revealed by transcriptome and histone modification profiling. *Proc Natl Acad Sci U S A* **116**, 18455–18465 (2019).
71. Molawi, K., Wolf, Y., Kandalla, P.K., Favret, J., Hagemeyer, N., Frenzel, K., Pinto, A.R., Klapproth, K., Henri, S., Malissen, B., Rodewald, H.R., Rosenthal, N.A., Bajenoff, M., Prinz, M., Jung, S. & Sieweke, M.H. Progressive replacement of embryo-derived cardiac macrophages with age. *J Exp Med* **211**, 2151–2158 (2014).
72. Simões, F.C. & Riley, P.R. Immune cells in cardiac repair and regeneration. *Development* **149**(2022).
73. Li, Y., Du, J., Deng, S., Liu, B., Jing, X., Yan, Y., Liu, Y., Wang, J., Zhou, X. & She, Q. The molecular mechanisms of cardiac development and related diseases. *Signal Transduction and Targeted Therapy* **9**, 368 (2024).
74. Revelo, X.S., Parthiban, P., Chen, C., Barrow, F., Fredrickson, G., Wang, H., Yücel, D., Herman, A. & van Berlo, J.H. Cardiac Resident Macrophages Prevent Fibrosis and Stimulate Angiogenesis. *Circulation Research* **129**, 1086–1101 (2021).
75. Epelman, S., Lavine, K.J., Beaudin, A.E., Sojka, D.K., Carrero, J.A., Calderon, B., Brija, T., Gautier, E.L., Ivanov, S., Satpathy, A.T., Schilling, J.D., Schwendener, R., Sergin, I., Razani, B., Forsberg, E.C., Yokoyama, W.M., Unanue, E.R., Colonna, M., Randolph, G.J. & Mann, D.L. Embryonic and adult-derived resident cardiac macrophages are maintained through distinct mechanisms at steady state and during inflammation. *Immunity* **40**, 91–104 (2014).
76. Bajpai, G., Bredemeyer, A., Li, W., Zaitsev, K., Koenig, A.L., Lokshina, I., Mohan, J., Ivey, B., Hsiao, H.M., Weinheimer, C., Kovacs, A., Epelman, S., Artyomov, M., Kreisel, D. & Lavine, K.J. Tissue Resident CCR2- and CCR2+ Cardiac Macrophages Differentially Orchestrate Monocyte Recruitment and Fate Specification Following Myocardial Injury. *Circ Res* **124**, 263–278 (2019).
77. Du Cheyne, C., Tay, H. & De Spiegelaere, W. The complex TIE between macrophages and angiogenesis. *Anat Histol Embryol* **49**, 585–596 (2020).
78. Simões, F.C., Cahill, T.J., Kenyon, A., Gavriouchkina, D., Vieira, J.M., Sun, X., Pezzolla, D., Ravaud, C., Masmanian, E., Weinberger, M., Mayes, S., Lemieux, M.E., Barnette, D.N., Gunadasa-Rohling, M., Williams, R.M., Greaves, D.R., Trinh, L.A., Fraser, S.E., Dallas, S.L., Choudhury, R.P., Sauka-Spengler, T. & Riley, P.R. Macrophages directly contribute collagen to scar formation during zebrafish heart regeneration and mouse heart repair. *Nat Commun* **11**, 600 (2020).
79. Sun, X., Sigal, S., Cosma, M.-A., de Villiers, C., Weinberger, M. & Riley, P.R. Type V collagen from macrophages regulates initial collagen assembly and alignment in post-infarcted hearts. *npj Regenerative Medicine* **10**, 44 (2025).

80. Klotz, L., Norman, S., Vieira, J.M., Masters, M., Rohling, M., Dube, K.N., Bollini, S., Matsuzaki, F., Carr, C.A. & Riley, P.R. Cardiac lymphatics are heterogeneous in origin and respond to injury. *Nature* **522**, 62–67 (2015).
81. Henri, O., Pouehe, C., Houssari, M., Galas, L., Nicol, L., Edwards-Levy, F., Henry, J.P., Dumesnil, A., Boukhalfa, I., Banquet, S., Schapman, D., Thuillez, C., Richard, V., Mulder, P. & Brakenhielm, E. Selective Stimulation of Cardiac Lymphangiogenesis Reduces Myocardial Edema and Fibrosis Leading to Improved Cardiac Function Following Myocardial Infarction. *Circulation* **133**, 1484–1497 (2016).
82. Zhou, Y., Huang, C., Hu, Y., Xu, Q. & Hu, X. Lymphatics in Cardiovascular Disease. *Arterioscler Thromb Vasc Biol* **40**, e275–e283 (2020).
83. Baluk, P., Fuxe, J., Hashizume, H., Romano, T., Lashnits, E., Butz, S., Vestweber, D., Corada, M., Molendini, C., Dejana, E. & McDonald, D.M. Functionally specialized junctions between endothelial cells of lymphatic vessels. *J Exp Med* **204**, 2349–2362 (2007).
84. Baluk, P. & McDonald, D.M. Buttons and Zippers: Endothelial Junctions in Lymphatic Vessels. *Cold Spring Harb Perspect Med* **12**(2022).
85. Srinivasan, R.S., Dillard, M.E., Lagutin, O.V., Lin, F.J., Tsai, S., Tsai, M.J., Samokhvalov, I.M. & Oliver, G. Lineage tracing demonstrates the venous origin of the mammalian lymphatic vasculature. *Genes Dev* **21**, 2422–2432 (2007).
86. Martinez-Corral, I., Ulvmar, M.H., Stanczuk, L., Tatin, F., Kizhatil, K., John, S.W.M., Alitalo, K., Ortega, S. & Makinen, T. Nonvenous Origin of Dermal Lymphatic Vasculature. *Circulation Research* **116**, 1649–1654 (2015).
87. Gancz, D., Raftrey, B.C., Perlmoter, G., Marin-Juez, R., Semo, J., Matsuoka, R.L., Karra, R., Raviv, H., Moshe, N., Addadi, Y., Golani, O., Poss, K.D., Red-Horse, K., Stainier, D.Y. & Yaniv, K. Distinct origins and molecular mechanisms contribute to lymphatic formation during cardiac growth and regeneration. *Elife* **8**(2019).
88. Klaourakis, K., Vieira, J.M. & Riley, P.R. The evolving cardiac lymphatic vasculature in development, repair and regeneration. *Nat Rev Cardiol* **18**, 368–379 (2021).
89. Stone, O.A. & Stainier, D.Y.R. Paraxial Mesoderm Is the Major Source of Lymphatic Endothelium. *Dev Cell* **50**, 247–255.e243 (2019).
90. Lupu, I.E., Grainger, D.E., Kirschnick, N., Weischer, S., Zhao, E., Martinez-Corral, I., Schoofs, H., Vanhollebeke, M., Jones, G., Godwin, J., Forrow, A., Lahmann, I., Riley, P.R., Zobel, T., Alitalo, K., Mäkinen, T., Kiefer, F. & Stone, O.A. Direct specification of lymphatic endothelium from mesenchymal progenitors. *Nat Cardiovasc Res* **4**, 45–63 (2025).
91. Maruyama, K., Miyagawa-Tomita, S., Haneda, Y., Kida, M., Matsuzaki, F., Imanaka-Yoshida, K. & Kurihara, H. The cardiopharyngeal mesoderm contributes to lymphatic vessel development in mouse. *eLife* **11**, e81515 (2022).
92. Chen, H.I., Sharma, B., Akerberg, B.N., Numi, H.J., Kivelä, R., Saharinen, P., Aghajanian, H., McKay, A.S., Bogard, P.E., Chang, A.H., Jacobs, A.H., Epstein, J.A., Stankunas, K., Alitalo, K. & Red-Horse, K. The sinus venosus contributes to coronary vasculature through VEGFC-stimulated angiogenesis. *Development* **141**, 4500–4512 (2014).
93. Kataru, R.P., Jung, K., Jang, C., Yang, H., Schwendener, R.A., Baik, J.E., Han, S.H., Alitalo, K. & Koh, G.Y. Critical role of CD11b+ macrophages and VEGF in inflammatory lymphangiogenesis, antigen clearance, and inflammation resolution. *Blood* **113**, 5650–5659 (2009).
94. Glinton, K.E., Ma, W., Lantz, C., Grigoryeva, L.S., DeBerge, M., Liu, X., Febbraio, M., Kahn, M., Oliver, G. & Thorp, E.B. Macrophage-produced VEGFC is induced by efferocytosis to ameliorate cardiac injury and inflammation. *J Clin Invest* **132**(2022).
95. Pflicke, H. & Sixt, M. Preformed portals facilitate dendritic cell entry into afferent lymphatic vessels. *J Exp Med* **206**, 2925–2935 (2009).

96. Yao, L.C., Baluk, P., Srinivasan, R.S., Oliver, G. & McDonald, D.M. Plasticity of button-like junctions in the endothelium of airway lymphatics in development and inflammation. *Am J Pathol* **180**, 2561–2575 (2012).
97. Zhang, F., Zarkada, G., Han, J., Li, J., Dubrac, A., Ola, R., Genet, G., Boyé, K., Michon, P., Künzel, S.E., Camporez, J.P., Singh, A.K., Fong, G.H., Simons, M., Tso, P., Fernández-Hernando, C., Shulman, G.I., Sessa, W.C. & Eichmann, A. Lacteal junction zippering protects against diet-induced obesity. *Science* **361**, 599–603 (2018).
98. Jannaway, M., Iyer, D., Mastrogiacomo, D.M., Li, K., Sung, D.C., Yang, Y., Kahn, M.L. & Scallan, J.P. VEGFR3 is required for button junction formation in lymphatic vessels. *Cell Rep* **42**, 112777 (2023).
99. Schoofs, H., Daubel, N., Schnabellehner, S., Grönloh, M.L.B., Palacios Martínez, S., Halme, A., Marks, A.M., Jeansson, M., Barcos, S., Brakebusch, C., Benedito, R., Engelhardt, B., Vestweber, D., Gaengel, K., Linsenmeier, F., Schürmann, S., Saharinen, P., van Buul, J.D., Friedrich, O., Smith, R.S., Majda, M. & Mäkinen, T. Dynamic cytoskeletal regulation of cell shape supports resilience of lymphatic endothelium. *Nature* **641**, 465–475 (2025).
100. Flaht-Zabost, A., Gula, G., Ciszek, B., Czarnowska, E., Jankowska-Steifer, E., Madej, M., Niderla-Bielińska, J., Radomska-Leśniewska, D. & Ratajska, A. Cardiac mouse lymphatics: developmental and anatomical update. *Anat Rec (Hoboken)* **297**, 1115–1130 (2014).
101. Klaourakis, K. University of Oxford (2021).
102. Jackson, D.G. Hyaluronan in the lymphatics: The key role of the hyaluronan receptor LYVE-1 in leucocyte trafficking. *Matrix Biol* **78-79**, 219–235 (2019).
103. Johnson, L.A., Banerji, S., Lawrance, W., Gileadi, U., Prota, G., Holder, K.A., Roshorm, Y.M., Hanke, T., Cerundolo, V., Gale, N.W. & Jackson, D.G. Dendritic cells enter lymph vessels by hyaluronan-mediated docking to the endothelial receptor LYVE-1. *Nature Immunology* **18**, 762–770 (2017).
104. Johnson, L.A., Banerji, S., Lagerholm, B.C. & Jackson, D.G. Dendritic cell entry to lymphatic capillaries is orchestrated by CD44 and the hyaluronan glycocalyx. *Life Sci Alliance* **4**(2021).
105. Johnson, L.A. & Jackson, D.G. Hyaluronan and Its Receptors: Key Mediators of Immune Cell Entry and Trafficking in the Lymphatic System. *Cells* **10**, 2061 (2021).
106. Lawrance, W., Banerji, S., Day, A.J., Bhattacharjee, S. & Jackson, D.G. Binding of Hyaluronan to the Native Lymphatic Vessel Endothelial Receptor LYVE-1 Is Critically Dependent on Receptor Clustering and Hyaluronan Organization. *The Journal of biological chemistry* **291**, 8014–8030 (2016).
107. Bano, F., Banerji, S., Ni, T., Green, D.E., Cook, K.R., Manfield, I.W., DeAngelis, P.L., Paci, E., Lepšík, M., Gilbert, R.J.C., Richter, R.P. & Jackson, D.G. Structure and unusual binding mechanism of the hyaluronan receptor LYVE-1 mediating leucocyte entry to lymphatics. *Nature Communications* **16**, 2754 (2025).
108. Rigby, D.A., Ferguson, D.J., Johnson, L.A. & Jackson, D.G. Neutrophils rapidly transit inflamed lymphatic vessel endothelium via integrin-dependent proteolysis and lipoxin-induced junctional retraction. *J Leukoc Biol* **98**, 897–912 (2015).
109. Chakarov, S., Lim, H.Y., Tan, L., Lim, S.Y., See, P., Lum, J., Zhang, X.-M., Foo, S., Nakamizo, S., Duan, K., Kong, W.T., Gentek, R., Balachander, A., Carbajo, D., Bleriot, C., Malleret, B., Tam, J.K.C., Baig, S., Shabeer, M., Toh, S.-A.E.S., Schlitzer, A., Larbi, A., Marichal, T., Malissen, B., Chen, J., Poidinger, M., Kabashima, K., Bajenoff, M., Ng, L.G., Angeli, V. & Ginhoux, F. Two distinct interstitial macrophage populations coexist across tissues in specific subtissular niches. *Science* **363**, eaau0964 (2019).
110. Siret, C., van Lessen, M., Bavais, J., Jeong, H.W., Reddy Samawar, S.K., Kapupara, K., Wang, S., Simic, M., de Fabritus, L., Tchoghandjian, A., Fallet, M., Huang, H., Sarrazin, S., Sieweke, M.H., Stumm, R., Sorokin, L., Adams, R.H., Schulte-Merker, S., Kiefer, F. & van de Pavert, S.A. Deciphering the heterogeneity of the Lyve1+ perivascular macrophages in the mouse brain. *Nature Communications* **13**, 7366 (2022).

111. Banerji, S., Hide, B.R., James, J.R., Noble, M.E. & Jackson, D.G. Distinctive properties of the hyaluronan-binding domain in the lymphatic endothelial receptor Lyve-1 and their implications for receptor function. *J Biol Chem* **285**, 10724–10735 (2010).
112. Banerji, S., Ni, J., Wang, S.X., Clasper, S., Su, J., Tammi, R., Jones, M. & Jackson, D.G. LYVE-1, a new homologue of the CD44 glycoprotein, is a lymph-specific receptor for hyaluronan. *J Cell Biol* **144**, 789–801 (1999).
113. Vachon, E., Martin, R., Kwok, V., Cherepanov, V., Chow, C.-W., Doerschuk, C.M., Plumb, J., Grinstein, S. & Downey, G.P. CD44-mediated phagocytosis induces inside-out activation of complement receptor-3 in murine macrophages. *Blood* **110**, 4492–4502 (2007).
114. Vachon, E., Martin, R., Plumb, J., Kwok, V., Vandivier, R.W., Glogauer, M., Kapus, A., Wang, X., Chow, C.-W., Grinstein, S. & Downey, G.P. CD44 is a phagocytic receptor. *Blood* **107**, 4149–4158 (2006).
115. Koopmans, T. & van Rooij, E. Maintaining the LYVE1 line through macrophage and lymphatic interplay in the regenerating neonatal heart. *Nature Cardiovascular Research* (2025).
116. Gale, N.W., Prevo, R., Espinosa, J., Ferguson, D.J., Dominguez, M.G., Yancopoulos, G.D., Thurston, G. & Jackson, D.G. Normal Lymphatic Development and Function in Mice Deficient for the Lymphatic Hyaluronan Receptor LYVE-1. *Molecular and Cellular Biology* **27**, 595–604 (2007).
117. Iqbal, A.J., McNeill, E., Kapellos, T.S., Regan-Komito, D., Norman, S., Burd, S., Smart, N., Machemer, D.E., Stylianou, E., McShane, H., Channon, K.M., Chawla, A. & Greaves, D.R. Human CD68 promoter GFP transgenic mice allow analysis of monocyte to macrophage differentiation in vivo. *Blood* **124**, e33–44 (2014).
118. Jung, S., Aliberti, J., Graemmel, P., Sunshine, M.J., Kreutzberg, G.W., Sher, A. & Littman, D.R. Analysis of fractalkine receptor CX(3)CR1 function by targeted deletion and green fluorescent protein reporter gene insertion. *Mol Cell Biol* **20**, 4106–4114 (2000).
119. Zaman, R. & Epelman, S. Resident cardiac macrophages: Heterogeneity and function in health and disease. *Immunity* **55**, 1549–1563 (2022).
120. Rumianek, A.N., Davies, B., Channon, K.M., Greaves, D.R. & Purvis, G.S.D. A Human CD68 Promoter-Driven Inducible Cre-Recombinase Mouse Line Allows Specific Targeting of Tissue Resident Macrophages. *Front Immunol* **13**, 918636 (2022).
121. De Villiers, C. & Riley, P.R. A Refined Protocol for Coronary Artery Ligation in the Neonatal Mouse. *Curr Protoc* **1**, e66 (2021).
122. Renier, N., Wu, Z., Simon, D.J., Yang, J., Ariel, P. & Tessier-Lavigne, M. iDISCO: a simple, rapid method to immunolabel large tissue samples for volume imaging. *Cell* **159**, 896–910 (2014).
123. Rueden, C.T., Schindelin, J., Hiner, M.C., DeZonia, B.E., Walter, A.E., Arena, E.T. & Eliceiri, K.W. ImageJ2: ImageJ for the next generation of scientific image data. *BMC Bioinformatics* **18**, 529 (2017).
124. Stuart, T., Butler, A., Hoffman, P., Hafemeister, C., Papalexi, E., Mauck, W.M., 3rd, Hao, Y., Stoeckius, M., Smibert, P. & Satija, R. Comprehensive Integration of Single-Cell Data. *Cell* **177**, 1888–1902 e1821 (2019).
125. Wang, Z., Cui, M., Shah, A.M., Tan, W., Liu, N., Bassel-Duby, R. & Olson, E.N. Cell-Type-Specific Gene Regulatory Networks Underlying Murine Neonatal Heart Regeneration at Single-Cell Resolution. *Cell reports* **33**, 108472 (2020).
126. Li, H. Minimap2: pairwise alignment for nucleotide sequences. *Bioinformatics* **34**, 3094–3100 (2018).
127. Heaton, H., Talman, A.M., Knights, A., Imaz, M., Gaffney, D.J., Durbin, R., Hemberg, M. & Lawniczak, M.K.N. Souporcell: robust clustering of single-cell RNA-seq data by genotype without reference genotypes. *Nat Methods* **17**, 615–620 (2020).
128. Huang, Y., McCarthy, D.J. & Stegle, O. Vireo: Bayesian demultiplexing of pooled single-cell RNA-seq data without genotype reference. *Genome Biol* **20**, 273 (2019).

129. Dann, E., Henderson, N.C., Teichmann, S.A., Morgan, M.D. & Marioni, J.C. Differential abundance testing on single-cell data using k-nearest neighbor graphs. *Nat Biotechnol* **40**, 245–253 (2022).
130. Tirosh, I., Venteicher, A.S., Hebert, C., Escalante, L.E., Patel, A.P., Yizhak, K., Fisher, J.M., Rodman, C., Mount, C., Filbin, M.G., Neftel, C., Desai, N., Nyman, J., Izar, B., Luo, C.C., Francis, J.M., Patel, A.A., Onozato, M.L., Riggi, N., Livak, K.J., Gennert, D., Satija, R., Nahed, B.V., Curry, W.T., Martuza, R.L., Mylvaganam, R., Iafrate, A.J., Frosch, M.P., Golub, T.R., Rivera, M.N., Getz, G., Rozenblatt-Rosen, O., Cahill, D.P., Monje, M., Bernstein, B.E., Louis, D.N., Regev, A. & Suvà, M.L. Single-cell RNA-seq supports a developmental hierarchy in human oligodendroglioma. *Nature* **539**, 309–313 (2016).
131. Susaki, E.A., Tainaka, K., Perrin, D., Kishino, F., Tawara, T., Watanabe, T.M., Yokoyama, C., Onoe, H., Eguchi, M., Yamaguchi, S., Abe, T., Kiyonari, H., Shimizu, Y., Miyawaki, A., Yokota, H. & Ueda, H.R. Whole-brain imaging with single-cell resolution using chemical cocktails and computational analysis. *Cell* **157**, 726–739 (2014).
132. Tvorogov, D., Anisimov, A., Zheng, W., Leppänen, V.M., Tammela, T., Laurinavicius, S., Holnthoner, W., Heloterä, H., Holopainen, T., Jeltsch, M., Kalkkinen, N., Lankinen, H., Ojala, P.M. & Alitalo, K. Effective suppression of vascular network formation by combination of antibodies blocking VEGFR ligand binding and receptor dimerization. *Cancer Cell* **18**, 630–640 (2010).
133. Heinolainen, K., Karaman, S., D'Amico, G., Tammela, T., Sormunen, R., Eklund, L., Alitalo, K. & Zarkada, G. VEGFR3 Modulates Vascular Permeability by Controlling VEGF/VEGFR2 Signaling. *Circ Res* **120**, 1414–1425 (2017).
134. Zhang, Y., Ulvmar, M.H., Stanczuk, L., Martinez-Corral, I., Frye, M., Alitalo, K. & Mäkinen, T. Heterogeneity in VEGFR3 levels drives lymphatic vessel hyperplasia through cell-autonomous and non-cell-autonomous mechanisms. *Nat Commun* **9**, 1296 (2018).
135. Dumont, D.J., Jussila, L., Taipale, J., Lymboussaki, A., Mustonen, T., Pajusola, K., Breitman, M. & Alitalo, K. Cardiovascular failure in mouse embryos deficient in VEGF receptor-3. *Science* **282**, 946–949 (1998).
136. Farbehi, N., Patrick, R., Dorison, A., Xaymardan, M., Janbandhu, V., Wystub-Lis, K., Ho, J.W., Nordon, R.E. & Harvey, R.P. Single-cell expression profiling reveals dynamic flux of cardiac stromal, vascular and immune cells in health and injury. *eLife* **8**(2019).
137. Liu, X., De la Cruz, E., Gu, X., Balint, L., Oxendine-Burns, M., Terrones, T., Ma, W., Kuo, H.-H., Lantz, C., Bansal, T., Thorp, E., Burridge, P., Jakus, Z., Herz, J., Cleaver, O., Torres, M. & Oliver, G. Lymphoangiocrine signals promote cardiac growth and repair. *Nature* **588**, 705–711 (2020).
138. Gancz, D., Perlmoter, G. & Yaniv, K. Formation and Growth of Cardiac Lymphatics during Embryonic Development, Heart Regeneration, and Disease. *Cold Spring Harb Perspect Biol* **12**(2020).
139. Lioux, G., Liu, X., Temino, S., Oxendine, M., Ayala, E., Ortega, S., Kelly, R.G., Oliver, G. & Torres, M. A Second Heart Field-Derived Vasculogenic Niche Contributes to Cardiac Lymphatics. *Dev Cell* **52**, 350–363 e356 (2020).
140. Keller, T.C.S.I.V., Lim, L., Shewale, S.V., McDaid, K., Martí-Pàmies, Í., Tang, A.T., Wittig, C., Guerrero, A.A., Sterling, S., Leu, N.A., Scherrer-Crosbie, M., Gimotty, P.A. & Kahn, M.L. Genetic blockade of lymphangiogenesis does not impair cardiac function after myocardial infarction. *The Journal of Clinical Investigation* **131**(2021).
141. Gonzalez-Rosa, J.M., Martin, V., Peralta, M., Torres, M. & Mercader, N. Extensive scar formation and regression during heart regeneration after cryoinjury in zebrafish. *Development* **138**, 1663–1674 (2011).
142. Porrello, E.R., Mahmoud, A.I., Simpson, E., Hill, J.A., Richardson, J.A., Olson, E.N. & Sadek, H.A. Transient regenerative potential of the neonatal mouse heart. *Science* **331**, 1078–1080 (2011).

143. Harrison, M.R., Feng, X., Mo, G., Aguayo, A., Villafuerte, J., Yoshida, T., Pearson, C.A., Schulte-Merker, S. & Lien, C.L. Late developing cardiac lymphatic vasculature supports adult zebrafish heart function and regeneration. *Elife* **8**(2019).
144. Vivien, C.J., Pichol-Thievend, C., Sim, C.B., Smith, J.B., Bower, N.I., Hogan, B.M., Hudson, J.E., Francois, M. & Porrello, E.R. Vegfc/d-dependent regulation of the lymphatic vasculature during cardiac regeneration is influenced by injury context. *NPJ Regen Med* **4**, 18 (2019).
145. Hilgendorf, I., Gerhardt, L.M., Tan, T.C., Winter, C., Holderried, T.A., Chousterman, B.G., Iwamoto, Y., Liao, R., Zirlik, A., Scherer-Crosbie, M., Hedrick, C.C., Libby, P., Nahrendorf, M., Weissleder, R. & Swirski, F.K. Ly-6Chigh monocytes depend on Nr4a1 to balance both inflammatory and reparative phases in the infarcted myocardium. *Circ Res* **114**, 1611–1622 (2014).
146. Schmid-Schonbein, G.W. The second valve system in lymphatics. *Lymphat Res Biol* **1**, 25–29; discussion 29–31 (2003).
147. Travisano, S.I., Harrison, M.R.M., Thornton, M.E., Grubbs, B.H., Quertermous, T. & Lien, C.L. Single-nuclei multiomic analyses identify human cardiac lymphatic endothelial cells associated with coronary arteries in the epicardium. *Cell reports* **42**, 113106 (2023).
148. Cahill, T.J., Sun, X., Ravaud, C., Villa Del Campo, C., Klaourakis, K., Lupu, I.E., Lord, A.M., Browne, C., Jacobsen, S.E.W., Greaves, D.R., Jackson, D.G., Cowley, S.A., James, W., Choudhury, R.P., Vieira, J.M. & Riley, P.R. Tissue-resident macrophages regulate lymphatic vessel growth and patterning in the developing heart. *Development* **148**(2021).
149. Madisen, L., Zwingman, T.A., Sunkin, S.M., Oh, S.W., Zariwala, H.A., Gu, H., Ng, L.L., Palmiter, R.D., Hawrylycz, M.J., Jones, A.R., Lein, E.S. & Zeng, H. A robust and high-throughput Cre reporting and characterization system for the whole mouse brain. *Nat Neurosci* **13**, 133–140 (2010).
150. Emde, B., Heinen, A., Gödecke, A. & Bottermann, K. Wheat germ agglutinin staining as a suitable method for detection and quantification of fibrosis in cardiac tissue after myocardial infarction. *Eur J Histochem* **58**, 2448 (2014).
151. Cho, C.H., Koh, Y.J., Han, J., Sung, H.K., Jong Lee, H., Morisada, T., Schwendener, R.A., Brekken, R.A., Kang, G., Oike, Y., Choi, T.S., Suda, T., Yoo, O.J. & Koh, G.Y. Angiogenic role of LYVE-1-positive macrophages in adipose tissue. *Circ Res* **100**, e47–57 (2007).
152. Kieu, T.Q., Tazawa, K., Kawashima, N., Noda, S., Fujii, M., Nara, K., Hashimoto, K., Han, P. & Okiji, T. Kinetics of LYVE-1-positive M2-like macrophages in developing and repairing dental pulp in vivo and their pro-angiogenic activity in vitro. *Scientific Reports* **12**, 5176 (2022).
153. Platonova, N., Miquel, G., Regenfuss, B., Taouji, S., Cursiefen, C., Chevet, E. & Bikfalvi, A. Evidence for the interaction of fibroblast growth factor-2 with the lymphatic endothelial cell marker LYVE-1. *Blood* **121**, 1229–1237 (2013).
154. Lim, H.Y., Lim, S.Y., Tan, C.K., Thiam, C.H., Goh, C.C., Carbajo, D., Chew, S.H.S., See, P., Chakarov, S., Wang, X.N., Lim, L.H., Johnson, L.A., Lum, J., Fong, C.Y., Bongso, A., Biswas, A., Goh, C., Evrard, M., Yeo, K.P., Basu, R., Wang, J.K., Tan, Y., Jain, R., Tikoo, S., Choong, C., Weninger, W., Poidinger, M., Stanley, R.E., Collin, M., Tan, N.S., Ng, L.G., Jackson, D.G., Ginhoux, F. & Angeli, V. Hyaluronan Receptor LYVE-1-Expressing Macrophages Maintain Arterial Tone through Hyaluronan-Mediated Regulation of Smooth Muscle Cell Collagen. *Immunity* **49**, 326–341.e327 (2018).
155. Yu, X., Hu, Y., Lim, H.Y., Li, Z., Jaitin, D.A., Yang, K., Kong, W.T., Xu, J., Bejarano, D.A., Bied, M., Orliaguet, L., Rengasamy, G., Chow, Z., Lee, C.Z.W., Lum, J., Tian, J., Zhang, X.-M., Liu, H., Tan, S.W., Chen, J., See, P., Loh, Y.-H., Malleret, B., Baig, S., Yassin, M.S.M., Toh, S.-A.E.S., Malissen, B., Fu, X., Kabashima, K., Ng, L.G., Blériot, C., Liu, Z., Sheng, L., Zheng, D.-N., Qu, J., Venteclef, N., Su, B., Amit, I., Schlitzer, A.,

Angeli, V., Ginhoux, F. & Chakarov, S. Septal LYVE1+ macrophages control adipocyte stem cell adipogenic potential. *Science* **389**, eadg1128 (2025).
156. Elfstrum, A.K., Rumahorbo, A.H., Reese, L.E., Nelson, E.V., McCluskey, B.M. & Schwertfeger, K.L. LYVE-1–expressing Macrophages Modulate the Hyaluronan-containing Extracellular Matrix in the Mammary Stroma and Contribute to Mammary Tumor Growth. *Cancer Research Communications* **4**, 1380–1397 (2024).
157. Hart, S.P., Rossi, A.G., Haslett, C. & Dransfield, I. Characterization of the effects of cross-linking of macrophage CD44 associated with increased phagocytosis of apoptotic PMN. *PLoS One* **7**, e33142 (2012).
158. Le, T., Ferling, I., Qiu, L., Nabaile, C., Assunção, L., Roskelley, C.D., Grinstein, S. & Freeman, S.A. Redistribution of the glycocalyx exposes phagocytic determinants on apoptotic cells. *Dev Cell* **59**, 853–868.e857 (2024).
159. Dollt, C., Becker, K., Michel, J., Melchers, S., Weis, C.-A., Schledzewski, K., Krewer, A., Kloss, L., Gebhardt, C., Utikal, J. & Schmieder, A. The shedded ectodomain of Lyve-1 expressed on M2-like tumor-associated macrophages inhibits melanoma cell proliferation. *Oncotarget* **8**(2017).
160. Johnson, P., Arif, A.A., Lee-Sayer, S.S.M. & Dong, Y. Hyaluronan and Its Interactions With Immune Cells in the Healthy and Inflamed Lung. *Frontiers in Immunology* **Volume 9 - 2018**(2018).
161. Lavin, Y., Winter, D., Blecher-Gonen, R., David, E., Keren-Shaul, H., Merad, M., Jung, S. & Amit, I. Tissue-resident macrophage enhancer landscapes are shaped by the local microenvironment. *Cell* **159**, 1312–1326 (2014).
162. Hampton, H.R., Bailey, J., Tomura, M., Brink, R. & Chtanova, T. Microbe-dependent lymphatic migration of neutrophils modulates lymphocyte proliferation in lymph nodes. *Nature Communications* **6**, 7139 (2015).
163. Jakovija, A. & Chtanova, T. Neutrophil Interactions with the Lymphatic System. *Cells* **10**(2021).
164. Pulikkot, S., Hu, L., Chen, Y., Sun, H. & Fan, Z. Integrin Regulators in Neutrophils. *Cells* **11**, 2025 (2022).
165. Horckmans, M., Ring, L., Duchene, J., Santovito, D., Schloss, M.J., Drechsler, M., Weber, C., Soehnlein, O. & Steffens, S. Neutrophils orchestrate post-myocardial infarction healing by polarizing macrophages towards a reparative phenotype. *Eur Heart J* **38**, 187–197 (2017).
166. Hempel, C., Wang, C.W., Kurtzhals, J.A.L. & Staalsø, T. Binding of Plasmodium falciparum to CD36 can be shielded by the glycocalyx. *Malaria Journal* **16**, 193 (2017).
167. Introini, V., Carciati, A., Tomaiuolo, G., Cicuta, P. & Guido, S. Endothelial glycocalyx regulates cytoadherence in Plasmodium falciparum malaria. *Journal of The Royal Society Interface* **15**, 20180773 (2018).
168. Uribe-Querol, E. & Rosales, C. Phagocytosis: Our Current Understanding of a Universal Biological Process. *Frontiers in Immunology* **11**(2020).
169. Silva, M.T. Macrophage phagocytosis of neutrophils at inflammatory/infectious foci: a cooperative mechanism in the control of infection and infectious inflammation. *Journal of Leukocyte Biology* **89**, 675–683 (2011).
170. Lee, P.Y., Wang, J.X., Parisini, E., Dascher, C.C. & Nigrovic, P.A. Ly6 family proteins in neutrophil biology. *J Leukoc Biol* **94**, 585–594 (2013).
171. Amorim, A., De Feo, D., Friebel, E., Ingelfinger, F., Anderfuhren, C.D., Krishnarajah, S., Andreadou, M., Welsh, C.A., Liu, Z., Ginhoux, F., Greter, M. & Becher, B. IFNγ and GM-CSF control complementary differentiation programs in the monocyte-to-phagocyte transition during neuroinflammation. *Nat Immunol* **23**, 217–228 (2022).
172. McKee, C.M., Penno, M.B., Cowman, M., Burdick, M.D., Strieter, R.M., Bao, C. & Noble, P.W. Hyaluronan (HA) fragments induce chemokine gene expression in alveolar macrophages. The role of HA size and CD44. *J Clin Invest* **98**, 2403–2413 (1996).
173. Banerji, S., Lawrance, W., Metcalfe, C., Briggs, D.C., Yamauchi, A., Dushek, O., van der Merwe, P.A., Day, A.J. & Jackson, D.G. Homodimerization of the Lymph Vessel

Endothelial Receptor LYVE-1 through a Redox-labile Disulfide Is Critical for Hyaluronan Binding in Lymphatic Endothelium. *J Biol Chem* **291**, 25004–25018 (2016).
174. Eitel, I. & Friedrich, M.G. T2-weighted cardiovascular magnetic resonance in acute cardiac disease. *Journal of Cardiovascular Magnetic Resonance* **13**, 13 (2011).
175. Buchrieser, J., James, W. & Moore, M.D. Human Induced Pluripotent Stem Cell-Derived Macrophages Share Ontogeny with MYB-Independent Tissue-Resident Macrophages. *Stem Cell Reports* **8**, 334–345 (2017).
176. Schledzewski, K., Falkowski, M., Moldenhauer, G., Metharom, P., Kzhyshkowska, J., Ganss, R., Demory, A., Falkowska-Hansen, B., Kurzen, H., Ugurel, S., Geginat, G., Arnold, B. & Goerdt, S. Lymphatic endothelium-specific hyaluronan receptor LYVE-1 is expressed by stabilin-1+, F4/80+, CD11b+ macrophages in malignant tumours and wound healing tissue in vivo and in bone marrow cultures in vitro: implications for the assessment of lymphangiogenesis. *The Journal of Pathology* **209**, 67–77 (2006).
177. Ma, Y. Role of Neutrophils in Cardiac Injury and Repair Following Myocardial Infarction. *Cells* **10**(2021).
178. Ichimura, S., Misaka, T., Ogawara, R., Tomita, Y., Anzai, F., Sato, Y., Miura, S., Yokokawa, T., Sato, T., Oikawa, M., Kobayashi, A., Yoshihisa, A. & Takeishi, Y. Neutrophil Extracellular Traps in Myocardial Tissue Drive Cardiac Dysfunction and Adverse Outcomes in Patients With Heart Failure With Dilated Cardiomyopathy. *Circulation: Heart Failure* **17**, e011057 (2024).
179. Liu, J., Yang, C., Liu, T., Deng, Z., Fang, W., Zhang, X., Li, J., Huang, Q., Liu, C., Wang, Y., Yang, D., Sukhova, G.K., Lindholt, J.S., Diederichsen, A., Rasmussen, L.M., Li, D., Newton, G., Luscinskas, F.W., Liu, L., Libby, P., Wang, J., Guo, J. & Shi, G.-P. Eosinophils improve cardiac function after myocardial infarction. *Nature Communications* **11**, 6396 (2020).
180. Toor, I.S., Rückerl, D., Mair, I., Ainsworth, R., Meloni, M., Spiroski, A.M., Benezech, C., Felton, J.M., Thomson, A., Caporali, A., Keeble, T., Tang, K.H., Rossi, A.G., Newby, D.E., Allen, J.E. & Gray, G.A. Eosinophil Deficiency Promotes Aberrant Repair and Adverse Remodeling Following Acute Myocardial Infarction. *JACC Basic Transl Sci* **5**, 665–681 (2020).
181. Sicklinger, F., Meyer, I.S., Li, X., Radtke, D., Dicks, S., Kornadt, M.P., Mertens, C., Meier, J.K., Lavine, K.J., Zhang, Y., Kuhn, T.C., Terzer, T., Patel, J., Boerries, M., Schramm, G., Frey, N., Katus, H.A., Voehringer, D. & Leuschner, F. Basophils balance healing after myocardial infarction via IL-4/IL-13. *J Clin Invest* **131**(2021).
182. Wong, N.R., Mohan, J., Kopecky, B.J., Guo, S., Du, L., Leid, J., Feng, G., Lokshina, I., Dmytrenko, O., Luehmann, H., Bajpai, G., Ewald, L., Bell, L., Patel, N., Bredemeyer, A., Weinheimer, C.J., Nigro, J.M., Kovacs, A., Morimoto, S., Bayguinov, P.O., Fisher, M.R., Stump, W.T., Greenberg, M., Fitzpatrick, J.A.J., Epelman, S., Kreisel, D., Sah, R., Liu, Y., Hu, H. & Lavine, K.J. Resident cardiac macrophages mediate adaptive myocardial remodeling. *Immunity* **54**, 2072–2088.e2077 (2021).
183. Holt, M., Lin, J., Cicka, M., Wong, A., Epelman, S. & Lavine, K.J. Dissecting and Visualizing the Functional Diversity of Cardiac Macrophages. *Circulation Research* **134**, 1791–1807 (2024).
184. Cahill, T.J., Choudhury, R.P. & Riley, P.R. Heart regeneration and repair after myocardial infarction: translational opportunities for novel therapeutics. *Nature Reviews Drug Discovery* **16**, 699–717 (2017).
185. Majmudar, M.D., Keliher, E.J., Heidt, T., Leuschner, F., Truelove, J., Sena, B.F., Gorbatov, R., Iwamoto, Y., Dutta, P., Wojtkiewicz, G., Courties, G., Sebas, M., Borodovsky, A., Fitzgerald, K., Nolte, M.W., Dickneite, G., Chen, J.W., Anderson, D.G., Swirski, F.K., Weissleder, R. & Nahrendorf, M. Monocyte-directed RNAi targeting CCR2 improves infarct healing in atherosclerosis-prone mice. *Circulation* **127**, 2038–2046 (2013).
186. Leuschner, F., Dutta, P., Gorbatov, R., Novobrantseva, T.I., Donahoe, J.S., Courties, G., Lee, K.M., Kim, J.I., Markmann, J.F., Marinelli, B., Panizzi, P., Lee, W.W., Iwamoto,

Y., Milstein, S., Epstein-Barash, H., Cantley, W., Wong, J., Cortez-Retamozo, V., Newton, A., Love, K., Libby, P., Pittet, M.J., Swirski, F.K., Koteliansky, V., Langer, R., Weissleder, R., Anderson, D.G. & Nahrendorf, M. Therapeutic siRNA silencing in inflammatory monocytes in mice. *Nat Biotechnol* **29**, 1005–1010 (2011).

187. Zhang, S., Yeap, X.Y., DeBerge, M., Naresh, N.K., Wang, K., Jiang, Z., Wilcox, J.E., White, S.M., Morrow, J.P., Burridge, P.W., Procissi, D., Scott, E.A., Frazier, W. & Thorp, E.B. Acute CD47 Blockade During Ischemic Myocardial Reperfusion Enhances Phagocytosis-Associated Cardiac Repair. *JACC Basic Transl Sci* **2**, 386–397 (2017).
188. Vagnozzi, R.J., Maillet, M., Sargent, M.A., Khalil, H., Johansen, A.K.Z., Schwanekamp, J.A., York, A.J., Huang, V., Nahrendorf, M., Sadayappan, S. & Molkentin, J.D. An acute immune response underlies the benefit of cardiac stem cell therapy. *Nature* **577**, 405–409 (2020).
189. Lancaster, J.J., Grijalva, A., Fink, J., Ref, J., Daugherty, S., Whitman, S., Fox, K., Gorman, G., Lancaster, L.D., Avery, R., Acharya, T., McArthur, A., Strom, J., Pierce, M.K., Moukabary, T., Borgstrom, M., Benson, D., Mangiola, M., Pandey, A.C., Zile, M.R., Bradshaw, A., Koevary, J.W. & Goldman, S. Biologically derived epicardial patch induces macrophage mediated pathophysiologic repair in chronically infarcted swine hearts. *Communications Biology* **6**, 1203 (2023).